UNIVERSITY OF
THESSALY

SCHOOL OF ENGINEERING

DEPARTMENT OF MECHANICAL ENGINEERING

Diploma Thesis

Rise of a liquid metal under the combined effect of Capillary and Lorentz forces

by

Konstantinos Bouchoris

SUBMITTED IN PARTIAL FULFILLMENT OF THE REQUIREMENTS
FOR DIPLOMA IN MECHANICAL ENGINEERING
OCTOBER 2019

Certified by the members of the Examination Committee

1st member Supervisor	Dr. Nikolaos Pelekasis Professor, Department of Mechanical Engineering University of Thessaly
2nd member	Dr. Dimitrios Valougeorgis Professor, Department of Mechanical Engineering University of Thessaly
3rd member	Dr. Vasilios Bontozoglou Professor, Department of Mechanical Engineering University of Thessaly

Acknowledgements

First and foremost, I would like to thank the supervisor of my diploma thesis Professor Nikolaos Pelekasis for entrusting me with this particular topic giving me the chance to study and learn the basics of a very fascinating discipline of Fluid Dynamics, namely Magnetohydrodynamics. His encouragement and deep scientific expertise concerning mathematical Fluid Mechanics and Computational implementation were indispensable and without his guidance the completion of this work would not be possible. Moreover, I feel deeply indebted to Dr. Maria Vlachomitrou, who introduced me to Computational Fluid Dynamics and especially the Finite Element Method. Her invaluable knowledge concerning CFD and coding made it possible for me to complete this project and without her immense support its completion would have been extremely difficult. It was a pleasure learning from such a wonderful and gentle personality. Also, I need to express my gratitude to Dr Lefteris Benos for various fruitful discussions about theoretical and technological aspects of the CPS he numerically investigated in his PhD Thesis. A large part of this work was based on his research. Many thanks to Professors Dimitrios Valougeorgis and Vasilios Bontozoglou for accepting to be members of the examination committee and equiping me with their knowldge on Numerical Methods and Transport Phenomena. Undoubtley, I wholeheartedly thank Dr. Anna Zervaki especially for her moral support, during the final year of my studies. Nevertheless, I express my sincere gratitude to all of my friends and especially Rafail, Nikos, Bill and Chris for the endless moments of joy, fruitful, serious and funny discussions during all of the years of my undergraduate studies. Lastly, this work is dedicated to the memory of the person who encouraged me the most throughout my life but is not with us anymore, my beloved mother. I will never be thankful enough to her.

Life is like riding a bicycle, to keep your balance you must keep moving.

Albert Einstein

Abstract

This work is concerned with the study of the capillary rise of a liquid metal (LM) within a Capillary Porous System (CPS) under the effect of an external magnetic field. The duty of the CPS is to protect the divertor, a device of critical importance for the operation of a Fusion Reactor. Liquid Li is considered for the numerical simulations due to its deployment in many experiments conducted worldwide. Firstly, a mathematical model describing the capillary rise of a liquid metal (LM) under the influence of a transverse magnetic field within a CPS is presented. Gravitational, viscous, inertial, surface tension and magnetic forces are accounted for, while the problem geometry consists of a single vertical capillary tube, similar to previous studies. Electrical currents entering the CPS via the liquid metal interface are also present. The mathematical model is based on liquid metal MHD of low R_m number. The Galerkin Finite Element Method is used in order to solve the mathematical problem presented here. Mesh generation is carried out via the spine method. Results of velocity and magnetic induction distribution along the interface strongly depend on the intensity and the direction of the electrical currents entering the CPS via the interface. Pressure distribution along the CPS height direction follows a linear distribution and pressure drop increases with the intensity of the electrical currents at the interface for constant external magnetic field. Time required for the liquid to exit the CPS is found to decrease with the magnetic Bond number, while the exit velocity increases almost linearly with the latter. For the case of 1T magnetic field and external currents producing magnetic pressure greater than the characteristic pressure, interfacial distortions were observed during the initial stages of the LM motion, indicating the possibility of drop ejection. Lastly, simulations with varying pore radius and constant current, field intensity were also performed. Distortions of the interface were found to be enhanced with increasing radius.

Keywords: Capillary Porous System, Liquid metal, MHD, Finite Element Method, spine method, magnetic Bond number, Fusion

Περίληψη

Η παρούσα μελέτη ασχολείται με την μαθηματική περιγραφή της τριχωειδούς ανύψωσης ενός υγρού μετάλλου μέσα σε διάταξη CPS υπό την επίδραση ενός εγκάρσιου μαγνητικού πεδίου. Το καθήκον αυτής της διάταξης είναι να προστατεύει τον divertor, ένα εξάρτημα νευραλγικής σημασίας για την λειτουργία ενος μελλοντικού αντιδραστήρα θερμοπυρηνικής σύντηξης. Ως υγρό θεωρήθηκε το Λίθιο εξαιτίας της χρήσης του σε διάφορα πειράματα που έχουν διεξαχθεί παγκοσμίως. Αρχικά περιγράφεται το μαθηματικό μοντέλο. Η γεωμετρία του προβλήματος αποτελείται από έναν κατακόρυφο τριχωειδή σωλήνα, όπως έχει γίνει σε προηγούμενες μελέτες, παρουσία βαρυτικών, ιξωδών, αδρανειακών, τριχωειδών και μαγνητικών δυνάμεων. Επιπλέον, ηλεκτρικά ρεύματα εισέρχονται στο CPS μέσω της διεπειφάνειας του υγρού μετάλλου. Το μαθηματικό μοντέλο βασίζεται στην Μαγνητοϋδροδυναμική υγρών μετάλλων χαμηλού μαγνητικού αριθμού Reynolds. Προκειμένου να επιλυθεί αριθμητικά το μαθηματικό πρόβλημα, χρησιμοποιήθηκε η Μέθοδος των Πεπερασμένων Στοιχείων κατά Galerkin. Η δημιουργία του πλέγματος έγινε με τη μέθοδο Spine. Τα αποτελέσματα που εξήχθησαν δείχνουν ότι οι κατανομές της αξονικής ταχύτητας και της μαγνητικής επαγωγής κατά μήκος της διεπιφάνειας εξαρτώνται σε μεγάλο βαθμό από το μέγεθος και την κατεύθυνση του ρεύματος που προσπίπτει στη διεπιφάνεια. Η κατανομή της πίεσης κατά μήκος του ύψους του πόρου είναι γραμμική και η πτώση πίεσης αυξάνεται καθώς αυξάνεται και η ένταση της ρευματικής πυκνότητας στη διεπιφάνεια για σταθερή ένταση του μαγνητικού πεδίου. Ο απαιτούμενος χρόνος για να εξέλθει το υγρό μέταλλο από τον πόρο μειώνεται με την αύξηση του μαγνητικού αριθμού Bond ενώ η ταχύτητα στην έξοδο μεταβάλλεται γραμμικά με τον τελευταίο. Στην περίπτωση μαγνητικού πεδίου 1T και για τιμές του ρεύματος στην διεπιφάνεια για τις οποίες η μαγνητική πίεση είναι μεγαλύτερη της χαρακτηριστικής παρατηρήθηκαν παραμορφώσεις στο σχήμα της διεπιφάνειας κατά τα αρχικά χρονικά στάδια των προσομοιώσεων. Η διαπίστωση αυτή υποδεικνύει την πιθανότητα αποκόλλησης σταγόνων (drop ejection) από το υγρό μέταλλο. Τέλος, έγιναν προσομοιώσεις για μεταβλητό μέγεθος πόρου όπου διαπιστώθηκε ότι οι παραπάνω παραμορφώσεις στη διεπιφάνεια γίνονται πιο έντονες καθώς αυξάνεται η ακτίνα του πόρου.

Λέξεις Κλειδία: Capillary Porous System, Υγρό μέταλλο, Μαγνητοϋδροδυναμική, Πεπερασμένα Στοιχεία, Μέθοδος Spine, Μαγνητικός αριθμός Bond, Σύντηξη

Table of Contents

Nomenclature

Latin Letters

u	Axial velocity component
v	Radial velocity component
p	Pressure
H	Magnetic Induction
B_0	Imposed magnetic field intensity
J	Current density at the pore entrance
f	Free surface shape
R_p	Pore radius
g	Gravitational acceleration
J_r	r component of current density at the interface
J_z	z component of current density at the interface
r, z	Spatial Coordinates
t	time
h_0	Pore height
l	slip length

Greek Letters

γ	Surface tension
σ	Electric conductivity
μ	Dynamic viscosity
ρ	Mass density
μ_m	Magnetic Permeability
θ_c	Contact angle

Dimensionless Numbers

Ca	Capillary number
We	Weber number
Bo	Gravitational Bond number
Bo_m	Magnetic Bond number
Re_m	Magnetic Reynolds number
c	Induction source
Re	Reynolds number

List of Figures

Chapter 1

Chapter 2

Chapter 3

Chapter 4

Chapter 5

Chapter 6

Chapter 7

List of Tables

Chapter 1: Introduction

In the first chapter, a literature review concerning controlled Thermonuclear Fusion mainly inside Tokamak devices is presented with an emphasis on the deployment of liquid metal surfaces as plasma facing components. Finally, an introduction to the main features and the worldwide studies of the Capillary Porous System is represented since it is considered the most promising choice concerning liquid surface plasma facing components.

1.1 Motivation for Fusion

It is a well-established fact that the world economy has heavily depended on fossil fuel usage for the last two centuries. As a result, Humanity has managed to improve its standard of living to an unprecedented degree. However, these resources are diminishing and without any action, an energy crisis is about to break out. Apart from the economic impact of fossil fuel shortages, there is also an environmental impact. Global warming due to carbon dioxide emissions and the accompanying climate change has become increasingly more alarming especially during the last decades. Nonetheless, energy consumption worldwide is expected to increase rather than decrease and mankind will not give up the present standard of living. Consequently, different energy sources are needed. Those that are available at present are of very low energy density (solar, wind and bio-energy) or produce long term radioactive waste (nuclear fission). Fortunately, there exists a particular source that lacks the above issues and promises virtually abundant energy supply, Thermonuclear Fusion.

Nuclear Fusion is the nuclear reaction in which two or more nuclei merge and a new element with greater atomic number (higher number of protons in the nucleus) is formed. In this reaction, an immense amount of energy is released and is related to Einstein's famous energy-mass equation $E = mc^2$. From a technical point of view, the most feasible fusion reaction on earth is the Deuterium – Tritium reaction. It is noteworthy that DT reaction has the highest energy gain in the lowest temperatures for thermonuclear fusion.

$$D + T \rightarrow He + n + 17.6\ MeV \tag{1.1}$$

In the reaction above, both reactants are Hydrogen isotopes and the result is a Helium nucleus, a neutron and energy release. Deuterium is available in the Earth's oceans while Tritium can be produced from a nuclear fission reaction of Lithium – largely available on earth – and an energetic neutron. The 'waste' of this reaction is Helium, which is non-toxic and non-radioactive.

According to the above, the advantages of nuclear fusion prove their superiority over other energy sources currently used. However, in order to make fusion commercially available on earth, a number of serious matters should be taken into account. First of all, the reacting nuclei are both positively charged and cannot fuse spontaneously due to the repelling Coulomb force. Therefore, a gas of charged particles must have a sufficiently large kinetic energy to overcome the Coulomb repulsion. This can be achieved in a temperature of about 10^8 degrees centigrade. At this state, the gas is ion-

ized and is in plasma state. Furthermore, the particle density (number of particles per unit volume) of the plasma should be high enough in order to have as many collisions as needed between the aforementioned nuclei.

From an engineering point of view, in order to harness fusion energy, researchers across the globe concerned with fusion research have to control the temperature, density and lifespan of the plasma fuel (D-T). Currently there are two different approaches on which fusion research is based. The first of these approaches is Magnetic Confinement Fusion (MCF), carried out in devices such as the magnetic mirror, the z-pinch and the Tokamak **Fig**. **1.1-1.3**. In these facilities, the plasma is characterized by low particle density but the plasma lifespan is sufficient enough to achieve the amount of collisions needed for energy release. On the contrary, in the second approach the plasma produced is of very high density and short lived. This approach is known as Inertial Confinement Fusion in which a small solid DT capsule is rapidly compressed and heated by laser beams releasing immense amounts of energy.

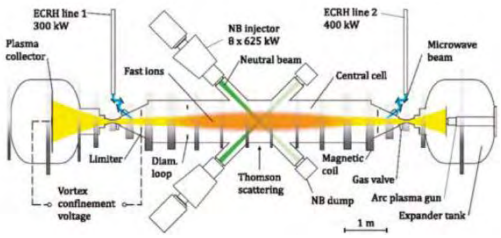

Fig. 1.1 Magnetic mirror configuration [34].

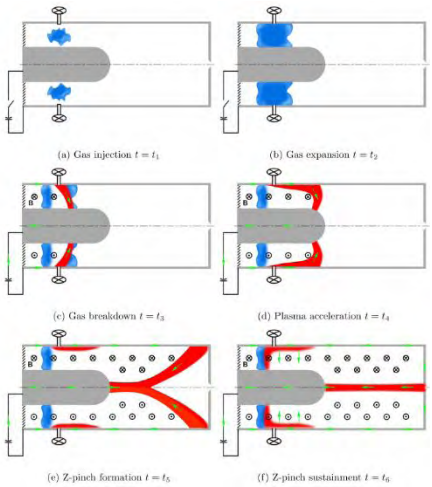

Fig. 1.2 Schematic illustration of the formation of a flow Z-pinch in the ZaP experiment [35].

The most widely used method for fusion research is the MCF with the plasma confined inside a Tokamak chamber. In a Tokamak facility, the plasma is confined in a toroidal chamber by magnetic fields of high intensity. These magnetic fields are provided by external coils and the current in the bulk region of the flowing plasma. In **Fig**. **1.3** the JET Tokamak can be seen along with the toroidal geometry of the plasma chamber. Within a Tokamak plasma, energy is produced through thermonuclear fusion of atoms and is absorbed as heat in the walls of the vessel [37].

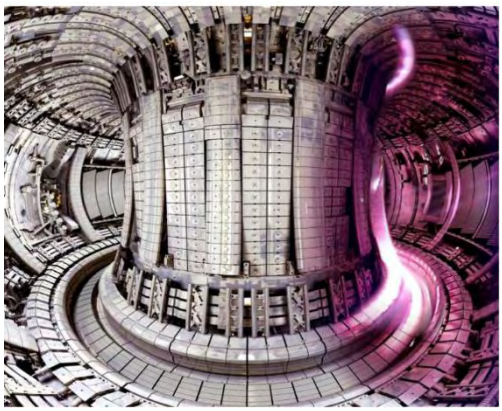

Fig. 1.3 An inside view of the Joint European Torus (JET) plasma chamber [36].

1.2 Liquid metals for Fusion research

Inside a Tokamak fusion reactor, the highest heat load is experienced by a structural element known as the divertor [17, 21]. While the neutron load in the divertor zone is lower than on the first blanket wall, its specific thermal loads are many times higher; their values incorporate flows of high-energy particles carried out of the plasma zone. Managing this considerable amount of heat is a vital issue in present and future reactors (e.g., DEMO) since power handling consists perhaps the greatest challenge in fusion research.

While Tungsten has long been identified as the most attractive material choice for a solid divertor, issues including surface cracking and deleterious modification of the surface must be faced to develop robust plasma facing components [47]. According to data from present experimental fusion reactors, e.g., JET (Joint European Torus), divertor walls made of tungsten can withstand specific heat loads of 20 MW/m^2 while studies concerning the design of a DEMO type divertor estimate its power handling capability to 5-10 MW/m^2 in steady-state conditions [47, 48]. Beyond this level a number of undesirable effects occur such as erosion, thermal stresses, thermal fatigue and plasma contamination. Such phenomena may irreversibly and negatively affect the proper operation of the reactor. Even in ITER conditions, where tungsten targets at the divertor will be deployed, issues of great significance arising from the presence of transient heat fluxes like ELMs (Edge Localized Modes) and plasma disruptions may make tungsten not the best choice for the divertor of any burning plasma experiments [22].

Consequently, the aforementioned issues have led researchers to consider liquid metals (LM for simplicity) as an alternative solution for Plasma Facing Components (PFM for short). The self-cooling and self-annealing properties of flowing liquids increase their life cycle as they interact with the scrape-off-layer of the fusion reactor [1]. Moreover, they can be recirculated and regenerated during their lifetime [47]. The currently available solutions with LMs, according to [21], are the following:

- Organization of liquid-metal films quickly flowing along a cooled substrate
- Creation of a “screen” by a liquid-metal flow
- Creation of drops for a liquid-metal screen
- Creation of a screen of dropping solid balls
- Placement of rotating cylinders in the divertor
- Capillary Porous System (CPS)

As far as advantages of LM usage are concerned, they are practically free from permanent damage by neutron and plasma irradiation and can be recirculated and regenerated for lifetime [22]. Furthermore, neutron effects in a Tokamak divertor are unavoidable but deployment of LM PFMs can circumvent this issue [46]. Specifically, they can out-perform any kind of solid PFM concept in areas such as erosion life-time and high heat load resistance [18]. Liquid metals deployed for R&D in fusion relevant environments and as PFCs include Tin (Sn), Gallium (Ga), Molten Li (Li) and Sn-Li [17, 46].

Generally speaking, the main role of a liquid metal PFC is to extract power from the magnetically confined plasma flowing inside the reactor chamber and transfer heat to a coolant that connects to the power conversion system. At the same time, it protects the divertor walls structural integrity and minimizes tritium retention. However, from the engineering point of view, all of the aforementioned concepts are difficult to implement them due to the fact that they have to be combined in a single device. In addition, although some of the issues that have to be addressed in a Tokamak environment are efficiently dealt with liquid metals, a main problem persists, instabilities of Magnetohydrodynamic nature due to electromagnetic forces. Analytically, in most LM PFCs the flow pattern is characterized by the formation of free surfaces or liquid metal drops [17, 38]. Therein large electrical currents are induced by violent plasma disruptions or thermionic emissions, which, then, interact with the tokamak magnetic field and produce body forces known as Lorentz forces that can destabilize the LM flow arrangement.

1.3 Deployment of a Capillary Porous System for protection of a plasma PFC

In the previous subsection, one of the main problems arising from LM deployment (Magnetohydrodynamic Instabilities) as PFMs, which arises regardless of the flow pattern, was stated. In order to appropriately face this issue, Russian researchers developed and currently prefer the Capillary Porous System (CPS) as liquid surface PFC. The CPS is based on the use of evaporation cooling for thermal load elimination and its operation is based on a fundamental property of liquid matter, surface tension. The main duty of a CPS is to constantly deliver liquid metal to a porous surface at sufficient working pressure without applying any external pressure since the flow within the porous structure is capillary driven instead of pressure driven [1, 17]. In other words, it acts as a capillary pump where the liquid motion is confined by capillary forces only and when there is shortage the same forces

automatically supply liquid [39]. Moreover, on top of the device rests a capillary-pore structure which reacts to local changes of the thermal load distribution on its surface [1].

Thus far, liquid metal devices based on condensation-evaporation seem highly promising. It is estimated that if the design of the target substrate is done properly, this energy removal method can provide excellent performance, which achieves ~ $O(10^2)$ Mw/m^2 [21]. Evaporation - Condensation devices which use Liquid Metals as the heat carrier fluid are proven to be the most efficient means of energy removal in high temperature facilities [17, 21]. Nygren and Tabarés [17], state that the CPS is the most mature path for liquid surface PFCs based on results coming especially from the Russian R&D program. In **Fig. 1.4** an illustration of a CPS deployed in two different experiments is depicted. Therein, the working fluid is pumped due to capillary forces from a large reservoir containing the liquid metal to a porous surface through a narrow wick. The porous structure contains a complex grid of capillary arteries [18] and is made from material with high thermal conductivity and good wetting properties with the working liquid. Their diameter varies from 10-100 μm [18]. It is useful to mention that these parameters have been observed to have an influence on the magnitude of capillary forces [17].

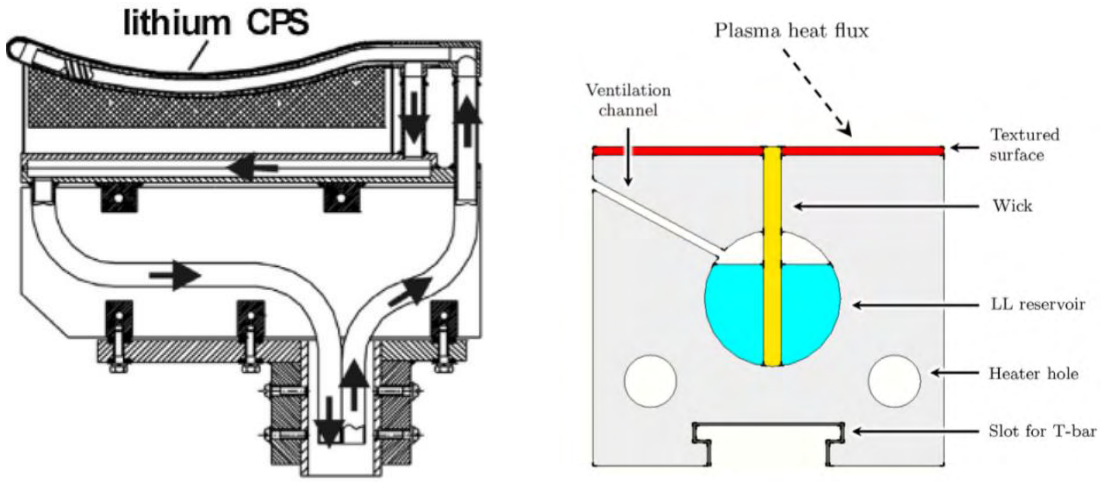

Fig. 1.4 An illustration of a CPS device with Li as the working fluid in a) Italian Tokamak in FTU facility [30] and b) NSTX-U [39].

In the review paper by Nygren and Tabarés (2016) summarized the main experimental results obtained during 1998-2009 [17]. Those are the following:

- Surface tension suppressed splashing of Li splashing, and regenerated the surface during a long experimental campaign.
- Erosion of liquid Li from the PFC is a strong function of Li temperature with a rate nearly the same as ion beam sputtering of liquid Li.

- Li non-coronal radiation cools the edge plasma, protects the PFC structure from high power loads in quasi-steady state and from disruptions.
- Hydrogen isotopes implanted in liquid Li by the plasma can be recovered at temperatures of 320–500 ºC with the range of Tritium being 400–500 ºC.

Apart from Li as the working fluid, a CPS target filled with liquid Sn has also been studied. It has been reported that the eroded vapour cloud removed some power from the plasma before it reached the target surface [46]. Moreover, in 2005-2006 CPS limiters with Li were deployed in FTU Tokamak device in Italy and in the Russian T-10 Tokamak. The CPS installation deployed there can be seen in **Fig. 1.6** a) and b). The original CPS successfully managed to deliver Li to host porous mesh at the plasma-wetted surface, **Fig. 1.6** c), even to the point of depleting the Li in the reservoir at the bottom of the device [30].

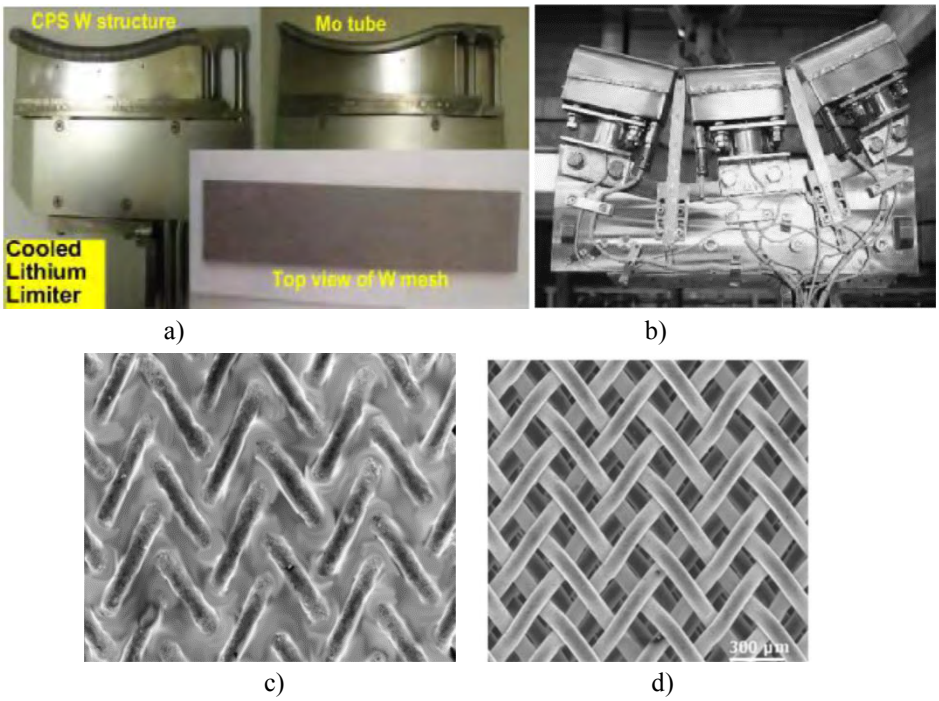

Fig. 1.5 a) CPS device filled with lithium in FTU Frascatti, b) View of complete asembled LLL before installation in FTU, c) Close view of SS mesh filled with Li in FTU adopted from [17, 30], d) CPS based on Mo mesh [50].

Furthermore, later experiments conducted by Russian researchers furtherly contributed to the aforementioned results. Specifically, tests with CPS targets at ELM and disruption simulating conditions with and without Li demonstrated the possibility of a Li based CPS [18, 19]. Currently more experiments with Li CPS are being conducted in China and Kazakhstan [17]. As a result, Li is the most dominant liquid metal for a CPS. Nevertheless, Li has been considered the most appropriate choice for liquid PFMs since the mid of 90s. Since then, experiments with lithium were successfully carried out on the TFTR, T-11M, T-10, CDX-U, FTU, NSTX and TJ-II fusion facilities [49]. Moreover, Golubchikov et al [21] list some reasons for lithium's suitability as a PFM:

- Lithium has a low Z that determines its minimal effect on the main plasma in comparison with any other materials.

- High latent heat of lithium evaporation, radiation and ionization of lithium vapor lead to re-distribution of the important part of incoming energy, thus decreasing power load density on the divertor.
- Helium and other noble gases do not interact with lithium in ordinary conditions.
- Lithium fits well the reactor design with self-cooled lithium–lithium blanket; service systems could be used both for the blanket and the divertor; tritium extraction technology can be the same for both components; the same structure material can be used in those systems - low activated vanadium alloys that are well compatible with lithium at temperatures below 700˚C.
- For low melting metals, lithium has the best physical and thermal properties for application in a liquid metal reactor.

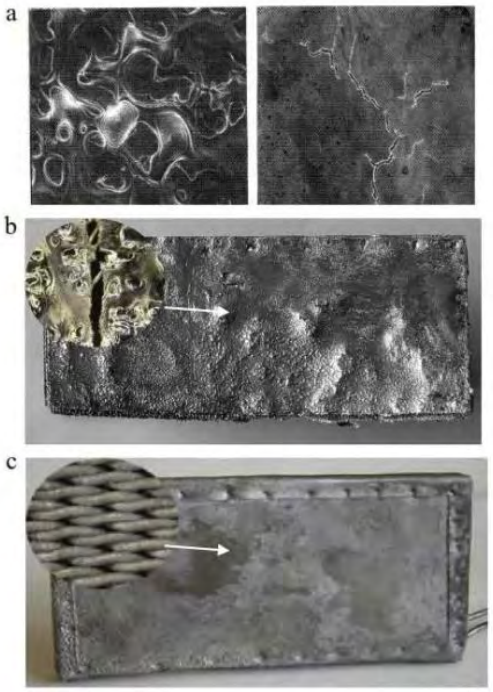

Fig. 1.6 View of Targets tested with irradiation in MK-200UG Russian Facility: a) V alloy after 1 Plasma pulse; b) CPS without lithium after 1 plasma pulse; c) CPS with lithium at 250 ºC after 17 plasma pulses [18].

Besides, it is noteworthy that for the case of a Liquid Li PFC, the formation of a vapor cloud in front of the PFC is observed, which acts like a protective shield reducing the power to the PFC [39, 41]. Apart from the unique combination of Li material properties [21], power exhaust capabilities for fusion reactors with Li as liquid PFM are the highest. In **Fig. 1.8** a), the incoming heat flux for various liquid metals as a function of time is depicted. In the case of Li, it can withstand incoming heat loads of a few hundreds of MW/m^2 at relatively moderate temperatures for fusion environments which are relevant to a fusion reactor Divertor and below its boiling point [19]. Furthermore, Li has a relatively high evaporation rate at temperatures of interest for Plasma Facing Components (PFCs) [17] as it is shown in **Fig. 1.8** b). Accordingly, the selection of lithium as a PFM in PFCs seems to be the optimal choice among other metals such as Hg, Na, Ti and Ga. However, a serious issue from the deployment of Li in fusion devices still remains; Tritium retention and elevated vapor pressure [47].

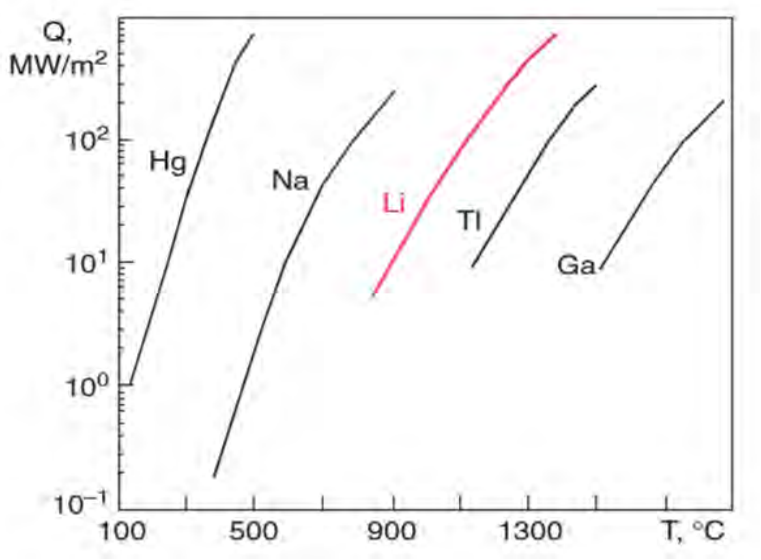

a)

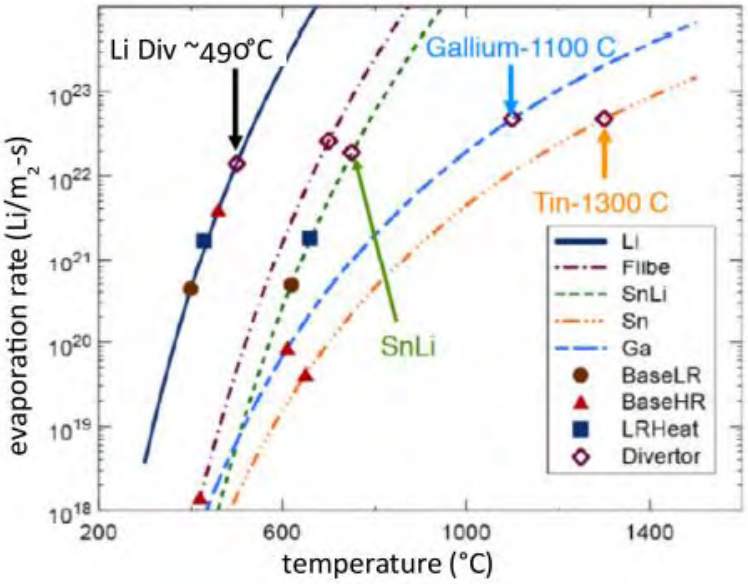

b)

Fig. 1.7 a) Incoming heat flux as a function of temperature for evaporation from a surface to vacuum for various liquid metals proposed for divertor protection [19] and b) evaporation rates for various fusion related liquid metals as a function of temperature [17]. Note that the large rate of Li is observed at the smallest temperatures.

Chapter 2: The Capillary Porous System (CPS)

In the second Chapter of this thesis, some fundamental aspects concerning the proper operation of the CPS as a plasma facing component are presented. Particularly, the fluid mechanical regime behind the liquid flow occupying the region inside the CPS is analyzed via a simplification of the geometry of the porous matrix along with some heat transfer elements. The anticipated effect of an external magnetic field on the flow within a single pore is discussed based on existing numerical results, providing an insight to the results anticipated from this study.

2.1 Operation of the CPS and elements of heat transfer

As it has been mentioned in Chapter 1, the CPS is a capillary pump that acts against the destabilization of the protective thin liquid metal film from electromagnetic and thermal forces inside a fusion reactor chamber. Thus far, ongoing research in experimental facilities such as FTU [30], NSTX [31] and MK-200UG [18] have shown highly promising results. The success of this device relies on particular aspects that need to be known in order to derive a mathematical model describing the liquid metal flow within the porous matrix, which is one of the goals of this thesis.

Once plasma activity is "turned on", an external heat pulse normal to the CPS roof depletes the ultrathin film occupying the top of the porous matrix due to the evaporation process. Besides, liquid lithium included within the porous structures also evaporates at a rate that depends on the intensity [1] and the duration of the incoming heat load. Then, due to capillary phenomena the replenishment process occurs, by pumping liquid metal from the reservoir, as can be seen in **Fig**. **2.1**. In other words, this particular pumping system is self-sustaining and self-regulating as mentioned previously.

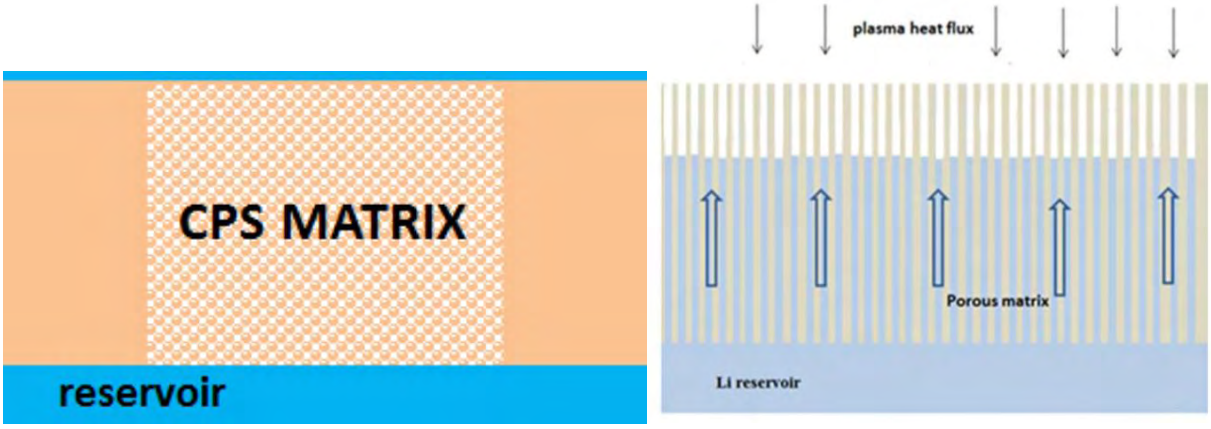

a) b)

Fig. **2. 1** Simple schematic arrangement of the CPS porous matrix with liquid metal resting on top of it. The matrix consists of capillary arteries, forming a complex grid of capillary tubes. b) A simplified schematic of the depletion-replenishment process of the liquid metal trapped within the porous matrix during plasma operation [1].

Furthermore, once the thin liquid metal film formed on the top of the porous matrix evaporates, a different operating CPS regime emerges, that is transpiration cooling. Specifically, a balance between the oncoming specific heat load and a) evaporation of Li captured within the pores, b) heat conduction within the porous matrix and c) convective heat transfer due to the preheating of liquid lithium, from the reservoir temperature up to the temperature of the interface, that is drawn out of the reservoir by capillary action once the top of the CPS is depleted of liquid metal is expected to appear. However, heat convection should be included in a more rigorous and realistic analysis of CPS [1].

2.2 Capillary motion inside a CPS

As it has been stated in Chapter 1, the CPS pumps liquid metal from a reservoir under the influence of various phenomena of fluid mechanical interest, such as gravity, inertia, viscous stresses and Magnetohydrodynamic effects. Principally, the proper operation of a CPS is obtained if the following inequality is satisfied [18-19, 40]:

$$P_c \geq \Delta P_L + \Delta P_F + \Delta P_{MHD} + \Delta P_g + P_r \tag{2.1}$$

where P_c denotes the CPS capillary pressure, ΔP_L – the hydraulic pressure drop in CPS, ΔP_g – the hydrostatic pressure drop, ΔP_F – the pressure drop on the evaporating surface due to liquid – vapor phase transition, ΔP_{MHD} – the pressure drop due to the MHD effect on flowing Li in a magnetic field and P_r is the reservoir pressure (supply system pressure). The driving force behind the CPS operation is the capillary activity since it is the dominant one when compared to the afforementioned phenomena and is due to the fact that its pores are at the micron scale. To be more specific, Lyublinski et al (2015) state that the accepted values for the pore radius are between 20-100 μm and at this length range, P_c can reach the values of 0.2-0.3 MPa and exceeds the sum of the pressures mentioned above. Evtikhin et al. in [40] mention that if full wetting is achieved, P_c can reach 0.5 MPa at acceptable pore sizes. In addition, the sum of these pressures is as high as 10 kPa for a 6 T Tokamak magnetic field [18]. The pressure related to MHD can push liquid out of the porous matrix or even resist its motion depending on the direction of the applied magnetic field. A more detailed analysis of the jxB phenomena met in fluid flow problems can be found in Chapter 3.1

Research on CPS has mainly focused on experiments while few studies concerning mathematical or numerical modelling are available. Specifically, Buhler et al in [32] investigated the flow of liquid lithium within a CPS when a uniform magnetic field is applied considering a complex geometry corresponding to the porous mesh contained in the CPS, simillar to that depicted in **Fig. 2.1** a). Their results showed that when the magnetic field is tranverse to the main velocity component (the component that points towards the pore exit) the pressure drop is increased compared to the hydrodynamic case. As far as static cases are considered, the concept of a single tube, shown in **Fig. 2.2**, was deployed in [1] and [27] in order to study the static arrangement of the liquid lithium resting upon the CPS and investigate the various parameters affecting its shape and thickness, such as the intensity of an imposed electrostatic field, producing fine results compared to existing research. Moreover, in [1] a preliminary study on the hydrodynamic flow of lithium inside a CPS was also conducted.

Following the analysis carried out in [1], in this thesis it is assumed that the CPS is composed of vertical cylindrical tubes with constant pore radius R_p and the flow within a single pore is considered since, without loss of generality, the flow regime within each pore is the same. Although this assumption overestimates the CPS permeability, it provides the foundations for studying the interplay between the forces that act towards or resist the fluid motion within the porous matrix [1].

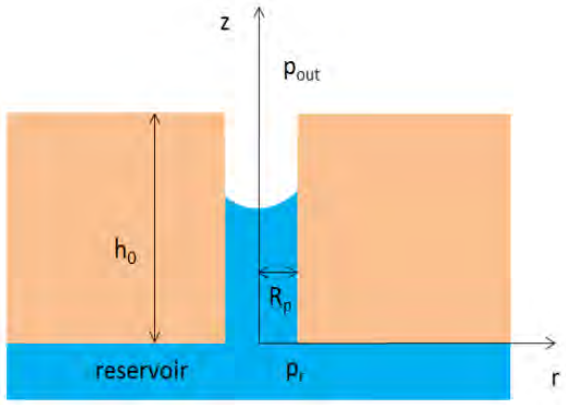

Fig. 2.2 Schematic representation of the flow arrangement within a single capillary pore [1]. The porous matrix is considered to be of rectangular geometry with constant thickness h_0 and constant pore radius R_p.

2.3 The effect of an external magnetic field

Thus far, the mechanism responsible for the replenishment process inside the porous matrix of a CPS was investigated from the perspective of fluid mechanics and heat transfer theory. However, it is a well-established fact that a CPS positioned inside a fusion reactor chamber will be exposed to strong magnetic fields. These fields are expected to induce electrical currents inside the flowing liquid metal and subsequently electromagnetic forces that need to be taken into account in any numerical simulation of CPS related flows, known as Lorentz forces. The aforementioned forces, the so-called "jxB effects", are anticipated to produce an additional effective overpressure since the liquid pressure field will be augmented by the magnetic pressure [2]. More information about this kind of pressure and its mathematical reasoning will be discussed thoroughly in Chapter 3.1. The magnitude of this overpressure and the flow configuration depend on the magnetic field intensity [32], the direction of the field and the electric currents that enter the liquid via its interface, as it depicted in **Fig. 2.3**. Benos in [1] studied static cases in which the applied field lied across the azimuthial direction, **Fig. 2.3**, in an attempt to find out under which circumstances drop ejection can appear. His analysis showed that static configurations of the liquid lithium within the pore could not be obtained for relatively large magnetic pressures if a fixed contact angle, the angle at which the liquid column approaches the capillary pore wall, is considered. For this reason, a dynamic analysis considering the full dynamics of the liquid column within the pore under the effect of the aforementioned magnetic field and a constant contact angle is essential, which is the main subject of this thesis. The analysis is expected to verify some phenomena observed in [1] and [32]. However, before proceeding to the mathematical modelling concerning the replenishment process in the presence of a magnetic field, it is reasonable to

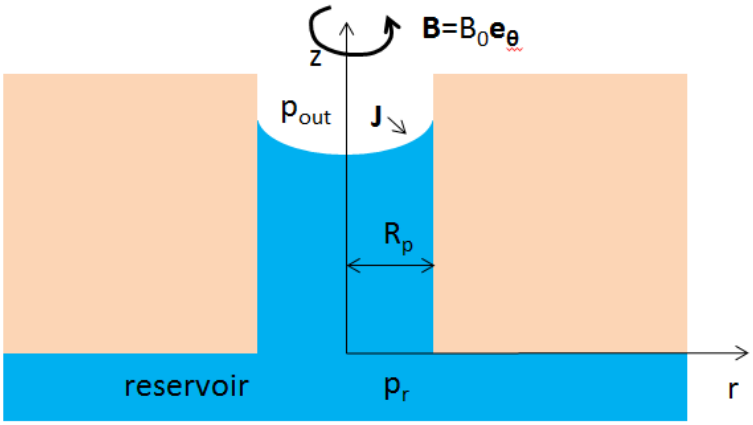

Fig. 2.3 Schematic of the geometry concerning the replenishment problem under the influence of a static magnetic field applied in the azimuthial direction. Note the electric current J, produced by plasma activity, entering the liquid column rising inside the capillary tube.

present some basic theoretical aspects of the flow of electrically conducting fluids and, more precisely, of liquid metals inside a magnetic field. The basic theory concerning flows of liquid metals under the influence of any magnetic field is presented in Chapter 3.1.

Chapter 3: Effect of an imposed magnetic field

In this Chapter, the fundamental physics and mathematical equations needed to study and interpret the flow of conducting and incompressible fluids are presented. The basic Maxwell equations along with Ohm's law are coupled with the fluid velocity field in order to produce an augmented transport equation for the electromagnetic variable chosen. Furthermore, some existing approaches based on the selection of different electromagnetic variables for the coupled problem are also included. The main assumptions of the problem under investigation pertaining to the applied magnetic field along with the derivation of the differential equation describing the induced magnetic field and boundary conditions are presented.

3.1 Basics of Magnetohydrodynamics

The problem under consideration is concerned with the capillary rise of a liquid metal within a pore of constant radius under the effect of an imposed magnetic field. Therefore, it is reasonable enough to use a mathematical model that incorporates the influence of the aforementioned field on the liquid flow. This model is based on the Magnetohydrodynamics theory. Magnetohydrodynamics (MHD for short) is concerned with the study of the dynamics of electrically conducting fluids and specifically with those effects that arise through the interaction of the motion of the fluid under consideration and any magnetic field [2, 9]. The fluid under investigation must be electrically conducting and non-magnetic. MHD has found application in many different subjects of practical and theoretical interest such as metal casting [9], crystal growth [13], plasma containment and flow in fusion reactors [2, 10, 14, 24] and Astrophysics [9, 24]. Other examples of technological and industrial applications of electrically conducting fluids include MHD pumps, flow-meters, generators and propulsion devices [2, 24].

From the numerous applications above, the one of the highest significance is perhaps controlled fusion. As mentioned in Chapter 1, LM film flows under Magnetic Fields and especially open surface flows have found considerable application in Fusion reactors as cooling concepts by evaporation and heat conduction to a substrate [17]. These concepts have stemmed from the idea that LM flows can act as coolants and PFCs [45] extracting high heat fluxes from the plasma chamber of a future fusion reactor while they interact with plasma confinement magnetic fields. At the same time, solid structural elements of the chamber wall are protected from extreme thermal stresses and sputtering erosion. However, it has been discovered that in open surface flows of conducting liquids, such as Li and Sn, the mean film height tends to increase and be distorted towards the free surface. In other words, the interaction of generated stream wise currents and the applied transverse field results in LM being pulled way towards the plasma [3, 7, 25] and maximum velocity is increased when compared to zero field cases [3, 7]. The resulting distortion and flow patterns strongly depend on the field intensity and the type of the LM used [3]. However, the above tendencies give rise to significant

concerns about the interfacial stability since large interfacial deformations may lead to drop ejection or flow detachment.

The mathematical modelling of MHD flows consists of the typical Navier - Stokes equations with an additional term corresponding to the Lorentz Force and an extra set of equations derived from Maxwell's Equations, specifically Ohm's Law, Ampere's Law and Faraday's Law. As it has been stated previously, liquid lithium is an electrically conducting fluid and flows under the influence of a static and transverse magnetic field inside the CPS porous matrix. Consequently, the interaction of the motion of the fluid and the applied magnetic field will give rise to electrical currents. The aforementioned induced currents must, according to the well-known Ampere's Law, give rise to a second magnetic field, namely the induced magnetic field.

The total field **B** (imposed plus induced) interacts with the induced current density, $\mathbf{J}$, and gives rise to a Lorentz force of

$$\boxed{\mathbf{f}_L = \mathbf{J} \times \mathbf{B}} \tag{3.1}$$

The Lorentz Force is the mechanical force exerted on the fluid particles as a result of the mutual interaction of **J** and **B**. Based on the definition of this force, it is explicitly deduced that it tends to accelerate or decelerate a fluid element in the normal direction of magnetic field and electric current, as depicted in **Fig 3.1**. Besides, it should be noted that $\mathbf{f}_L$ is a body force (force per unit volume) and acts as a source term in the Navier-Stokes equations, which are discussed in detail in Chapter 4. The induced electric current **J** is given by Ohm's Law:

$$\boxed{\mathbf{J} = \sigma(\mathbf{E} + \mathbf{u} \times \mathbf{B})} \tag{3.2}$$

where **E** is the electric field produced by the fluid velocity, **u**, and **B** the combined magnetic field. Furthermore, the induced current is given by Ampere's Law which states that

$$\boxed{\mu_m \mathbf{J} = \nabla \times \mathbf{B},\ \nabla \cdot \mathbf{B} = 0} \tag{3.3}$$

Combining Eq.3.2 with Eq.3.3 and having in mind that $-\partial \mathbf{B} / \partial t = \nabla \times \mathbf{E}$, yields the following relation, known as the Induction equation:

$$\boxed{\frac{\partial \mathbf{B}}{\partial t} = \nabla \times (\mathbf{u} \times \mathbf{B}) + \frac{1}{\mu_m \sigma} \nabla^2 \mathbf{B}} \tag{3.4}$$

The main advantage of the above equation is that it directly relates the main hydrodynamic quantity, the velocity field, **u**, to the main electromagnetic one, the external magnetic field, as it is underlined in [26]. Moreover, it ensures the fact that the interaction of the fluid flow with the magnetic field acts as the source of the induced field in the above diffusion-like equation. This so-called source term is the magnetic advection, the curl term in the Induction equation.

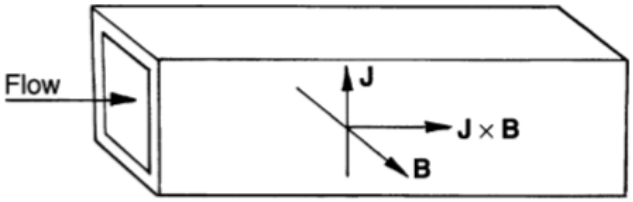

Fig 3. 1. A schematic representation of the direction of the Lorentz force exerted on a unidirectional flow inside a rectangular duct. Vectors **J**, **B** are perpendicular to each other and, as a result of the definition of the Lorentz Force, **J**x**B** is perpendicular to the duct cross section [2].

As far as the Lorentz force is concerned, it can be replaced by an imaginary set of stresses [1-2].

$$\boxed{\mathbf{f}_L = \nabla \cdot \left[\frac{\mathbf{BB}}{\mu_m} - \frac{|\mathbf{B}|^2}{2\mu_m} \underline{\underline{\mathrm{I}}} \right] = \frac{1}{\mu_m} (\mathbf{B} \cdot \nabla)\mathbf{B} - \nabla \left(\mathbf{B}^2 / 2\mu_m \right)} \tag{3.5}$$

The second rank tensor $\frac{\mathbf{BB}}{\mu_m} - \boldsymbol{\nabla}(\frac{\mathrm{B}^2}{2\mu_m})$ represents the Maxwell stresses and $\underline{\underline{\mathrm{I}}}$ is the unit tensor.

At this point, it is necessary to define a nondimensional number, fundamental to MHD, the Magnetic Reynolds number, $\mathrm{R_m}$. This parameter is defined as

$$R_m = \sigma \mu_m u L$$

where μ_m stands for the magnetic permeability and σ, u, L are electrical conductivity, characteristic velocity and length scale, correspondingly.

The magnetic Reynolds number stands for the ratio of advection, the first term on the right scale of Eq**.** 3.4, over diffusion, the second term on the right scale of Eq. 3.4, of the magnetic field **B**. Besides, another qualitative definition of $\mathrm{R_m}$ is the ratio of induced magnetic field over the applied field. For conducting fluids such as liquid metals, $\mathrm{R_m}$ is typically of the order 10^{-3}-10^{-1} [2] and is the domain of Liquid Metal MHD in most cases of practical importance [9]. Under these circumstances, diffusion dominates over advection in Eq. 3.4, implying that the first term on the right scale is much smaller than the second term.

Consequently, in the case that $\mathrm{R_m} << 1$, the induced magnetic field is negligible in comparison with the imposed field and it is proved that the produced electric field, **E**, is irrotational and can be deduced from a scalar potential φ [2, 24]. Then, Eq. 3.1- 3.2 are as follows:

$$\boxed{\mathbf{J} = \sigma(-\nabla\varphi + \mathbf{u} \times \mathbf{B}_0)} \tag{3.6}$$

and the electromagnetic force per unit volume reads as

$$\boxed{\mathbf{f}_L = \mathbf{J} \times \mathbf{B}_0} \tag{3.7}$$

Taking the divergence of the relation above leads to a Poisson equation for the electric potential

$$\boxed{\nabla^2 \varphi = \nabla \cdot (\mathbf{u} \times \mathbf{B}_0)} \tag{3.8}$$

where $\nabla \cdot \mathbf{J} = 0$ due to electric charge conservation. This model is known as the *low magnetic Reynolds number approximation* (low-R_m model), widely used in liquid metal MHD flows in Fusion reactor environments [2, 10, 24] and Crystal Growth [13]. However, this is not always the case since in applications relevant to controlled Fusion, plasma disruptions and edge-localized modes may result in considerable electromagnetic interactions in the liquid metal, which cannot be dealt with the low-R_m approximation [11]. In general, the *φ formulation* (Eq. 3.8) is less complex and the required calculations are less than those needed in the full MHD model (Eq. 3.5) since less assumptions are made and the induced magnetic field is neglected [15]. However, it is less consistent with physical reality while the full MHD model can been used for low and even moderate R_m [11, 15]. Besides, it has been shown that in some MHD cases the results between the low-R_m approximation and the Induction formulation differ significantly [12, 15].

To this end, the two formulations mentioned above and combinations of them are the main approaches in order to mathematically describe the flow of any liquid metal, provided that R_m is sufficiently low. The first, namely the *B-formulation*, uses the total magnetic field B as the main electromagnetic variable whereas the *φ-formulation* implements the electrostatic potential *φ*. In this regard, the existence of other approaches for the coupling is also noteworthy. For instance, one of them was proposed by Smolentsev et al in which the electromagnetic variable was the induced electric current density [6], providing accurate results compared with existing research. Nevertheless, every mathematical approach carries out the coupling of the electromagnetic part with the fluid velocity field u.

3.2 Derivation of the Lorentz Force and Magnetic Induction Equation

In the present thesis, it is assumed that there are no external electrostatic fields ($\nabla \varphi = 0$) and the applied magnetic field lies along the azimuthial direction with constant magnitude $\mathbf{B}_0 = B_0 \mathbf{e}_\theta$ and, hence, only the effect of a constant applied magnetic field on the flow configuration is investigated. Also, a cylindrical coordinate system is chosen, with its center positioned in the middle of the entrance of the pore (**Fig. 2.3**). The current density is then expressed through a simplified form of Ohm's law:

$$\mathbf{J} = \sigma(\mathbf{u} \times \mathbf{B}) \tag{3.9}$$

where σ is the electric conductivity of the fluid, **B** the total magnetic field and **u** the liquid metal velocity field inside the pore. According to Maxwell, there are no magnetic monopoles (Gauss law in Eq. 3.3). As a consequence, the divergence of the imposed magnetic field, $\mathbf{B}_0 = B_0 \mathbf{e}_\theta$, is:

$$\nabla \cdot \mathbf{B_0} = \nabla \cdot (B_0 \mathbf{e_\theta}) = \frac{1}{r}\frac{\partial B_0}{\partial \theta} = 0 \tag{3.10}$$

However, the curl of $\mathbf{B}_0$ is nonzero:

$$\nabla \times \mathbf{B}_0 = \frac{1}{r}\frac{\partial (rB_0)}{\partial r}\mathbf{e_z} = \frac{B_0}{r}\mathbf{e_z} \neq \mathbf{0} \tag{3.11}$$

fact that implies an induced current according to Ampere's Law. Based on the analysis of Gao and Morley [3, 25], Smolentsev [6, 7] and using the fact that the magnetic Reynolds number is significantly less than unity, the total magnetic field can be decomposed into the applied and induced parts, respectively.

$$\mathbf{B} = \mathbf{B}_0 + \mathbf{B}_i \tag{3.12}$$

such that $|\mathbf{B}_i| \ll |\mathbf{B}_0|$. However, according to Ampere's Law, the induced electric current can also be computed from the following relation [1, 3].

$$\boxed{\mathbf{J} = \frac{1}{\mu_m}\nabla \times \mathbf{B}_i = \nabla \times \mathbf{H}} \tag{3.13}$$

Where $\mathbf{H} = \mathbf{B}_i / \mu_m$ represents the magnetic induction and serves as a stream function for the emerging electric current, so that any spurious currents associated with a rotational applied magnetic field can be avoided [1]. Moreover, Eq. 3.13 makes use of magnetic induction, **H**, as the main electromagnetic variable and not $\mathbf{B}_i$ since an additional parameter including the liquid's magnetic permeability μ_m (R_m for instance) is not needed, as stated by Morley et al in [3]. At this particular point, it should be stressed that a rotational $\mathbf{B_0}$ does not correspond to a realistic magnetic field in a fusion reactor divertor, however, it is chosen as such in order to avoid a 3D MHD model.

Since the condition $R_m << 1$ holds, the magnitude of *H* will satisfy the following condition:

$$B_i \ll B_0 \Leftrightarrow \mu_m H \ll B_0 \tag{3.14}$$

and vector **H** is considered to lie along the azimuthial direction, i.e. $\mathbf{H} = H\mathbf{e_\theta}$, the Lorentz force reads as

$$\mathbf{f}_L = \mathbf{J} \times \mathbf{B}_0 = (\nabla \times \mathbf{H}) \times \mathbf{B}_0 = \left[-\frac{\partial H}{\partial z}\mathbf{e_r} + \frac{1}{r}\frac{\partial (rH)}{\partial r}\mathbf{e}_z \right] \times B_0 \mathbf{e_\theta} \Rightarrow$$

$$\mathbf{f}_L = -\frac{\partial H}{\partial z} B_0 \mathbf{e}_z - \frac{B_0}{r}\frac{\partial (rH)}{\partial r}\mathbf{e_r} = -\frac{\partial H}{\partial z} B_0 \mathbf{e}_z - \frac{\partial H}{\partial r} B_0 \mathbf{e}_r - \frac{B_0 H}{r}\mathbf{e}_r \tag{3.15}$$

Keeping in mind the fact that B_0 is spatially constant and that the del operator is $\nabla = \frac{\partial}{\partial r}\mathbf{e_r} + \frac{\partial}{\partial z}\mathbf{e}_z$, the latter expression can be written as follows:

$$\mathbf{f}_L = -\nabla(B_0 H) - \frac{B_0 H}{r}\mathbf{e}_r \tag{3.16}$$

In addition, Ohm's law from Eq. 3.9 is equated with the expression provided by Eq. 3.13:

$$\begin{aligned}
&\sigma(\mathbf{u}\times\mathbf{B}) = \nabla\times\mathbf{H} \Rightarrow \\
&\nabla\times[\sigma(\mathbf{u}\times\mathbf{B})] = \nabla\times\nabla\times\mathbf{H} \Rightarrow \\
&\sigma(\nabla\times\mathbf{u}\times\mathbf{B}) = \nabla(\nabla\cdot\mathbf{H}) - \nabla^2\mathbf{H} \Rightarrow \\
&\sigma[\mathbf{u}(\nabla\cdot\mathbf{B}) - \mathbf{B}(\nabla\cdot\mathbf{u}) + (\mathbf{B}\cdot\nabla)\mathbf{u} - (\mathbf{u}\cdot\nabla)\mathbf{B}] = -\nabla^2\mathbf{H}
\end{aligned} \tag{3.17}$$

where the vector identity $\nabla\times\nabla\times\mathbf{H} = \nabla\left(\nabla\cdot\mathbf{H}\right) - \nabla^2\mathbf{H}$ has been used and $\nabla\cdot\mathbf{H} = \nabla\cdot\mathbf{B} = 0$ due to the solenoidality of the magnetic field. Moreover, the liquid metal is incompressible and according to continuity equation the constrain $\nabla\cdot\mathbf{u} = 0$ holds. As a result, the latter equation is simplified:

$$-(\mathbf{B}\cdot\nabla)\mathbf{u} + (\mathbf{u}\cdot\nabla)\mathbf{B} = \frac{\nabla^2\mathbf{H}}{\sigma} \tag{3.18}$$

Since $\mathbf{H} = H\mathbf{e_\theta}$, the right scale of the above equation is:

$$\begin{aligned}
&\nabla^2\mathbf{H} = \nabla^2(H\mathbf{e_\theta}) = \left[\frac{\partial}{\partial r}\left(\frac{1}{r}\frac{\partial(rH)}{\partial r}\right) + \frac{\partial^2 H}{\partial z^2}\right]\mathbf{e_\theta} = \left[\frac{\partial^2 H}{\partial r^2} + \frac{1}{r}\frac{\partial H}{\partial r} + \frac{\partial^2 H}{\partial z^2} - \frac{H}{r^2}\right]\mathbf{e_\theta} \Rightarrow \\
&\nabla^2\mathbf{H} = (\nabla_\perp^2 H - \frac{H}{r^2})\mathbf{e_\theta}
\end{aligned} \tag{3.19}$$

For the sake of simplicity, since $\perp$ denotes the r-z plane and the induced currents are coplanar with the fluid velocity field, the $\perp$ is dropped: $\nabla_\perp^2 \equiv \frac{\partial^2}{\partial r^2} + \frac{1}{r}\frac{\partial}{\partial r} + \frac{\partial^2}{\partial z^2} \equiv \nabla^2$

The left scale reads as:

$$-(\mathbf{B}\cdot\nabla)\mathbf{u} + (\mathbf{u}\cdot\nabla)\mathbf{B} = (v\frac{\partial}{\partial r} + u\frac{\partial}{\partial z})(B_0 + B_i)\mathbf{e_\theta} - \frac{B_0 + B_i}{r}\frac{\partial}{\partial\theta}(u\mathbf{e}_z + v\mathbf{e_r}) = -B_0\frac{v}{r}\mathbf{e_\theta} \tag{3.20}$$

since only the two basis vectors $\mathbf{e_r}$ and $\mathbf{e_\theta}$ are θ dependent. The two velocity components are coplanar with the r z plane and, thus $\frac{\partial(u,v)}{\partial\theta} = 0$. Besides, since the condition provided by Eq. 3.14 holds, then $B_0 + B_i \approx B_0$.

Finally, the expression for the magnetic induction, H, is derived [1]:

$$\frac{1}{\sigma}(\nabla^2 H - \frac{H}{r^2})\mathbf{e_\theta} = -B_0 \frac{v}{r}\mathbf{e_\theta} \Rightarrow$$

$$\boxed{\nabla^2 H - \frac{H}{r^2} = -\sigma B_0 \frac{v}{r}} \qquad (3.21)$$

Note that this relation is a second order differential equation in cylindrical coordinates and does not contain any first order partial derivatives containing both the magnetic field and the velocity field. Besides, it is consistent with the steady state form of Eq. 3.4, where B now is the flow induced field. This is a direct consequence of the low R_m as previously mentioned at Section 3.1

Lithium is a paramagnetic material. Paramagnetic materials are slightly attracted by a magnetic field and the material does not retain the magnetic properties when the external field is removed. Paramagnetic materials have positive susceptibility that is slightly above unity. For liquid lithium $\chi_{m,Li} = 1.4\text{x}10^{-5}$ so $\mu_m = \mu_o(1+\chi_{m,Li}) = 4.000056\pi$ x 10^{-7} N/A^2 where μ_o is the magnetic permeability of vacuum. In a Fusion Reactor environment the magnetic field intensity can reach values B_0 = O(1) T and according to [1] the characteristic value for H is R_pJ_r where R_p is the pore radius and its value according to [18] is R_p = O(10) μm and J_r is the radial current density component at the interface which can reach values up to 10^9 A/m^2 according to [1]. Then, according to Eq. 3.12 we have for the induced field

$$B_i = \mu_m H \sim 10^{-3}\ \text{T} << B_0$$

The above calculation validates the previous assumptions.

Returning to the induction equation derived above, appropriate boundary conditions pertaining to H have to be incorporated using cylindrical coordinates in order to conform with the geometry of the pore, as depicted in **Fig 3.2**. Those boundary conditions are summarized below:

At the right boundary the pore wall is considered electrically insulated, thus

$$r = R_p,\ \ 0 \le z \le f(r):\ \mathbf{J}\cdot\mathbf{e_r} = J_r = 0 \qquad (3.22)$$

Also, at r = 0 symmetry conditions are imposed:

$$r = R_p:\ J_r = 0 \Rightarrow -\frac{\partial H(r=0,z)}{\partial z} = 0 \Rightarrow H(r=0,z) = const. \qquad (3.23)$$

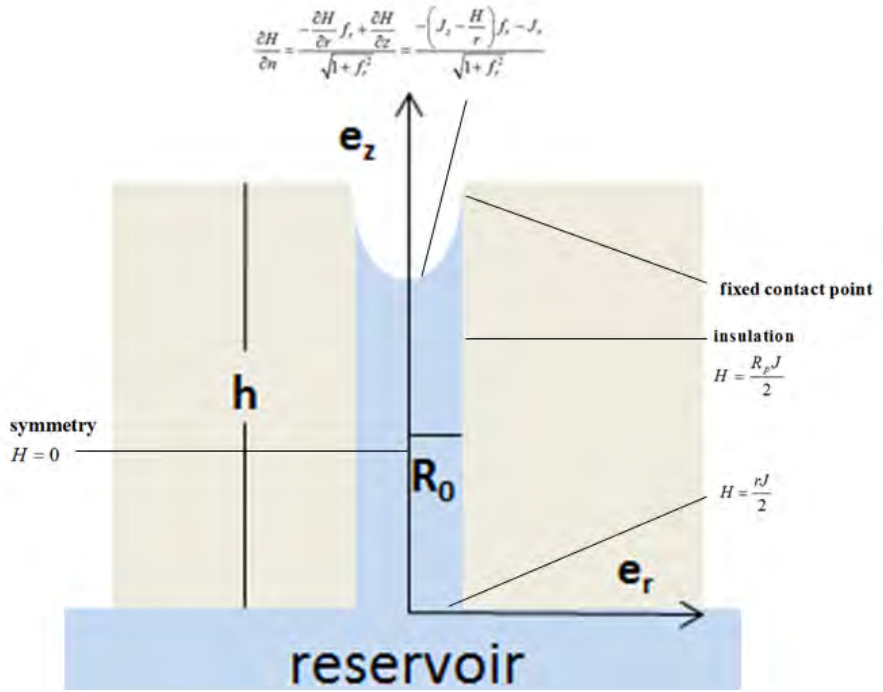

Fig. 3.2 A schematic representation of the geometry of the problem along with the Boundary Conditions. The contact angle does not change. However, its vertical position changes with time as the liquid column rises and grad-ually fills the pore. The geometry corresponds to half of the cylindrical pore since symmetry along x-axis is assumed.

At the interface $z = f(r)$ a known current density is imposed:

$$\mathbf{J} = J_r \mathbf{e}_\mathbf{r} + J_z \mathbf{e}_z \tag{3.24}$$

At the pore entrance z = 0 the current density takes a constant value, J, and can be calculated via charge conservation based on the assumption of eletrically insulated side walls:

$$\iint_{z=0} (\mathbf{J}\cdot\mathbf{n})\,dA = \iint_{z=f(r)} (\mathbf{J}\cdot\mathbf{n})\,dA \Rightarrow$$

$$J\left(\pi R_p^{\,2}\right) = \int_0^{2\pi}\int_0^{Rp} (J_z - J_r f_r)\, r\,dr\,d\theta \Rightarrow$$

$$\boxed{J = \frac{2}{R_p^{\,2}}\int_0^{R_p} (J_z - J_r f_r)\, r\,dr} \tag{3.25}$$

Moreover, we have at z = 0:

$$J_r = 0 \Rightarrow H = H(r) \tag{3.26}$$

$$J_z = J \Rightarrow J = \frac{1}{r}\frac{\partial(rH)}{\partial r} \Rightarrow H = \frac{rJ}{2} + \frac{a}{r} \overset{a=0}{\Rightarrow} H = \frac{rJ}{2} \tag{3.27}$$

Finally, at $r = R_p$ and $0 \le z \le f(r)$ we have that:

$$H\left(r = R_p, z\right) = \frac{R_p J}{2} \tag{3.28}$$

while at *r = 0:*

$$H\left(r = 0, z\right) = 0 \tag{3.29}$$

At the interface, a Robin-type boundary condition is imposed [1].

$$\frac{\partial H}{\partial n} = \nabla H \cdot \mathbf{n} = \frac{-\frac{\partial H}{\partial r} f_r + \frac{\partial H}{\partial z}}{\sqrt{1 + f_r^{\,2}}} = \frac{-\left(J_z - \frac{H}{r}\right) f_r - J_r}{\sqrt{1 + f_r^{\,2}}} \tag{3.30}$$

At this particular point, the boundary value problem derived above describes the spatial distribution of the induced magnetic field through the scalar H(r, z). The latter serves as a stream function for the induced current since each of its components is deduced via calculating first order derivatives of H, according to Eq. 3.13. In addition, the right scale of Eq. 3.22 includes the radial velocity component, v, implying the fact that the magnetic induction distribution depends on the fluid motion; if there is no motion (i.e. u, v = 0) there is no coupling between velocity and the electromagnetic variable of the problem. As it has been previously stated, the boundary value problem described by Eq. 3.22 through 3.32 is going to be coupled with the Navier – Stokes equations (the momentum related equations) along with appropriate boundary conditions in order to fully describe the problem of the liquid column rising inside the pore.

Chapter 4: Mathematical description of the problem

In the following chapter we are concerned with the mathematical modeling of the replenishment process taking into account the mathematical formulation derived in Chapter 3 for the induced magnetic field. Specifically, the boundary value problem derived in the previous Chapter is coupled with the Navier-Stokes and continuity equations producing a MHD system describing the lithium capillary rise with appropriate boundary and initial conditions. Finally, the system derived is rendered non dimensional.

4.1 Basics of capillary phenomena

Phenomena concerning fluid statics or fluid flow in which surface tension plays a significant role are known as capillary phenomena, although there may be no capillary tube in sight [16]. In Capillary Dynamics (flows with low Reynolds number), the phenomenon in which a liquid rapidly penetrates into a small-diameter tube under the action of surface tension is known as 'Wicking'. The reason behind this frequently observed phenomenon is surface tension and liquid is drawn into the tube only if it wets the tube material. The term ''wetting'' refers to the observation of an equilibrium contact angle less than 90°. The simplest model of wicking is based upon the flow of liquid into a long straight and vertical capillary, as shown in **Fig. 4.1**. The driving force for wicking is the capillary pressure, p_c, which, for a capillary of small radius, is well approximated by using the Young-Laplace equation. The meniscus is assumed to be a part of a hemispherical surface of radius $R_p/\cos\theta$ where θ is the dynamic contact angle. It is worth mentioning that the dynamic angle is generally non-zero [16]. Thus, we have for capillary pressure

$$p_c = -\frac{2\gamma}{R_p}\cos\theta \tag{4.1}$$

where γ is the surface tension of the liquid. Note the '-' sign on the pressure. The pressure is reduced by the (negative) curvature of this meniscus as one passes from the ambient medium just above the meniscus into the liquid. In addition, the dynamic contact angle is generally different from the equilibrium contact angle θ [16, 42]. However, throughout this thesis the dynamic contact angle is assumed constant and equal to θ_c for simplicity. The capillary is assumed to be vertical with constant radius $r = R_p$, as depicted in **Fig. 4.1**. The liquid flows against gravity. Therefore, the net pressure driving force is given by the following simple formula [16].

$$\Delta p = -\frac{2\gamma}{R_p}\cos\theta + \rho g h \tag{4.2}$$

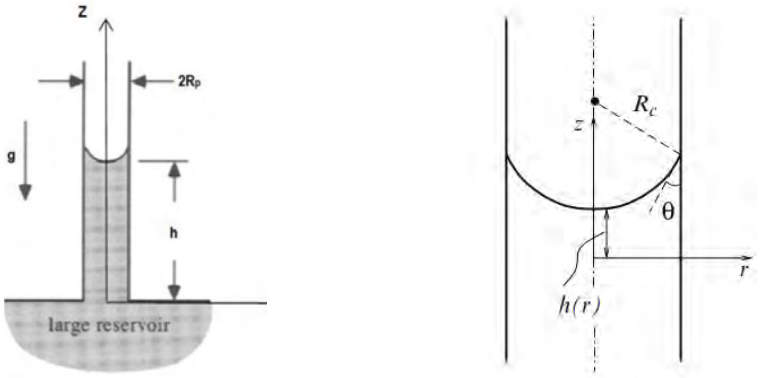

Fig. 4.1 Schematic representation of the wicking process within a typical capillary tube of radius Rp. Note that θ is the contact angle with the capillary lateral wall and h the equilibrium height which is reached in static arrangement. The liquid gas interface in presented by a function of radial distance r, h(r), and Rc = Rp/cosθ [16, 20, 42]**.**

Here, h is height of rise measured from the surface of the reservoir. When static equilibrium is achieved, the equilibrium height h is given by the following formula [8]

$$h_{eq} = \frac{2\gamma}{\rho g R_p}\cos\theta \tag{4.3}$$

with θ denoting the equilibrium contact angle. It is of importance to stress the dependence of the equilibrium interface shape on the physical properties of the solid boundary [42]. Despite the profound simplicity of the model of a single vertical tube, many porous media models consider the dynamics of a single cylindrical capillary and knowledge of the latter is still of importance [43, 44]. One of the simplest models for the penetration of a liquid inside a capillary tube is the so-called Lucas-Washburn equation [16, 43, 44], in which the vertical height reached by the meniscus, h, is proportional to $t^{1/2}$.

$$h = \sqrt{\frac{\gamma R_p \cos\theta}{2\mu} t} \tag{4.4}$$

The above relation is derived under the assumption that only the surface tension force at the meniscus and the friction force inside the straight tube are present [43]. Inertia is excluded. Hence, the liquid column height increases continuously until static equilibrium is established.

4.2 Mathematical Modeling of the Replenishment process

As far as the problem under investigation is concerned, the reservoir continuously delivers liquid metal via wicking into the porous matrix without applying any external pressure. As a consequence, the nature of the problem under consideration is purely dynamic. The pore contained in the porous matrix is considered to be a long straight cylindrical capillary tube of radius R_p which is in contact with the reservoir (z = 0 plane) that provides the liquid metal at constant pressure p_r, as depicted in **Fig. 3.2**. The liquid metal flow is assumed to be isothermal and evaporation effects are neglected.

Furthermore, its material properties such as density, dynamic viscosity, electric conductivity and surface tension, are assumed to be constant throughout the region it occupies within the pore.

If $\mathbf{u}=u\mathbf{e_z}+v\mathbf{e_r}$ represents the velocity field of the liquid within the pore then the flow arrangement of the liquid metal is determined by the momentum equation, also known as *Cauchy's first law of motion* [20], along with continuity equation for incompressible flows:

$$\rho\frac{D\mathbf{u}}{Dt}=\nabla\cdot\underline{\underline{T}}+\mathbf{f} \tag{4.5}$$

$$\nabla\cdot\mathbf{u}=0 \tag{4.6}$$

where $\underline{\underline{T}}=-p\underline{\underline{I}}+\underline{\underline{\tau_v}}$ is the stress tensor of the fluid, p is the fluid pressure, $\underline{\underline{I}}$ is the unit tensor and $\underline{\underline{\tau_v}}$ represents the viscous stress tensor. Besides, D/Dt is the material derivative and is defined as $D/Dt\equiv\partial/\partial t+\mathbf{u}\cdot\nabla$. Vector $\mathbf{f}$ denotes the force per unit volume exerted on a fluid element by external fields. In the present thesis, the only body forces considered are gravity and Lorentz forces arising from the fluid's interaction with the externally applied magnetic field $\mathbf{B}_0$. In that case, $\mathbf{f}$ is given by

$$\mathbf{f}=\mathbf{f_g}+\mathbf{f_L}=\rho\mathbf{g}+\mathbf{f_L}=\rho\mathbf{g}+\mathbf{J}\times\mathbf{B}_0 \tag{4.7}$$

In the expression above, $\mathbf{g}$ is the acceleration due to gravity and $\mathbf{J}$ the induced electric current density. According to **Fig. 3.2** the body force due to gravity acts only along the axial direction z, hence $\mathbf{f}_g=-\rho g\mathbf{e_z}$ whereas the analytical expression for the Lorentz force was derived and discussed in detail in Chapter 3. It is to be underlined that this force is the manifestation of the MHD effect on the liquid flow. Moreover, the liquid metal is assumed to be Newtonian with constant dynamic viscosity μ so that the viscous stresses are given by the well-known constitutive equation.

$$\underline{\underline{\tau_v}}=\mu\left(\nabla\mathbf{u}+\nabla\mathbf{u}^{\mathrm{T}}\right) \tag{4.8}$$

where $\nabla\mathbf{u}$ is the velocity gradient and μ denotes the dynamic viscosity.

To this end, the momentum equation is solved by taking into consideration the time-dependent term included in the material derivative, i.e. $\rho D\mathbf{u}/Dt=\rho\partial\mathbf{u}/\partial t+\rho(\mathbf{u}\cdot\nabla)\mathbf{u}$, assuming a time dependent pattern with the dynamics of the rising fluid following the time evolution of the meniscus.

By combining Eq. 4.4, 4.6**,** 4.7 and 3.16 we have for momentum transfer:

$$\rho\frac{\partial\mathbf{u}}{\partial t}+\rho(\mathbf{u}\cdot\nabla)\mathbf{u}=-\nabla p+\nabla\cdot\underline{\underline{\tau_v}}+\rho\mathbf{g}-\nabla(B_0H)-B_0\frac{H}{r}\mathbf{e_r}\Rightarrow$$

$$\rho\frac{\partial \mathbf{u}}{\partial t}+\rho(\mathbf{u}\cdot\nabla)\mathbf{u}=-\nabla(p+\rho gz)-\nabla(B_0H)+\nabla\cdot\underline{\underline{\tau_v}}-B_0\frac{H}{r}\mathbf{e_r}\Rightarrow$$

$$\rho\frac{\partial \mathbf{u}}{\partial t}+\rho(\mathbf{u}\cdot\nabla)\mathbf{u}=-\nabla(p+\rho gz+B_0H)+\nabla\cdot\underline{\underline{\tau_v}}-B_0\frac{H}{r}\mathbf{e_r} \tag{4.9}$$

From the aforementioned expression for momentum, it is deduced that jxB forces have a direct impact on the fluid pressure field. To be more specific, it has been proved in the previous chapter that $\mathbf{J}\times\mathbf{B}_0=-\nabla(B_0H)-(B_0H/r)\mathbf{e_r}$ in which the first term acts in the same way as pressure does (pressure dependence is expressed via $\nabla(p+\rho gz)$) and, thus, augments the liquid pressure. For this reason, B_0H is called the magnetic pressure [2].

Generally, the magnetic pressure is written as $p_m=(2\mu_m)^{-1}B^2$ [2, 9], however, it does not affect the fluid flow inside the pore. Therefore, the Lorentz force is simply written as

$$\mathbf{f}_L=-\frac{B_0H}{r}\mathbf{e}_r \tag{4.10}$$

on the understanding that pressure is augmented by B_0H. Accordingly, a modified pressure function is introduced

$$\wp=\underbrace{p_l}_{\text{Liquid pressure}}+\underbrace{\rho gz}_{\text{Hydrostatic pressure}}+\underbrace{B_0H}_{\text{Magnetic pressure}} \tag{4.11}$$

with p_l representing the difference $p-p_r$, ρgz expresses the hydrostatic part of the pressure field and B_0H the magnetic pressure.

Consequently, the momentum equation can be written in the form:

$$\underbrace{\rho\frac{\partial \mathbf{u}}{\partial t}}_{\text{Local acceleration}}+\underbrace{\rho(\mathbf{u}\cdot\nabla)\mathbf{u}}_{\text{Inertia}}=-\underbrace{\nabla\wp}_{\text{Total pressure}}+\underbrace{\nabla\cdot\underline{\underline{\tau_v}}}_{\text{Viscous forces}}-\underbrace{\frac{B_0H}{r}\mathbf{e_r}}_{\text{Lorentz Force}} \tag{4.12}$$

and the Magnetic induction H is calculated by Eq. 3.22 derived in the previous Chapter

$$\nabla^2H-\frac{H}{r^2}=-\sigma B_0\frac{v}{r} \tag{4.13}$$

along with continuity equation:

$$\frac{v}{r}+\frac{\partial v}{\partial r}+\frac{\partial u}{\partial z}=0 \tag{4.14}$$

Note that by adding the constant pressure $-p_r$ to the solution of the of the above set of equations (Eq. 4.11 - 4.13) the solution to the problem does not change due to the fact that the effect of pressure is expressed via its gradient [16], the first term of the right scale of Eq. 4.11. The Poisson-type equation 4.12, namely the Induction Equation, carries out the coupling between the applied magnetic field $\mathbf{B}_0$ and the fluid velocity **u**.

Finally, the last three equations, i.e. Momentum and Induction equations, along with continuity provide the mathematical frame in order to describe the problem in the bulk region of the fluid. The above set of equations is to be solved with imposition of appropriate boundary conditions, which are going to be discussed below.

4.3 Incorporation of Boundary Conditions

The set of equations presented in the previous subsection describes the laminar flow of an incompressible liquid metal inside a vertical capillary tube of cylindrical cross section. Thus, cylindrical coordinates need to be incorporated in which axial symmetry around z-axis is imposed ($\partial / \partial\theta = 0$), implying that the flow arrangement is unchanged if rotated around the z-axis. Boundary conditions for the stream function H=H(r, z) were discussed in Chapter 3.2. As a result, symmetry boundary conditions prevail at $r = 0$:

r = 0:

$$\frac{\partial u}{\partial r}(r=0,z)=0 \tag{4.15}$$

$$v(r=0,z)=0 \tag{4.16}$$

$$H(r=0,z)=0 \tag{4.17}$$

At the pore entrance, the flow is assumed to be fully developed and the transverse velocity is set to zero:

$$\frac{\partial u}{\partial z}(r,z=0)=0 \tag{4.18}$$

$$v(r,z=0)=0 \tag{4.19}$$

$$H(r,z=0)=\frac{rJ}{2} \tag{4.20}$$

Also, the pressure in the reservoir is equal to $p = p_r$. The radial component of current density is set to zero whereas its axial – z component is assumed to be constant with value $J_r = J$. Therefore, we have

$$p(r,z=0)=p_r \Rightarrow \wp(r,z=0)=(p_r-p_r)+\rho g\cdot 0+B_0 H(r,z=0)\Rightarrow$$

$$\wp(r,z=0)=B_0\frac{rJ}{2} \tag{4.21}$$

As far as the right boundary of the related geometry is concerned, the no penetration condition is imposed and a slip length, l, is allowed near the meniscus tip in order to accomodate the liquid metal rise velocity [1]. Hence, at r = R_p and $z\in\left[0,\, f(r)\right]$ we have:

<u>$r = Rp$</u> :

$$v(r=R_p,z)=0 \tag{4.22}$$

$$u(r=R_p,z)=\frac{\partial f}{\partial t}(r=R_p;t)e^{-\left(\frac{1-x}{\varepsilon}\right)},\ x=\frac{z}{f(r)},\ \varepsilon=\frac{l}{R_p} \tag{4.23}$$

$$H(r=R_p,z)=\frac{R_p J}{2} \tag{4.24}$$

The aforementioned condition for u at the pore wall ensures that the no-slip condition is reinstated after a very small slip length l [1]. As far as the liquid-gas interface is concerned, the following two boundary conditions apply. The first condition is the Stress Balance at the interface which reads in vector form as:

$$\left(\underline{\underline{T}}^{(1)}-\underline{\underline{T}}^{(2)}\right)\cdot\mathbf{n}=\gamma(\nabla_s\cdot\mathbf{n})\mathbf{n}\Rightarrow\begin{cases}(p-p_{out})\cdot\mathbf{n}-\underline{\underline{\tau}}_v\cdot\mathbf{n}=\gamma(\nabla_s\cdot\mathbf{n})\mathbf{n}\\ \text{and}\\ \mathbf{t}\cdot\underline{\underline{T}}\cdot\mathbf{n}=0\end{cases} \tag{4.25}$$

where **n** is the unit vector normal to the interface and $\nabla_s=\left(\underline{\underline{I}}-\mathbf{nn}\right)\cdot\nabla$ is the tangential gradient operator. The stresses just outside the liquid-gas interface are assumed to be isotropic since there is no fluid motion above the interface, thus $\underline{\underline{T}}^{(1)}=-p_{out}\underline{\underline{I}}$. The following Figure, **Fig. 4.2**, represents a more detailed look at the free surface between two immiscible fluids and its curvature.

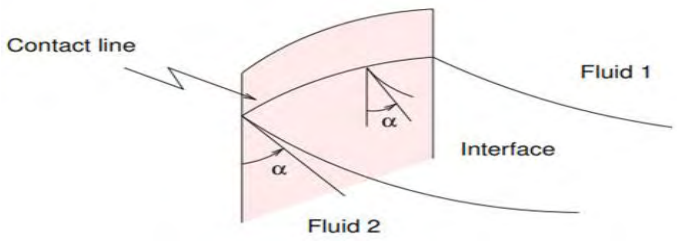

Fig. 4.2 A three-dimensional illustration of an interface terminating at a curved contact line, adopted from [23]. By convention, Fluid 2 corresponds to the fluid of higher density, liquid lithium in this case. Note that vector **n** always points towards the outer fluid (vacuum in this problem).

The free surface is assumed to have a shape which depends on the radial spatial coordinate, *r*, thus the interface shape is presented by an unknown function f(r). The surface tension is spatially independent since there are no interfacial temperature gradients and as a result no thermocapillary effect. Recalling the relation for the total pressure, Eq. 4.11, we have for the interface:

$$\boxed{\begin{array}{l}\left(\wp - \rho g z - B_0 H - p_{out}\right)\cdot\mathbf{n} - \underline{\underline{\tau}}_v \cdot \mathbf{n} = \gamma\left(\nabla_s \cdot \mathbf{n}\right)\mathbf{n} \\ \text{where z = f}\left(r\right) \text{ at the interface}\end{array}} \tag{4.26}$$

The latter expression is also known as the dynamic condition and is used in free surface flows as a tool to determine the position of a moving boundary as part of the solution since it is known only at t = 0. The dynamic condition has two physical interpretations. The first expression occurs from the tangential (to the interface) component the dynamic condition:

$$\mathbf{t}\cdot\underline{\underline{T}}\cdot\mathbf{n} = 0 \tag{4.27}$$

implies that there is no shear stress tangential to the interface. The second, states that the stress within the liquid, normal to and just inside the interface, must be balanced by a stress acting normal to the surface arising from surface tension [16], and described by the augmented Young-Laplace equation (Eq. 4.26).

The second condition imposed at the interface is the kinematic condition asserting that the fluid does not cross the free surface. If **n** is the outward pointing unit normal to the interface and $\mathbf{u}_s = \left(\partial f / \partial t\right)\mathbf{e}_\mathbf{z}$ corresponds to the surface velocity, the kinematic boundary condition is given by the following relation:

$$\mathbf{n}\cdot\left(\mathbf{u}-\mathbf{u}_s\right) = 0 \Rightarrow$$

$$\left(\frac{\mathbf{e}_\mathbf{z} - f_r\mathbf{e}_\mathbf{r}}{\sqrt{1-f_r{}^2}}\right)\cdot\left(u\mathbf{e}_\mathbf{z} + v\mathbf{e}_\mathbf{r} - \frac{\partial f}{\partial t}\mathbf{e}_\mathbf{z}\right) = 0 \Rightarrow$$

$$\boxed{\frac{\partial f}{\partial t} + \frac{\partial f}{\partial r}v = u} \tag{4.28}$$

where $f_r \equiv \dfrac{\partial f}{\partial r}$.

4.4 Non dimensionlization of the governing equations

Thus far, the governing equations of the problem describing the liquid lithium flow within the pore under the influence of an external magnetic field, the so-called jxB effects, are the following:

Momentum

$$\rho\frac{\partial \mathbf{u}}{\partial t}+\rho(\mathbf{u}\cdot\nabla)\mathbf{u}=-\nabla\wp+\nabla\cdot\underline{\underline{\tau}}_{v}-\frac{B_0 H}{r}\mathbf{e_r} \tag{4.29}$$

Magnetic Induction

$$\nabla^2 H-\frac{H}{r^2}=-\sigma B_0\frac{v}{r} \tag{4.30}$$

Continuity

$$\frac{v}{r}+\frac{\partial v}{\partial r}+\frac{\partial u}{\partial z}=0 \tag{4.31}$$

Kinematic Condition at the Interface

$$\frac{\partial f}{\partial t}+\frac{\partial f}{\partial r}v=u \tag{4.32}$$

Stress Balance at the Interface

$$(\wp-\rho g z-B_0 H-P_{out})\cdot\mathbf{n}-\underline{\underline{\tau}}_{v}\cdot\mathbf{n}=\gamma(\nabla_s\cdot\mathbf{n})\mathbf{n} \tag{4.33}$$

where $\mathbf{n}=(\mathbf{e_z}-f_r\mathbf{e_r})\left(1+f_r^{\,2}\right)^{-0.5}$ is the unit vector normal to the free surface. Furthermore, at the interface the following condition for the electric currents is incorporated:

$$f_r J_z+J_r=\frac{f_r}{r}H-\frac{\partial H}{\partial n}\sqrt{1+f_r^{\,2}} \tag{4.34}$$

in which J_z, J_r are known quantities and represent the two components of current density at z = f(r).

The Boundary Conditions are:

$$\underline{r=0}:\ H=0,\ v=0,\ \frac{\partial u}{\partial r}=0 \tag{4.35}$$

$$\underline{r=R_p}:\ H=\frac{R_p J}{2},\ v=0,\ u=\left.\frac{\partial f}{\partial t}\right|_{(r=R_p,t)}e^{-\left(\frac{1-x}{\varepsilon}\right)},\ x=\frac{z}{f(r)},\ \varepsilon=\frac{l}{R_p} \tag{4.36}$$

$$\underline{z=0}:H=\frac{rJ}{2},\ p=p_r\Rightarrow p_l=p_r-p_r=0 \tag{4.37}$$

where

$$J = \frac{2}{R_p^2}\int_0^{R_p}\left(J_z - f_r J_z\right) r dr$$

and the Initial Conditions:

$$H\left(r,z,t=0\right) = p\left(r,z,t=0\right) = 0 \tag{4.38}$$

$$\left(u,v\right)\big|_{t=0} = 0 \tag{4.39}$$

$$f\left(r,t=0\right) = R_p \tag{4.40}$$

In order to render the governing equations and boundary conditions dimensionless, the physical and spatial parameters of the problem are deployed. Specifically, the pore radius R_p was chosen as the characteristic length, γ/R_p as the characteristic pressure and $\hat{u}$ as a characteristic velocity. The latter is derived via a force balance between surface tension and inertia and accordingly:

$$\left|\rho\mathbf{u}\cdot\nabla\mathbf{u}\right| = \left|\nabla p\right| \Rightarrow \rho\hat{u}\frac{\hat{u}}{R_p} = \frac{\gamma}{R_p^{\,2}} \Rightarrow$$

$$\boxed{\hat{u} = \sqrt{\frac{\gamma}{\rho R_p}}} \tag{4.41}$$

The dimensionless variables (denoted by *) are defined as

$$\left(r,z\right)^* = \frac{\left(r,z\right)}{R_p},\ \left(u,v\right)^* = \frac{\left(u,v\right)}{\hat{u}},\ H^* = \frac{H}{R_p J_r}$$

$$\wp^* = \frac{\wp}{\gamma/R_p},\ J^* = \frac{J}{J_r},\ t^* = \frac{t}{\left(R_p/\hat{u}\right)} = \frac{t}{\sqrt{\rho R_p^{\,3}/\gamma}} \tag{4.42}$$

In dimensionless form, the set of the governing equations is written as

<u>Momentum</u>

$$\rho\left(\frac{\partial\left(\hat{u}\mathbf{u}^*\right)}{\partial\left(Rp/\hat{u}t^*\right)} + \left(\hat{u}\mathbf{u}^*\right)\cdot\frac{1}{R_p}\nabla^*\right)\left(\hat{u}\mathbf{u}^*\right) = -\left(\frac{1}{R_p}\nabla^*\right)\left(\frac{\gamma}{R_p}\wp^*\right) + \left(\frac{1}{R_p}\nabla^*\right)\cdot\left(\frac{\mu\hat{u}}{R_p}\underline{\underline{\tau}}_v^{\,*}\right) - B_0\frac{R_p J_r H^*}{R_p r^*}\mathbf{e}_r \Rightarrow$$

$$\left(\rho\frac{\hat{u}^2}{R_p}\right)\left(\frac{\partial\mathbf{u}^*}{\partial t^*} + \left(\mathbf{u}^*\cdot\nabla^*\right)\mathbf{u}^*\right) = -\frac{\gamma}{R_p^{\,2}}\nabla^*\wp^* + \frac{\mu\hat{u}}{R_p^{\,2}}\nabla^*\cdot\underline{\underline{\tau}}_v^{\,*} - B_0\frac{J_r H^*}{r^*}\mathbf{e}_r \Rightarrow$$

$$We\left(\frac{\partial\mathbf{u}^*}{\partial t^*} + \left(\mathbf{u}^*\cdot\nabla^*\right)\mathbf{u}^*\right) = -\nabla^*\wp^* + Ca\nabla^*\cdot\underline{\underline{\tau}}_v^{\,*} - Bo_m\frac{H^*}{r^*}\mathbf{e}_r$$

Hereafter, the asterisk (*) above dimensionless variables is dropped for convenience and hence the dimensionless momentum equation is obtained.

$$\boxed{We\left(\frac{\partial \mathbf{u}}{\partial t}+\mathbf{u}\cdot\nabla\mathbf{u}\right)=-\nabla\wp+Ca\nabla\cdot\underline{\underline{\tau}}_{v}-Bo_{m}\frac{H}{r}\mathbf{e}_{\mathbf{r}}} \tag{4.43}$$

where is $\wp = p_l + Boz + Bo_m H$ the dimensionless fluid pressure.

The non dimensionalization of the rest of the equations is carried out in a similar fashion.

Magnetic Induction

$$\frac{1}{R_p{}^2}\nabla^{*2}(H^* J_r R_p)-\frac{H^* J_r R_p}{(R_p r^*)^2}=-B_0\sigma\frac{\hat{u}v^*}{R_p r^*}\Rightarrow$$

$$\frac{J_r}{R_p}\nabla^2 H-\frac{J_r H}{R_p r^2}=-B_0\sigma\frac{\hat{u}v}{R_p r}\Rightarrow$$

$$\nabla^2 H-\frac{H}{r^2}=-\underbrace{\left(\frac{\sigma B_0}{J_r}\hat{u}\right)}_{=c}\frac{v}{r}=-c\frac{v}{r}\Rightarrow$$

$$\boxed{\nabla^2 H-\frac{H}{r^2}=-c\frac{v}{r}} \tag{4.44}$$

where c is a non-dimensional number defined as

$$c=\frac{\sigma B_0\hat{u}}{J_r} \tag{4.45}$$

and is the ratio of the induced over the injected electrical current

Continuity

$$\left(\frac{1}{R_p}\nabla^*\right)\cdot\left(\hat{u}\mathbf{u}^*\right)=0\Rightarrow$$

$$\nabla^*\cdot\mathbf{u}^*=0\Rightarrow$$

$$\boxed{\frac{v}{r}+\frac{\partial v}{\partial r}+\frac{\partial u}{\partial z}=0} \tag{4.46}$$

Stress Balance at the Interface

$$\left[\frac{\gamma}{R_p}\wp^* - \rho g(R_p z^*) - B_0(R_p J_r H^*) - \frac{\gamma}{R_p}p_{out}{}^*\right]\mathbf{n} - (\frac{\mu\hat{u}}{R_p})\underline{\underline{\tau}}_v{}^*\cdot\mathbf{n} = \gamma\left[\left(\frac{1}{R_p}\nabla^*_s\cdot\mathbf{n}\right)\mathbf{n}\right] = -\frac{\gamma}{R_p}\left(\frac{\partial\mathbf{t}}{\partial s} - \frac{\mathbf{n}}{R_2}\right)^*$$

Both legs of the above relation are multiplied by R_p/γ to give the dimensionless form of stress balance equation:

$$\boxed{\left(\wp - Boz - Bo_m H - p_{out}\right)\cdot\mathbf{n} - Ca\underline{\underline{\tau}}_v\cdot\mathbf{n} = \left(\nabla_s\cdot\mathbf{n}\right)\mathbf{n}} \qquad (4.47)$$

where $\mathbf{t} = \frac{\mathbf{e_z} + f_r\mathbf{e_r}}{\sqrt{1+f_r^2}}$ and $\mathbf{n} = \frac{\mathbf{e_z} - f_r\mathbf{e_r}}{\sqrt{1+f_r^2}}$ are normal and tangent unit vectors, respectively.

Kinematic Condition at the Interface

$$\frac{\partial\left(R_p f^*\right)}{\partial\left(R_p/\hat{u}t^*\right)} + \frac{\partial(R_p f^*)}{\partial(R_p r^*)}\left(\hat{u}v^*\right) = \left(\hat{u}u^*\right) \Rightarrow$$

$$\boxed{\frac{\partial f}{\partial t} + v\frac{\partial f}{\partial r} = u} \qquad (4.48)$$

In the system of equations above, the dimensionless parameters are the Capillary number, $Ca = \mu\hat{u}/\gamma$, Weber number, $We = \rho\hat{u}^2 R_p/\gamma$, gravitational Bond number, $Bo = \rho g R_p{}^2/\gamma$ and magnetic Bond number, $Bo_m = B_0 J_r R_p{}^2/\gamma$. As far as their meaning is concerned, the first number measures the importance of viscous forces relative to surface tension forces, the Weber number the importance of inertial forces relative to surface tension forces, the gravitational Bond number the importance of gravitational effects relative to surface tension related effects. To this end, it is of interest to state that the aforementioned dimensionless numbers are used in problems in which a fluid is bounded by a free surface or fluid interface [23]. Furthermore, the magnetic Bond number, defined in [1], measures the magnitude of magnetic pressure forces relative to surface tension forces:

$$Bo_m = \frac{\text{Magnetic pressure}}{\text{Capillary pressure}} = \frac{B_0 J_r R_p}{\gamma/R_p}$$

At this point, it is worth noting that not all of the above parameters are going to impose a significant effect in the numerical results presented later in Chapter 6. This is mainly due to the fact that the characteristic length of the geometry under investigation, the pore radius, is of magnitude of O(10) μm [18] and the physical properties of liquid lithium. For instance, the gravitational Bond number of the flow is less than 10^{-3}, meaning that any gravitational effects can safely be neglected [29].

To this end the system is closed by the rendering the Boundary Conditions dimensionless. Accordingly, the Boundary Conditions are as follows:

$$\underline{r=0}:\ H=0,\ v=0,\ \frac{\partial u}{\partial r}=0 \tag{4.49}$$

$$\underline{r=1}:\ H=\frac{J}{2},\ v=0,\ u=\left.\frac{\partial f}{\partial t}\right|_{(r=1,t)}\exp\left[-\left(\frac{1-x}{l}\right)\right] \tag{4.50}$$

$$\underline{z=0\ \left(reservoir\right)}:\ H=\frac{rJ}{2},\ p=p_r \Rightarrow p_l=p_r-p_r=0\Rightarrow$$

$$\wp\left(r,x=0\right)=Bo_m\frac{rJ}{2} \tag{4.51}$$

$$\underline{z=f\left(r\right)}:\ f_r J_z+1=\frac{f_r}{r}H-\frac{\partial H}{\partial n}\sqrt{1+f_r^{\,2}} \tag{4.52}$$

where

$$J=2\int_0^1\left(J_z-f_r\right)rdr \tag{4.53}$$

is the dimensionless current density at the pore entrance. The last expression is calculated only at the interface.

We now have the dimensionless form of the governing differential equations along with the boundary and initial conditions that are needed to describe the replenishment process. In the next Chapter, a numerical method, specifically the Finite Element Method, is deployed to solve the system for all the six unknown variables.

Chapter 5: Numerical Analysis

In the fifth chapter, a brief description of the numerical methodology that was deployed in order to solve the mathematical system described in Chapter 4 is given. Particularly, the Galerkin Finite Element Method is utilized for the discretization of the nonlinear governing equations, leading to a nonlinear algebraic system. The resulting system is solved at every time instant via the Newton-Raphson iterative procedure until convergence is achieved. Finally, benchmark calculations are conducted in order to validate the numerical model.

5.1 The Finite element method methodology

The Finite Element Method is a numerical method in which a given space is represented as a collection of simple domains, known as finite elements, so that it is possible to systematically construct the approximation functions needed in a variational or weighted-residual approximation of the solution of a problem over each element. For a typical problem, according to Reddy [28], the basic steps involved in the finite element analysis of a problem are the following:

1. Discretization of the given domain into a collection of preselected finite elements.
   a. Construct the finite element mesh of preselected elements.
   b. Number the nodes and elements.
   c. Generate the geometric properties (e.g., coordinates and cross-sectional areas) needed for the problem.

2. Derivation of element equations for all typical elements in the mesh.
   a. Construct the variational formulation of the given differential equation over the typical element.
   b. Assume that a typical dependent variable u is of the form $u = \sum_{i=1}^{n} u_i b_i$ and substitute it into Step 2a to obtain element equations in the form $\left[K^e \right]\{\mathrm{u}^e\} = \{\mathrm{F}^e\}$
   c. Derive or select element interpolation functions b_i and compute the element matrices.

3. Assembly of element equations to obtain the equations of the whole problem.
   a. Identify the interelement continuity conditions among the primary variables by relating element nodes to global nodes. Construct the variational formulation of the given differential equation over the typical element.
   b. Identify the "equilibrium" conditions among the secondary variables.
   c. Assemble element equations using Steps 3a and 3b.

4. Imposition of the boundary conditions of the problem

a. Identify the specified global primary degrees of freedom.
b. Identify the specified global secondary degrees of freedom.

5. Solution of the assembled equations.

6. Post-processing of the results.

5.2 Weak Form of the Momentum equations

As mentioned previously in Chapter 2, in order to mathematically model the flow of the liquid metal inside a single pore under the presence of a known static magnetic field, the geometry under consideration has the form of a vertical cylindrical tube of radius R_p. As a result, the upper boundary of the liquid metal column will be a free surface which is described by the function f(r). The position and the shape of the free boundary continuously changes as the liquid trapped within the pore rises due to capillary forces and is regarded as a crucial unknown of the mathematical problem under investigation. For this reason and in order to ensure that the mesh size of the computational domain along the z direction lies between 0 and 1, variable x = z / f(r) is introduced. Subsequently, the process for calculating the interface shape is established using the Spine Method for mesh generation [4, 5]. Although it has been proven that the Elliptic mesh generation method is more effective than the Spine Method and is preferred over the latter [5], the Spine Method is suitable for this problem since we are interested in predicting the liquid rise velocity and the induced interfacial deformations are not large.

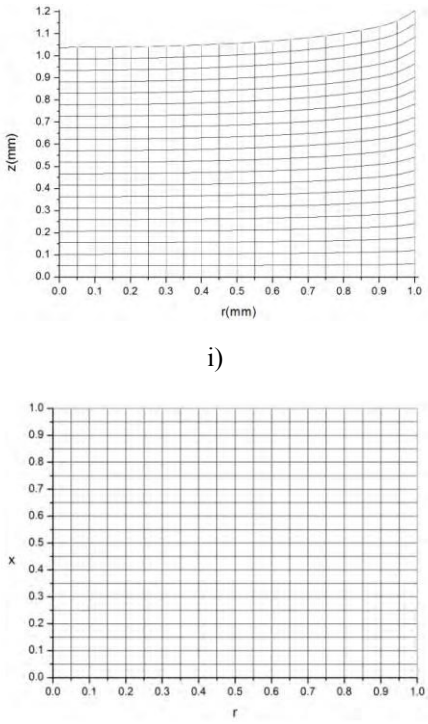

i)

ii)

Fig. 5. 1 i) The Physical mesh and ii) the Computational mesh, at the same time instant based on the Spine Method.

The velocity components u, v along with the magnetic induction H, fluid pressure, p, and shape interface f are discretized in space using the finite element method. For the first three unknown variables, biquadratic elements are deployed, bilinear for the pressure and one-dimensional quadratic elements for the shape interface. Thus, we have that

$$(u,v,H)=\sum_{i=1}^{M}(u_i,v_i,H_i)\,B_i(r,z),\quad p=\sum_{i=1}^{N}p_i\Psi_i(r,z),\quad f(r)=\sum_{i=1}^{K}f_i b_i(r)$$

Here, M is the number of biquadratic finite element basis functions used, N the number of bilinear basis functions and K the number of 1-D quadratic basis function used for the approximation of the shape interface.

The Galerkin weighted residuals of the governing equations are the following:

Momentum

$$R_{ki}=\iiint_{Ve}B_i\mathbf{e_k}\cdot\left[-We\left(\frac{\partial\mathbf{u}}{\partial t}+\mathbf{u}\cdot\nabla\mathbf{u}\right)-\nabla\wp+Ca\nabla\cdot\underline{\underline{\tau}}_v-Bo_m\frac{H}{r}\mathbf{e_r}\right]dV=0\Rightarrow$$

$$R_{ki}=-\iiint_{Ve}WeB_i\mathbf{e_k}\cdot\left(\frac{\partial\mathbf{u}}{\partial t}+\mathbf{u}\cdot\nabla\mathbf{u}\right)dV-\iiint_{Ve}\left[\nabla\wp\cdot\left(B_i\mathbf{e_k}\right)\right]dV-\iiint_{Ve}Ca(\nabla\cdot\underline{\underline{\tau}}_v)\cdot\left(B_i\mathbf{e_k}\right)dV$$

$$-\iiint_{Ve}B_i\mathbf{e_k}\cdot\left(Bo_m\frac{H}{r}\mathbf{e_r}\right)dV=0 \qquad (5.1)$$

with k = 1, 2 standing for the z, r components of the fluid velocity, respectively, and thus $\mathbf{e_k}=\{\mathbf{e_z},\mathbf{e_r}\}$.

$$R_{ki}=-\iiint_{Ve}WeB_i\mathbf{e_k}\cdot\left(\frac{\partial\mathbf{u}}{\partial t}+\mathbf{u}\cdot\nabla\mathbf{u}\right)dV-\iiint_{Ve}\nabla\cdot\left(B_i\wp\mathbf{e_k}\right)dV+\iiint_{Ve}\wp\nabla\cdot\left(B_i\mathbf{e_k}\right)dV$$

$$+\iiint_{Ve}Ca(\nabla\cdot\underline{\underline{\tau}}_v)\cdot\left(B_i\mathbf{e_k}\right)dV-\iiint_{Ve}B_iBo_m\frac{H}{r}\underbrace{\mathbf{e_r}\cdot\mathbf{e_k}}_{=\delta_{rk}}dV=0 \qquad (5.2)$$

Here δ_{rk} is the Kronecker delta: $\delta_{rk}=1$ if k = r and $\delta_{rk}=0$ if k = z. Besides, the second integral in the above expression can be expanded using the Divergence Theorem. The unit vectors of the associated geometry are constant and independent of the spatial coordinate θ since axisymmetry is assumed and hence they can be brought out of the integrals:

$$R_{ki}=-\iiint_{Ve}WeB_i\mathbf{e_k}\cdot\left(\frac{\partial\mathbf{u}}{\partial t}+\mathbf{u}\cdot\nabla\mathbf{u}\right)dV-\oiint_{Ae}(\wp B_i\mathbf{e_k})\cdot\mathbf{n}dA+\iiint_{Ve}\wp\nabla\cdot\left(B_i\mathbf{e_k}\right)dV$$

$$-\iiint_{Ve}Ca\underline{\underline{\tau}}_v:\nabla\left(B_i\mathbf{e_k}\right)dV+\oiint_{Ae}Ca\underbrace{\left[\underline{\underline{\tau}}_v\cdot\left(B_i\mathbf{e_k}\right)\right]}_{=(\underline{\underline{\tau}}_v\cdot\mathbf{n})\cdot(B_i\mathbf{e_k})}\cdot\mathbf{n}\,dA-\iiint_{Ve}B_iBo_m\frac{H}{r}\delta_{rk}dV=0$$

Moreover, 2π can be eliminated from every term, simplifying the above expression

$$\Rightarrow R_{ki} = -\iint_{Ae} WeB_i \mathbf{e_k} \cdot \left(\frac{\partial \mathbf{u}}{\partial t} + \mathbf{u} \cdot \nabla \mathbf{u} \right) dA - \left(\oint_{\Gamma e} \wp B_i \mathbf{n} r ds \right) \cdot \mathbf{e_k} + \iint_{Ae} \wp \nabla \cdot (B_i \mathbf{e_k}) dA$$

$$-\iint_{Ae} \mathrm{Ca}\, \underline{\underline{\tau}}_v : \nabla (B_i \mathbf{e_k}) dA + \oint_{\Gamma e} \left[Ca(\underline{\underline{\tau}}_v \cdot \mathbf{n}) \right] \cdot (B_i \mathbf{e_k}) r ds - \iint_{Ae} B_i Bo_m \frac{H}{r} \delta_{rk} dA = 0 \tag{5.3}$$

where **n** denotes the outward pointing unit normal to the boundary and the symmetry of the viscous stress tensor was taken into account. Hereafter, the two boundary integral terms are written together in order to incorporate the stress balance at the liquid-gas interface using Eq. 4.44. At this point it is useful to state that the two expressions for $\underline{\underline{\tau}}_v$: $\nabla(B_i \mathbf{e_k})$ are included in Appendix B.

$$R_{ki} = -\iint_{Ae} WeB_i \mathbf{e_k} \cdot \left(\frac{\partial \mathbf{u}}{\partial t} + \mathbf{u} \cdot \nabla \mathbf{u} \right) dA + \iint_{Ae} \wp \nabla \cdot (B_i \mathbf{e_k}) dA - \iint_{Ae} \mathrm{Ca}\, \underline{\underline{\tau}}_v : \nabla (B_i \mathbf{e_k}) dA$$

$$-\oint_{\Gamma e} \left[\wp \mathbf{n} - Ca(\underline{\underline{\tau}}_v \cdot \mathbf{n}) \right] \cdot (B_i \mathbf{e_k}) r ds - \iint_{Ae} B_i Bo_m \frac{H}{r} \delta_{rk} dA \overset{\text{Eq. 4.44}}{\Rightarrow}$$

$$R_{ki} = -\iint_{Ae} WeB_i \mathbf{e_k} \cdot \left(\frac{\partial \mathbf{u}}{\partial t} + \mathbf{u} \cdot \nabla \mathbf{u} \right) dA + \iint_{Ae} \wp \nabla \cdot (B_i \mathbf{e_k}) dA - \iint_{Ae} \mathrm{Ca}\, \underline{\underline{\tau}}_v : \nabla (B_i \mathbf{e_k}) dA$$

$$-\oint_{\Gamma e} \left[(Boxf + Bo_m H + p_{out}) \mathbf{n} + (\nabla_s \cdot \mathbf{n}) \mathbf{n} \right] \cdot (B_i \mathbf{e_k}) r ds - \iint_{Ae} B_i Bo_m \frac{H}{r} \delta_{rk} dA \tag{5.4}$$

The second term inside the boundary integral term can be written as a function of the tangent and normal unit vectors **n**, **t** and the principal Radii of curvature, that is

$$(\nabla_s \cdot \mathbf{n}) \mathbf{n} = \left(\frac{\partial \mathbf{t}}{\partial s} - \frac{\mathbf{n}}{R_2} \right) \tag{5.5}$$

The aforementioned quantities are connected to the shape interface f and their analytical expressions are included in Appendix A. However, according to the full form of Eq. 5.5 included in the Appendix A, therein appear second order derivatives of the interface shape f(r) with respect to the radial distance r. Consequently, a suitable manipulation of the latter equation should be made in order to reduce the order of differentiation. Specifically, integration by parts is used on the above term inside the line integral. Thus we have:

$$\int_{\Gamma e} (\nabla_s \cdot \mathbf{n}) \mathbf{n} \cdot (B_i \mathbf{e_k}) r ds = \int_{\Gamma e} \left(\frac{\partial \mathbf{t}}{\partial s} - \frac{\mathbf{n}}{R_2} \right) \cdot (B_i \mathbf{e_k}) r ds = \int_{\Gamma e} \frac{\partial \mathbf{t}}{\partial s} \cdot (B_i \mathbf{e_k}) r ds - \int_{\Gamma e} \frac{\mathbf{n}}{R_2} \cdot (B_i \mathbf{e_k}) r ds \Rightarrow$$

$$\int_{\Gamma e} (\nabla_s \cdot \mathbf{n}) \mathbf{n} \cdot (B_i \mathbf{e_k}) r ds = \int_{r=0}^{r=1} d (r B_i \mathbf{e_k} \cdot \mathbf{t}) - \int_{\Gamma e} \frac{\partial (r B_i \mathbf{e_k})}{\partial s} \cdot \mathbf{t} ds - \int_{\Gamma e} \frac{\mathbf{n}}{R_2} \cdot (B_i \mathbf{e_k}) r ds \Rightarrow$$

$$\int_{\Gamma e}(\nabla_s\cdot\mathbf{n})\mathbf{n}\cdot\left(B_i\mathbf{e}_\mathbf{k}\right)rds=\left(rB_i\mathbf{e}_\mathbf{k}\cdot\mathbf{t}\right)|_{r=0}^{r=1}-\int_{\Gamma e}\frac{\partial\left(rB_i\mathbf{e}_\mathbf{k}\right)}{\partial r\sqrt{1+f_r{}^2}}\cdot\mathbf{t}\sqrt{1+f_r{}^2}dr-\int_{\Gamma e}\frac{\mathbf{n}}{R_2}\cdot\left(B_i\mathbf{e}_\mathbf{k}\right)rds \quad \overset{ds=\sqrt{1+f_r{}^2}dr}{\Rightarrow}$$

$$\int_{\Gamma e}(\nabla_s\cdot\mathbf{n})\mathbf{n}\cdot\left(B_i\mathbf{e}_\mathbf{k}\right)rds=\left(rB_i\mathbf{e}_\mathbf{k}\cdot\mathbf{t}\right)|_{r=1}-\int_{\Gamma e}\frac{\partial(rB_i)}{\partial r}\mathbf{e}_\mathbf{k}\cdot\mathbf{t}dr-\int_{\Gamma e}\frac{f_r}{r\sqrt{1+f_r{}^2}}\mathbf{n}\cdot\left(B_i\mathbf{e}_\mathbf{k}\right)r\sqrt{1+f_r{}^2}dr\Rightarrow$$

$$\int_{\Gamma e}(\nabla_s\cdot\mathbf{n})\mathbf{n}\cdot\left(B_i\mathbf{e}_\mathbf{k}\right)rds=\left(rB_i\mathbf{e}_\mathbf{k}\cdot\mathbf{t}\right)|_{r=1}-\int_{\Gamma e}\left(r\frac{\partial B_i}{\partial r}+B_i\right)\mathbf{e}_\mathbf{k}\cdot\mathbf{t}dr-\int_{\Gamma e}f_r\mathbf{n}\cdot\left(B_i\mathbf{e}_\mathbf{k}\right)dr \tag{5.6}$$

The first term on the RHS of the above express reads $\sin\theta_c\big|_{r=1}$ for k = z and $\cos\theta_c\big|_{r=1}$ for k = r, where $\theta_c=\pi/2-\theta$ is the complimentary angle of the contact angle. Finally, the residuals corresponding to the conservation of linear momentum are the following:

<u>z momentum: for k = z</u>

$$R_{1i}=\iint_{Ae}\left[\wp\frac{\partial B_i}{\partial z}-2Ca\frac{\partial u}{\partial z}\frac{\partial B_i}{\partial z}-Ca\frac{\partial B_i}{\partial r}\left(\frac{\partial u}{\partial r}+\frac{\partial v}{\partial z}\right)-We\left(u\frac{\partial u}{\partial z}+v\frac{\partial u}{\partial r}\right)B_i\right]rdrdz$$
$$-\int_{\Gamma e}B_i\,n_z\left[p_{out}+BOf+Bo_mH+\nabla_s\cdot\mathbf{n}\right]r\sqrt{1+f_r{}^2}dr-\int_{\Gamma e}B_i\,\wp\left(z=0\right)rdr$$
$$-\iint_{Ae}We\left(\frac{u^{n+1}-u^n}{\Delta t}\right)B_irdrdz\Rightarrow$$

$$\boxed{\begin{aligned}&R_{1i}=\iint_{Ae}\left[\wp\frac{\partial B_i}{\partial z}-2Ca\frac{\partial u}{\partial z}\frac{\partial B_i}{\partial z}-Ca\frac{\partial B_i}{\partial r}\left(\frac{\partial u}{\partial r}+\frac{\partial v}{\partial z}\right)-We\left(u\frac{\partial u}{\partial z}+v\frac{\partial u}{\partial r}\right)B_i\right]rdrdz\\&-\int_{\Gamma e}B_i\left[p_{out}+Bof+Bo_mH+(\nabla_s\cdot\mathbf{n})\right]rdr\\&-\int_{\Gamma e}B_i\frac{Bo_mrJ}{2}rdr-\iint_{Ae}We\left(\frac{u^{n+1}-u^n}{\Delta t}\right)B_irdrdz\end{aligned}} \tag{5.7}$$

<u>r momentum: for k = r</u>

$$R_{2i}=\iint_{Ae}\left[\wp\frac{1}{r}\frac{\partial(rB_i)}{\partial r}-2Ca\frac{\partial v}{\partial r}\frac{\partial B_i}{\partial r}-Ca\frac{\partial B_i}{\partial z}\left(\frac{\partial u}{\partial r}+\frac{\partial v}{\partial z}\right)-2Ca\frac{vB_i}{r^2}-We\left(u\frac{\partial v}{\partial z}+v\frac{\partial v}{\partial r}\right)B_i\right]rdrdz$$
$$-\int_{\Gamma e}B_i\,n_r\left[p_{out}+Bof+Bo_mH+\nabla_s\cdot\mathbf{n}\right]r\sqrt{1+f_r{}^2}dr-\iint_{Ae}We\left(\frac{v^{n+1}-v^n}{\Delta t}\right)B_irdrdz-\iint_{Ae}B_iBo_m\frac{H}{r}rdrdz\Rightarrow$$

$$\boxed{\begin{aligned}&R_{2i}=\iint_{Ae}\left[\wp\frac{1}{r}\frac{\partial(rB_i)}{\partial r}-2Ca\frac{\partial v}{\partial r}\frac{\partial B_i}{\partial r}-Ca\frac{\partial B_i}{\partial z}\left(\frac{\partial u}{\partial r}+\frac{\partial v}{\partial z}\right)-2Ca\frac{vB_i}{r^2}-We\left(u\frac{\partial v}{\partial z}+v\frac{\partial v}{\partial r}\right)B_i\right]rdrdz\\&-\iint_{Ae}We\left(\frac{v^{n+1}-v^n}{\Delta t}\right)B_irdrdz-\iint_{Ae}B_iBo_m\frac{H}{r}rdrdz+\int_{\Gamma e}B_i\left[p_{out}+Bof+Bo_mH+\nabla_s\cdot\mathbf{n}\right]rf_rdr\end{aligned}} \tag{5.8}$$

Note that the time derivatives in the acceleration term of each momentum residual is discretized in time using a fully implicit scheme [1] involving the two velocity values of the previous time instant, denoted by the symbol 'n', and Δt is the dimensionless time step. Moreover, n+1 denotes the current time instant at which every other term is calculated.

5.3 Weak Form of the Induction, Continuity and Kinematic equations

The Magnetic induction residual is obtained after moving the RHS source term in the left scale and integrating over the liquid volume:

$$R_{3i} = \iiint_{Ve} B_i \left(\nabla^2 H - \frac{H}{r^2} + c\frac{v}{r} \right) dV = 0 \tag{5.9}$$

In the above expression, the quantity inside the volume integral does not depend on θ and, thus, 2π can be eliminated converting the volume integral to a surface integral:

$$R_{3i} = \iint_{Ae} B_i \left(\nabla^2 H - \frac{H}{r^2} + c\frac{v}{r} \right) dA \Rightarrow$$

$$R_{3i} = \iint_{Ae} \left(B_i \nabla^2 H - B_i \frac{H}{r^2} + B_i c\frac{v}{r} \right) r dr dz \Rightarrow$$

$$R_{3i} = \iint_{Ae} (B_i \nabla^2 H) r dr dz - \iint_{Ae} B_i \frac{H}{r^2} r dr dz + \iint_{Ae} c\frac{vB_i}{r} r dr dz \tag{5.10}$$

The first term in the last expression is written in a different form using the Divergence Theorem in order to reduce the order of differentiation and to incorporate the Robin-type boundary condition at the liquid-gas interface:

$$R_{3i} = -\iint_{Ae} (\nabla B_i \cdot \nabla H) r dr dz + \oint_{\Gamma e} B_i \frac{\partial H}{\partial n} r ds - \iint_{Ae} B_i \frac{H}{r^2} r dr dz + \iint_{Ae} c\frac{vB_i}{r} r dr dz \Rightarrow$$

$$R_{3i} = \iint_{Ae} (\nabla B_i \cdot \nabla H) r dr dz - \oint_{\Gamma e} B_i \frac{\partial H}{\partial n} r ds + \iint_{Ae} B_i \frac{H}{r^2} r dr dz - \iint_{Ae} c\frac{vB_i}{r} r dr dz \tag{5.11}$$

The line integral term is going to be evaluated only at the interface via the following calculations in which the Robin-type boundary condition Eq. 4.52 is incorporated

$$\int_{\Gamma e} B_i \frac{\partial H}{\partial n} r ds = \int_{\Gamma e} B_i \frac{\partial H}{\partial n} r \sqrt{1 + f_r^{\,2}} dr = \int_{\Gamma e} B_i \left(\frac{\partial H}{\partial n} \sqrt{1 + f_r^{\,2}} \right) r dr \Rightarrow$$

$$\int_{\Gamma e} B_i \frac{\partial H}{\partial n} r ds = \int_{\Gamma e} B_i (-f_r J_z - J_r + f_r \frac{H}{r}) r dr \tag{5.12}$$

Finally, combining the last two expressions leads to the following result for the residual concerning the magnetic part:

$$R_{3i} = \iint_{Ae} (\nabla B_i \cdot \nabla H) r dr dz - \int_{\Gamma e} B_i (-f_r J_z - J_r + f_r \frac{H}{r}) r dr + \iint_{Ae} B_i \frac{H}{r^2} r dr dz - \iint_{Ae} c \frac{\nu B_i}{r} r dr dz \Rightarrow$$

$$\boxed{R_{3i} = \iint_{Ae} (\frac{\partial B_i}{\partial r}\frac{\partial H}{\partial r} + \frac{\partial B_i}{\partial z}\frac{\partial H}{\partial z} + B_i \frac{H}{r^2}) r dr dz - \iint_{Ae} c \frac{\nu B_i}{r} r dr dz + \int_{\Gamma e} B_i (f_r J_z r + r J_r - f_r H) dr} \quad (5.13)$$

where the Γ symbol corresponds to the elements exactly at the interface.

As far as continuity and the kinematic condition are concerned, they are discretized by deploying the bilinear and 1-D quadratic basis functions respectively.

$$R_{4i} = \iint_{Ae} \Psi_i \left(\frac{\nu}{r} + \frac{\partial u}{\partial z} + \frac{\partial \nu}{\partial r} \right) r dr dz \quad (5.14)$$

$$R_{5i} = \int_{\Gamma e} b_i \left(\frac{\partial f}{\partial t} + \nu^{(n+1)} \frac{\partial f}{\partial r}^{(n+1)} - u^{(n+1)} \right) r dr \Rightarrow$$

$$\boxed{R_{5i} = \int_{\Gamma e} b_i \left(\frac{f^{(n+1)} - f^{(n)}}{\Delta t} + \nu^{(n+1)} \frac{\partial f}{\partial r}^{(n+1)} - u^{(n+1)} \right) r dr} \quad (5.15)$$

As far as the current at the pore entrance is concerned, a sixth residual is considered in a similar fashion as in [1].

$$\boxed{R_6 = J - 2\int_{\Gamma e} (J_z - f_r) r dr} \quad (5.16)$$

The time derivative in the fifth residual is discretized in time using a fully implicit scheme and Δt is the dimensionless time step. The Jacobian Matrix of the coordinates transformation mentioned above reads:

$$|J| = \begin{vmatrix} \frac{\partial r}{\partial r} & \frac{\partial r}{\partial x} \\ \frac{\partial z}{\partial r} & \frac{\partial z}{\partial x} \end{vmatrix} = \begin{vmatrix} 1 & 0 \\ x\frac{\partial f}{\partial r} & f \end{vmatrix} = f(r) \quad (5.17)$$

Hence, the above system of equations and the boundary conditions are transformed into the r-x coordinate system where the following equalities hold:

$$\frac{\partial}{\partial r} = \frac{\partial}{\partial r} - x\frac{f_r}{f}\frac{\partial}{\partial x}, \text{ and } \frac{\partial}{\partial z} = \frac{1}{f}\frac{\partial}{\partial x} \quad (5.18)$$

and $dA = rdrdz = |J| rdrdx = rfdrdx$

Finally, the system of equations to be solved numerically takes the common form of a linear algebraic system

$$[A] \cdot \Delta\vec{x} = -\vec{R} \tag{5.19}$$

where $\vec{R}$ is the residual vector containing the residual entries at each element, [A] represents the Jacobian Matrix, which contains the partial derivatives of the residuals with respect to each of the unknown variables of the problem and $\Delta\vec{x} = \vec{x}_{new} - \vec{x}_{old}$ is the correction of the unknown vector, $\vec{x}$, during every iteration. Then, the potential solution at every single iteration is calculated via:

$$\vec{x}_{new} = \vec{x}_{old} + \Delta\vec{x} \tag{5.20}$$

and this process is performed until convergence.

Let n_{xel}, n_{yel} be the number of elements at x and r directions, respectively, as depicted in **Fig. 4.2**. Then, the number of nodes at each direction is

$$nnx = 2\, n_{xel} + 1,\ nny = 2\, n_{yel} + 1 \tag{5.21}$$

and the number of nodes used for the numerical procedure is

$$n_{total} = nnx \cdot nny \tag{5.22}$$

The two velocity components along with the magnetic induction field require 3 n_{total} equations in total and $(n_{xel}+1)(n_{yel}+1)$ for the pressure field. The shape interface demands nny equations and only 1 is needed for the unknown current J. Thus, the total number of equations-unknowns that consists the problem is

$$neq_{tot} = [\, 3\, n_{total} + (n_{xel}+1)(n_{yel}+1)\,] + nny + 1 = n_{band} + nny + 1 \tag{5.23}$$

The aforementioned system of equations produces a set of nonlinear equations with the Jacobian matrix, A, being in the form of an arrowhead matrix, [1]. An arrow matrix has nonzero elements only in a narrow band centered on the main diagonal and in the last few columns and rows. Hence, A matrix can be divided into four sub-matrices [1]:

1. A banded Jacobian matrix (J) of dimension (nband x nband) with derivative entries of the residuals relating to momentum balances, magnetic equation and continuity equation with respect to u_i, v_i, H_i and p_i.

2. A matrix in the form of a column (COL) of dimension n_{band} x (*nny*+1) with derivative entries of the residuals relating to momentum balances, magnetic equation and continuity equation with respect to f_i and *J*.
3. A matrix in the form of a row (ROW) of dimension n_{band} x (*nny*+1) with derivative entries of the residual relating to the kinematic condition with respect to u_i, v_i, H_i and p_i.

4. A matrix in the square arrowhead at the bottom right (HEAD) of dimension (*nny*+1) x (*nny*+1) with derivative entries of the residual relating to the kinematic condition and current conservation at the pore entrance with respect to f_i and *J*.

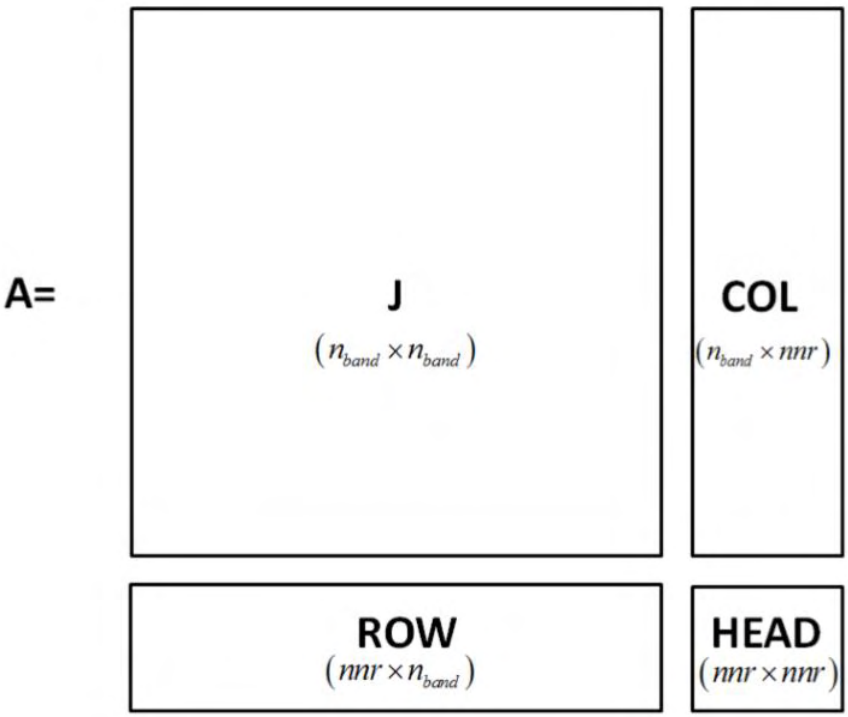

Fig. 5.2 Illustration of the Arrowhead Matrix, taken from [1]. Here nnr = nny.

After storing the above equations in the above form, during each iteration of the Newton Raphson procedure, A matrix is inversed by a standard routine written for arrow matrices and the unknown vector is calculated.

5.4 Grid Independence and Code Validation

Before proceeding to the results concerning the replenishment process under the influence of an external magnetic field, it is necessary to conduct a series of simulations with different number of elements in order to choose a suitable computational grid. Within this context, a cylindrical pore of radius $R_p = 30$ μm was considered, which is an acceptable value according to Lyublinski et al [18] for proper CPS performance. Besides, a tube height of $h_0 = 1$ mm was chosen. The material properties for the liquid into consideration were calculated at temperature T = 300 °C from [33]. Liquid lithium material properties were set to $\rho = 505$ kg/m^3, $\mu = 2.287 \times 10^{-3}$ Pα s, $\gamma = 0.314$ N/m and $g = 9.81$ m/s^2 the acceleration due to gravity. The constant contact angle was set to $\theta_c = 30^o$ and the reservoir overpressure $\Delta p = p_r - p_{out} = 0$ Pα. Thus, by setting the reservoir overpressure to zero, the lithium flow is purely capillary-driven. Moreover, the current density entering the pore and hitting upon the interface was considered known and specifically with components $J_r = 10^5$ A/m^2 and $J_z = 0$. The intensity of the applied magnetic field was set to an acceptable value for fusion related applications, $B_0 = 1$ T. In order to study the grid independence of the problem with the aforementioned parameters, a series of simulations with increasing number of elements was conducted starting from a relatively small grid of 300 elements up until 4800 elements. The results correspond to various distributions along the interface at the same time instant. These are the axial velocity profile, u, and the Magnetic Induction profile at the interface at various time instants and the velocity and position of the uppermost point of the liquid column in contact with the solid wall as functions of time.

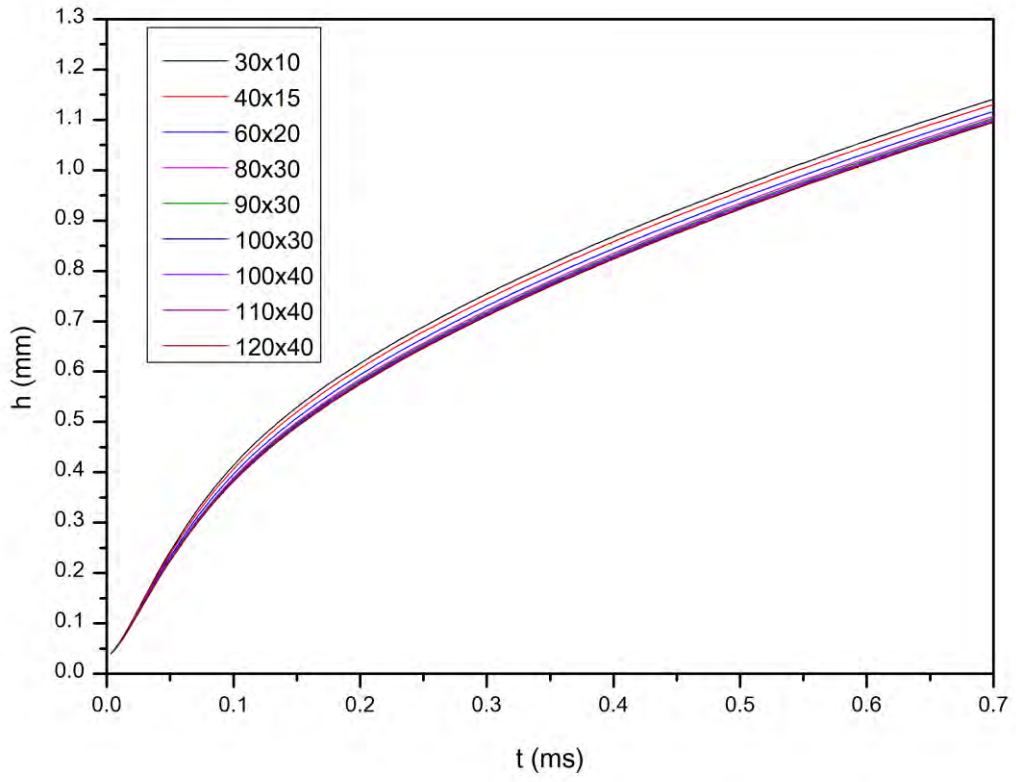

Fig. 5.3 Time evolution of the meniscus height calculated at r=1 (contact point location) for different grids.

As far as the latter is concerned, the meniscus height, h, as a function of time was calculated for a time period corresponding to 0.7 ms as can be seen in **Fig. 5.3**. It is deduced that the time for the liquid to exit the pore, or, in other words, the time at which the column height barely exceeds the capillary tube height h_0=1mm, is between 0.57 and 0.59 ms, depending on the exact number of elements. The corresponding temporal evolution of the liquid metal rising velocity is plotted for each of these grids in **Fig. 5.4** along with an enlargement of the area between 0.012 and 0.045 ms where discrepancies between grids are large. As a result, the choice of a mesh between 100x40 and 120x40 is capable of achieving an acceptable numerical solution.

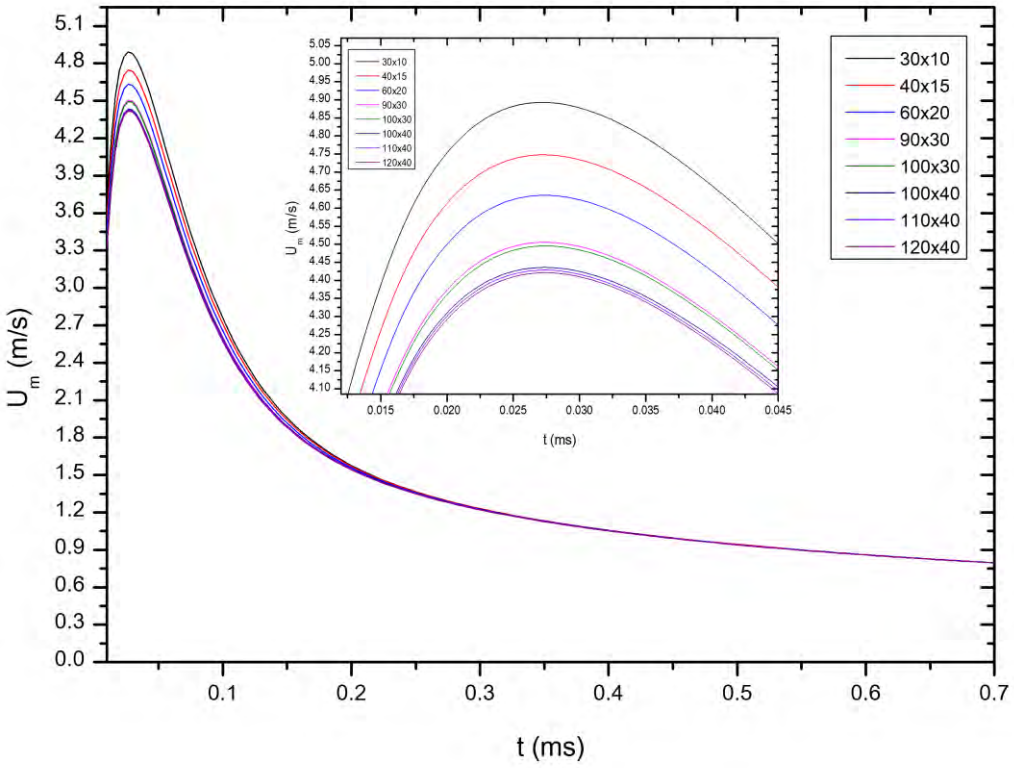

Fig. 5.4. Temporal evolution of the meniscus contact point velocity. Note that the time needed for maximum velocity is the same for every grid, between 0.0275 and 0.03 ms.

However, in order to obtain further information on the accuracy of each of the aforementioned computational grids, the axial velocity and magnetic induction at the interface are plotted against r (radial distance) at the same time instant. The results are illustrated in **Fig. 5.4** and correspond to a time instant of 0.164 ms. According to those comparisons, the 110x40 grid is selected since any further grid refinement shows small numerical differences.

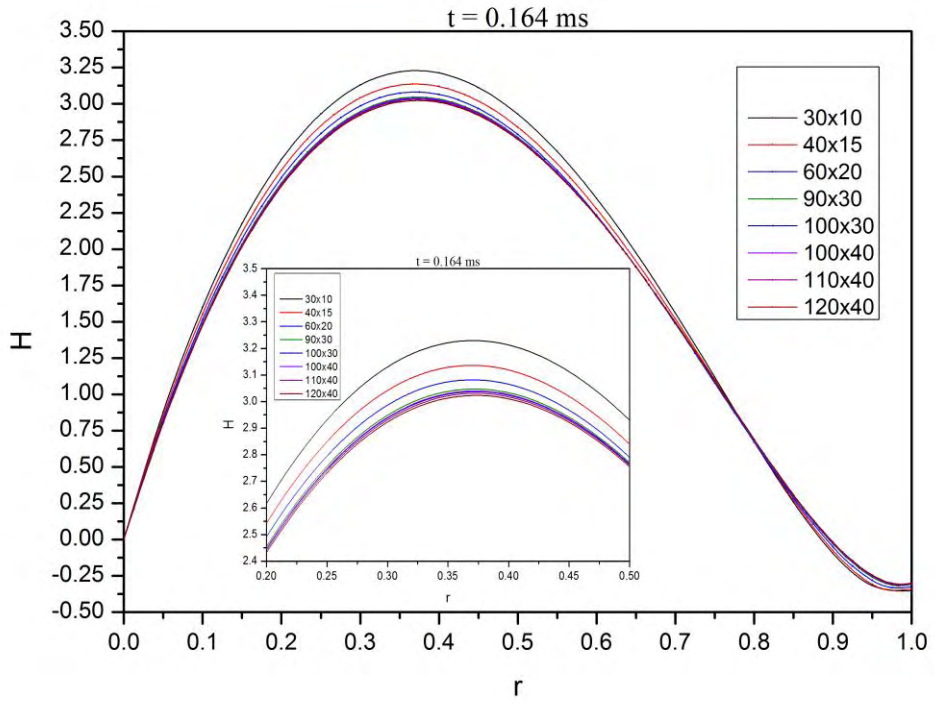

a)

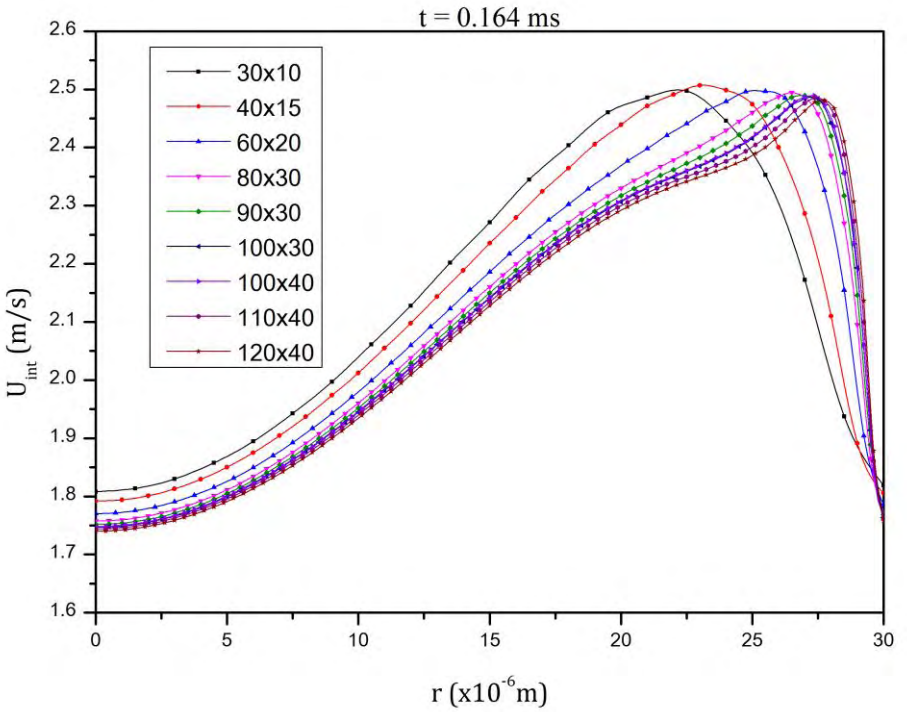

b)

Fig. 5.5 a) Induced magnetic field profile and b) Axial velocity profile at the interface at t = 0.164 ms. Note that in a) H is normalized by $J_r R_p$ and r by the pore radius, R_p.

Our next intention is to validate the mathematical model deployed in this chapter. As a validation study, the purely hydrodynamic case was studied. For this purpose, the Magnetic field was set to zero with arbitrary J_r, J_z currents since in this case there is no MHD effect. The results obtained were compared to those of an existing code which solves the problem of transient capillary rise of Li inside a single pore without magnetic field formulation. As it is seen in **Fig. 5.6**, the numerical results obtained from the present code are in complete agreement with the hydrodynamic results provided by the previous code.

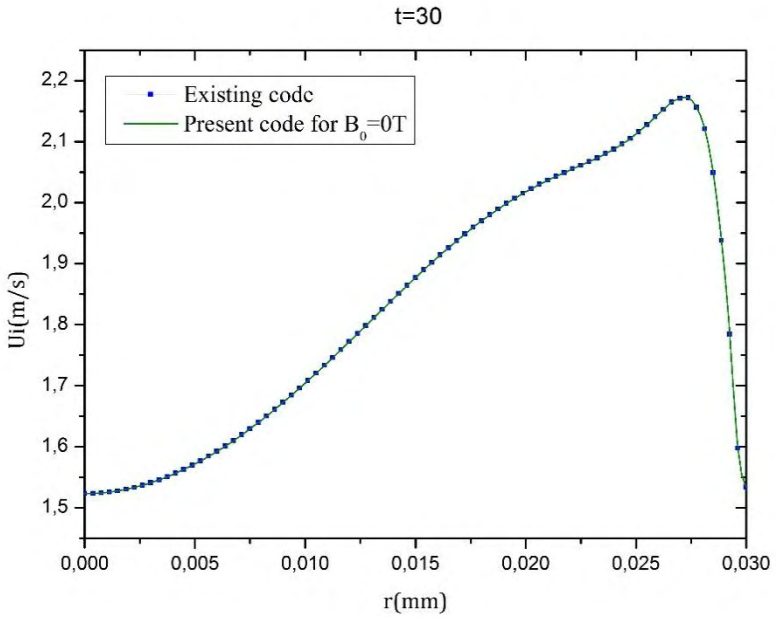

i)

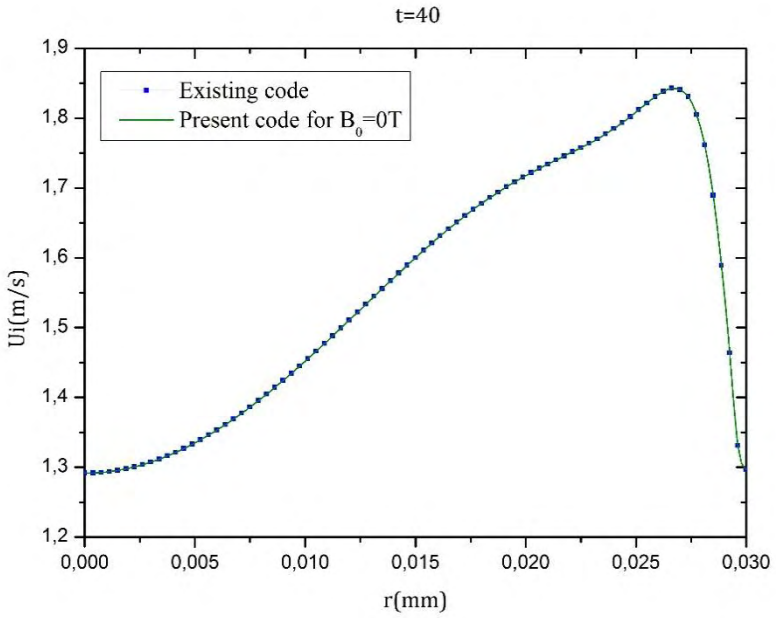

ii)

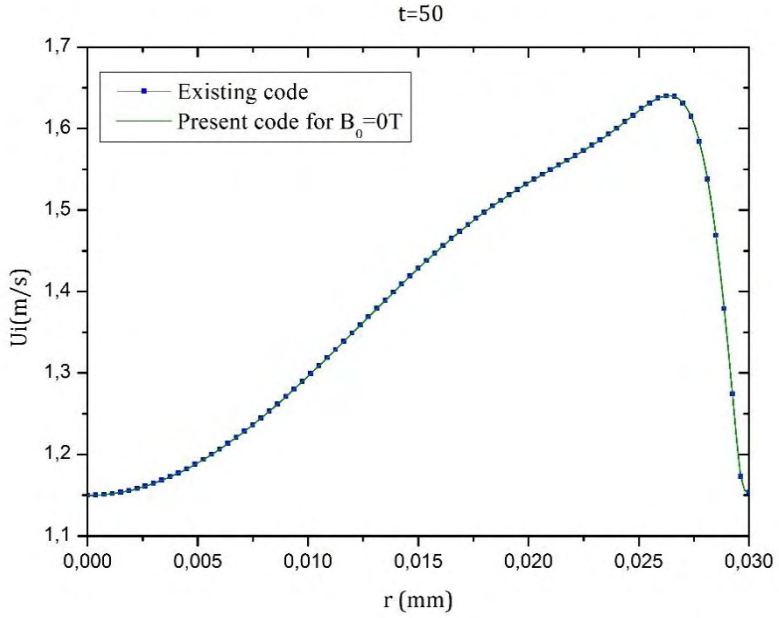

iii)

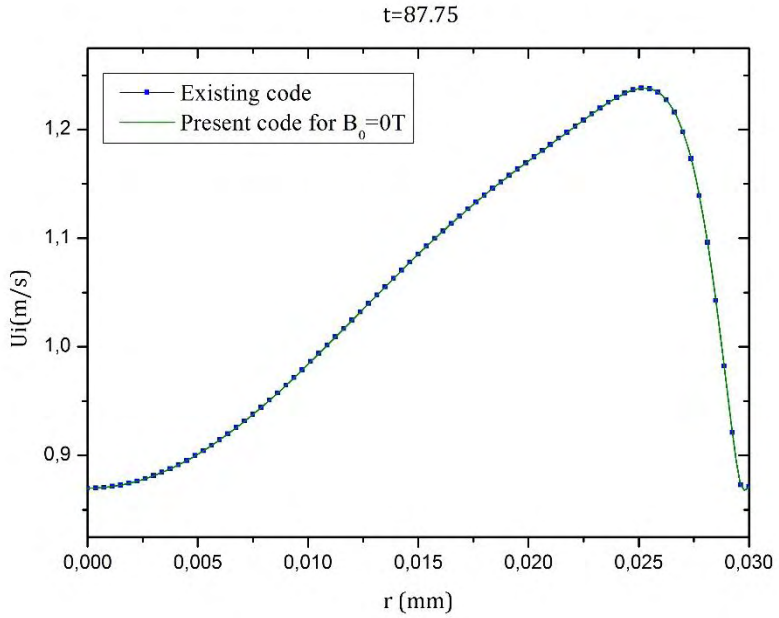

iv)

Fig. 5.6 Axial velocity profile exactly at the interface for i) t = 30, ii) t = 40, iii) t=50 and iv) the time instant at which the liquid exits the pore (dimensionless time instants).

Moreover, the code was also tested for the hydrodynamic case without inertia. In order to run this simulation, the We number in Eq. 4.43 was set to zero, thus the simulation corresponded to Stokes Flow [8, 42]. In **Fig. 5.6**, the liquid metal rising velocity is plotted against time for the case with and without inertia. Large discrepancies between the two curves appear only during the initial stage of wicking and after some time the two velocities seem to be almost equal, with numerical deviations

during the quasi-steady regime being almost negligible. This proves that during the exit of the liquid from the pore the exit velocity of the column is almost equal to that of the inertialess case, implying that inertia in this case is important only during the first stages of wicking, in which the meniscus tip temporal velocity exhibits a transient behavior. This result was reported in [1]. The blue curve was obtained using the formula $\gamma R_p/(\mu h_0)$ for the velocity scale since, in the case without inertia, capillary pressure balances the axial pressure drop [1]. Moreover, the rate at which the velocity changes over time during the quasi steady regime is very slow but nonzero, therefore static equilibrium within the pore of height h_0 = 1mm is far from being reached. This due to the fact that the actual equilibrium height in this case is given by Eq. 4.3 and is about h_{eq} = 3.65 m

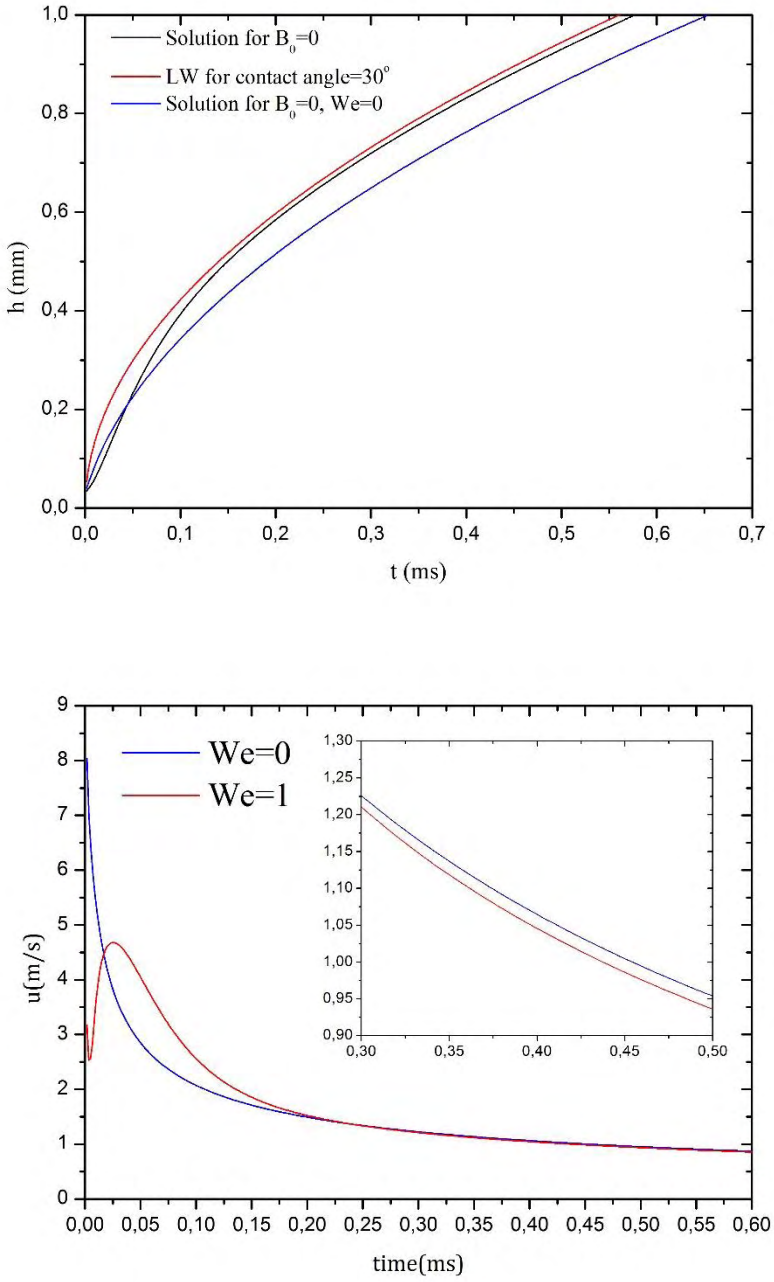

Fig. 5.7 Temporal evolution of the meniscus tip height and velocity for B_0 = 0T with and without inertia

Besides, the curve corresponding to the temporal evolution of the meniscus height for the inertialess case is bellow Lucas-Washburn curve. The last result was demonstrated in [1].

Lastly, in order to further validate the code developed for this problem, it was investigated if the results of the static case demonstrated in [1] could be reproduced by the code developed for this problem. Therein, the case for a completely rectangular physical domain (flat interface) and $J = J_z = 0$ was studied analytically and Eq. 4.12 was solved under the assumption of static equilibrium ($v = 0$). In order to solve Eq. 4.12 with zero RHS, the magnetic field intensity was set to zero while the contact angle to 90^o. Since $\theta_c = 90^o$ and $J_z = 0$, then according to Eq. 3.25, the gradient $\partial f / \partial r = 0$ so the integral evaluating the current density at the pore entrance vanishes and $J = 0$. Note now that the Boundary Value Problem derived in Chapter 3 does not contain time, thus, the solution for H is expected to be independent of time. The results obtained showed that the Induction distribution along the interface did not vary from a time instant to another and the profile obtained can be seen in **Fig. 5.8** where both H and r are in dimensionless form. Compared to the exact solution presented in **Fig. 5.9**, the two curves are in good agreement.

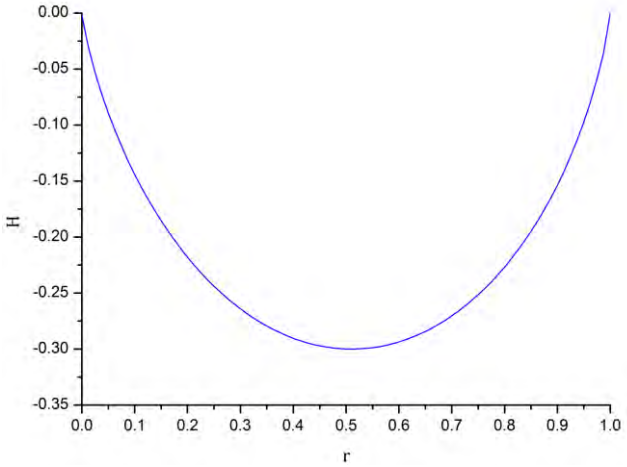

Fig. 5.8 Interfacial Magnetic Induction for the case of a flat interface.

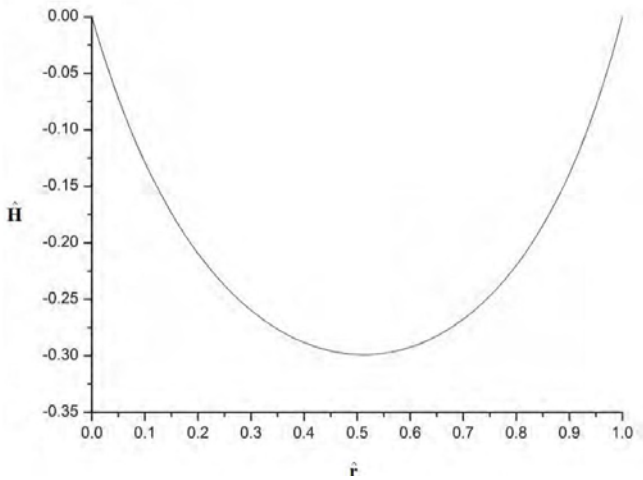

Fig. 5.9 The exact solution at the interface for rectangular geometry, from [1].

Chapter 6: Results

In this Chapter, the results of the numerical analysis deployed in order to solve the system described in the previous Chapter are presented. The analysis focused on altering the intensity of the applied magnetic field and the components of current density exactly at the interface. Firstly, the analyses performed focused on the case of constant current density at the interface with increasing the value of the magnetic field intensity. Then, an analysis of constant magnetic field intensity with increasing the interfacial current is conducted in order to examine the conditions under which the magnetic field can cause drop ejection or instability. In the final section of the results, the effect of varying pore radius for a specific value of the imposed field and interfacial current is investigated.

6.1 Numerical and problem parameters

As it is stated in the previous Chapter, a mesh of 110 x 40 = 4400 biquadratic Lagrangian elements is used in order to carry out a series of numerical simulations, each one of them corresponding to a different Bo_m. Since the liquid metal rises within a pore of height h_0 = 1mm, each simulation is terminated as soon as the liquid column barely exceeds this height. The material properties of the fluid, the contact angle and the other input parameters used in this Chapter are the same as those considered for the benchmark test and can be seen in **Fig. 6.1**

Problem Parameters

Parameter	Value	Units
γ	0.314	N/m
σ	3.28×10^{6}	S/m
ρ	505	kg/m^3
μ	2.287×10^{-3}	Pa s
R_p	30	μm
B_0	1-7	T
J_r	10^4-10^9	A/m^2
l	30	nm
θ	30	degrees

Fig. 6.1 List of material and geometrical properties of the the present problem.

Since we are interested in studying the influence of the emerging Lorentz Force on the capillary rise of Li within the pore and the Li material properties are constant, the only parameters that change if

the Magnetic field strength or the current at the interface are altered, are the magnetic Bond, Bo_m, and the dimensionless induction source, $c = \sigma B_0 \hat{u}/J_r$. The CPS is placed in the Divertor section, where the value of the intensity of the imposed magnetic field B_0 is a few T. The two components of the interfacial current density, J_r and J_z, were altered in a way corresponding to normal and off normal conditions. This is due to the fact that this current is generated by the plasma confined in the chamber and can reach high values corresponding to ELMs. Accordingly, its characteristic value, namely J_r, can be set to even 10^9 Am^{-2} [1]. Based on the above, the magnetic Bond number for B_0 = 1T lies between 2.86×10^{-5} and 2.86 for $J_r = 10^4$ A/m^2 and $J_r = 10^9$ A/m^2, respectively, while the c parameter between 1.49×10^{-2} and 5792. Therefore, the results are expected to vary significantly since c ranges from values below unity to $c \gg 1$. As far as the rest parameters are concerned, the We, Ca and Bo numbers remain fixed for constant material parameters and pore radius. The characteristic flow velocity is given by Eq. 4.41 and according to the definition of Weber number, We = 1 regardless of the material properties. This is due to the fact that inertia is expected to be important for the case of a fully time dependent flow. The gravitational Bond number of the flow is 1.41×10^{-5}, significantly less than 10^{-3}, implying that gravitational effects are not expected to play a considerable role [29]. The Capillary number is 3.31×10^{-2}. Lastly, the Reynolds numbers of the flow ($Re = \rho \hat{u} R_p/\mu$), although not a part of the mathematical formulation presented in Chapter 4, is about Re = 30. Also, this dimensionless number is not independent parameter since it is apparently written as $Re = We/Ca$. In other words, neither $Re \ll 1$ nor $Re \gg 1$. Therefore, since Re = O(10), inertia terms were included in all of the simulations.

6.2 Results for the case of constant interfacial current density

6.2.1 Zero axial component ($J_z = 0$)

Firstly, the case of a constant current entering the liquid metal open surface is studied in order to examine the conditions under which the Lorentz forces accelerate or decelerate the LM rising within the pore. Specifically, the component along the axial z direction, namely J_z, was set to zero and two different values for the radial component J_r were tested. For the first case, J_r was set to the relatively small value of $J_r = 10^4$ A/m^2.

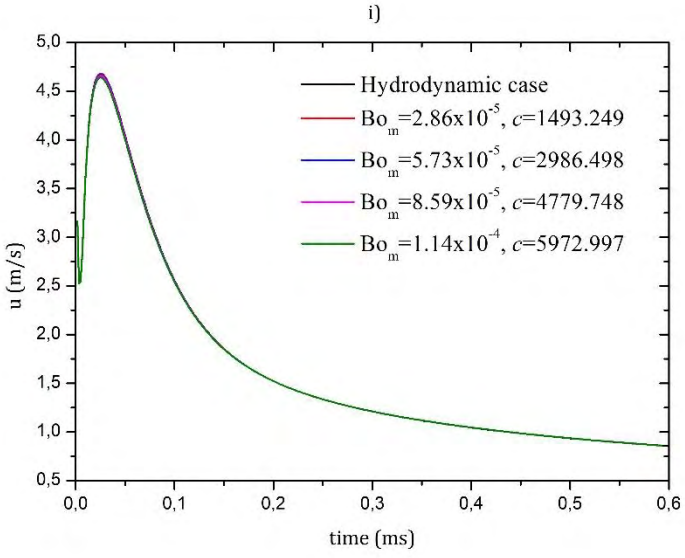

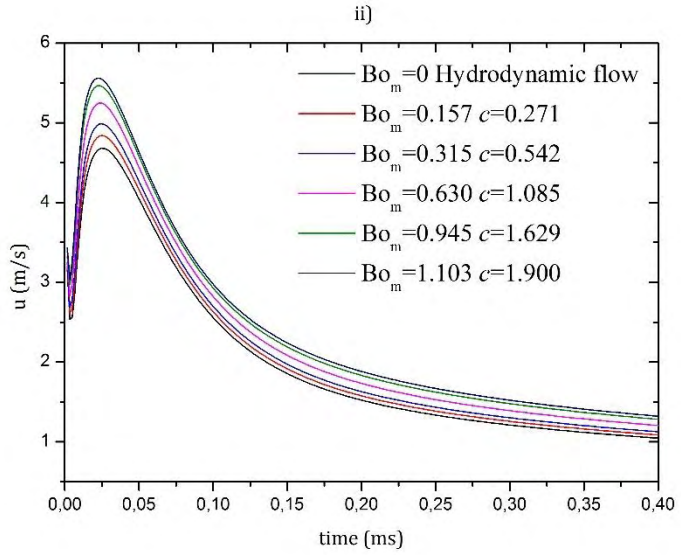

Fig. 6.2 Temporal evolution of the velocity at the contact point for i) Jr = 10^4 A/m^2 and B0 = 1, 2, 3, 4 T and ii) for Jr = 5.5x10^7 A/m^2 and B_0 = 1, 2, 4, 6 and 7 T.

Nonetheless, cases in which J_r is high enough to produce a magnetic Bond comparable to or grater than unity are also probable in a Tokamak environment. Accordingly, a second value for J_r was tested, J_r = 5.5x10^7 A/m^2. The intensity of the imposed magnetic field is chosen between 1 and 4 T for the first case and between 1 and 7 T for the second. Every case is compared to the hydrodynamic flow. The latter is obtained by setting B_0 = 0T. The results of the first case pertaining to the rising velocity are shown in **Fig. 6.2** i) where the temporal evolution of the meniscus tip velocity is presented. It is shown that for such small current density where Bo_m ~10^{-5} the LM rising velocity seems to be the same with the case of zero magnetic field and also the time needed for exit is the same for every Bo_m. Only during the period the liquid approaches its maximum velocity an increase of the magnetic field intensity slightly reduces its rising velocity. On the contrary, the results for the case of J_r = 5.5x10^7 A/m^2 are quite different. To be specific, **Fig. 6.2** ii) illustrates the rising velocity for the aforementioned current density with the imposed field ranging from 1 to 7 T. It shows that the maximum velocity and generally the rising velocity increases with Bo_m. Here Bo_m ~ 10^{-1} and the c number is comparable to unity whereas in the first case c ranges from 1493 to 5792 ($c \gg 1$). This realization implies that when $c \gg 1$, the dominant expression for the Lorentz force is the Ohmic part given by Eq. 3.9. Indeed, by combining Eq. 3.9 and Eq. 3.7 results in a Lorentz force that opposes the liquid's vertical motion. In addition, the c parameter represents a ratio of two different characteristic current densities, with the numerator coming from Ohm's law (Eq. 3.9). Hence, in the first case the Ohmic current is the dominant one compared to J_r whereas in the second case in which these two currents are comparable in magnitude, the dominant part of the Lorentz forces is given by Eq. 3.13. Moreover, **Fig. 6.3** illustrates the time evolution of the column height for the second case, where Bo_m increases towards unity and shows that as the latter increases the time required to exit the pore decreases. In general, in the case of magnetic propulsion an increased Lorentz force results in a decreased required time for exit. Besides, it is worth noting that for every case the maximum velocity is achieved roughly at the same time. Presumably, this is attributed to the fact that the material proper-

ties and the pore radius are the same for each of the simulations stated above and, thus, the viscous time scale remains fixed. The latter is defined as $t_2 = \rho {R_p}^2/\mu$ and provides an order of magnitude estimate for the time needed to enter the quasi steady regime [16, 43]. According to **Fig. 5.7** and **Fig. 6.2**, an almost steady state velocity is obtained at 0.55 ms and here $t_2 \approx 0.2$ ms. So, they are of the same order of magnitude. Based on the above statement, if the pore radius is increased, the time needed for a quasi steady behaviour, similar to that of **Fig. 5.7, Fig. 6.2**, will be greater.

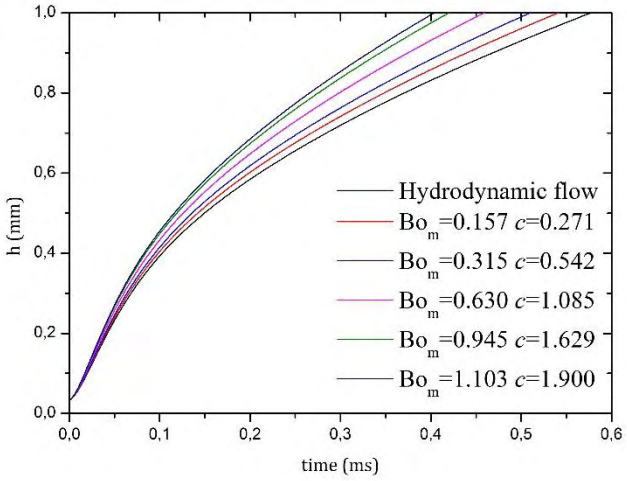

Fig. 6.3 Time evolution of the liquid metal column for Jr = 5.5x10^7 A/m^2.

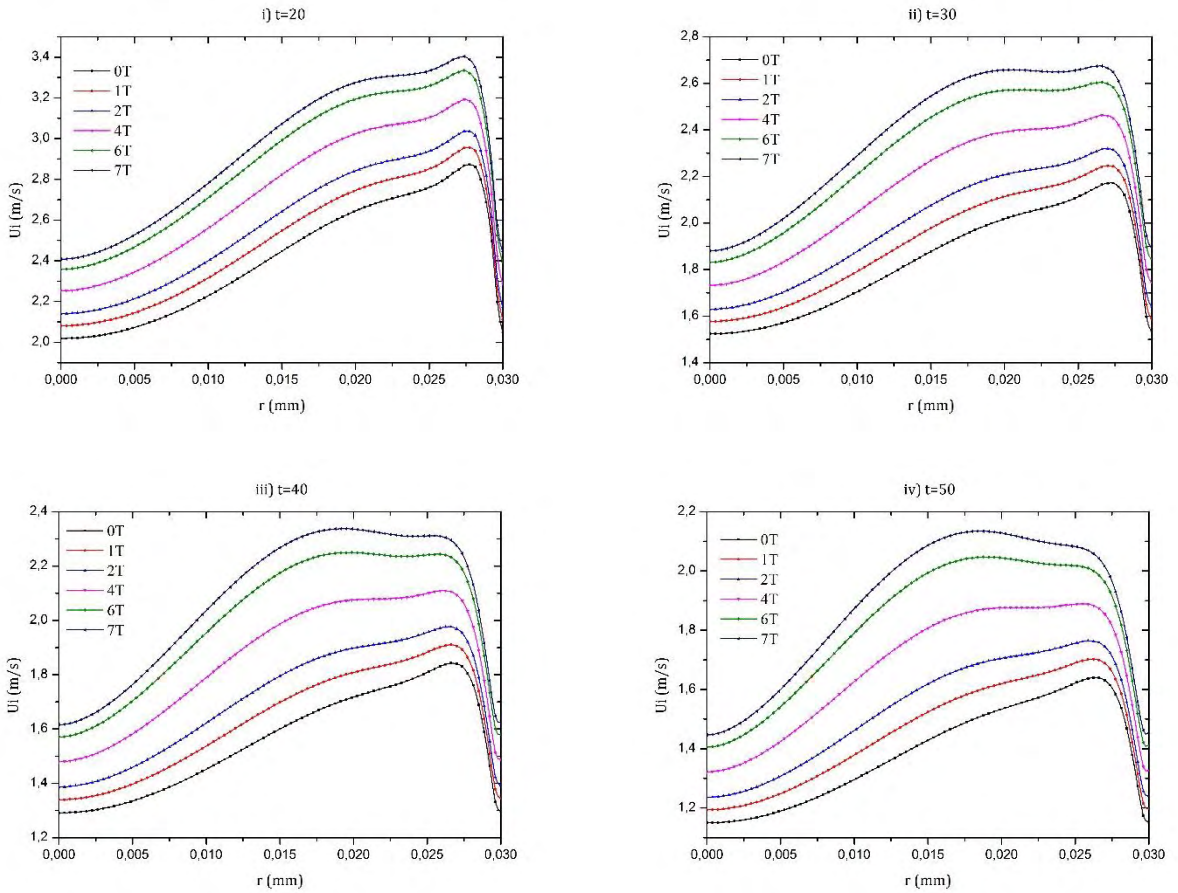

Fig. 6.4 Velocity profiles (z component) at the interface for Jr = 5.5x10^7 A/m^2 i) t=20, ii) t=30, iii) t=40 and iv) t=50.

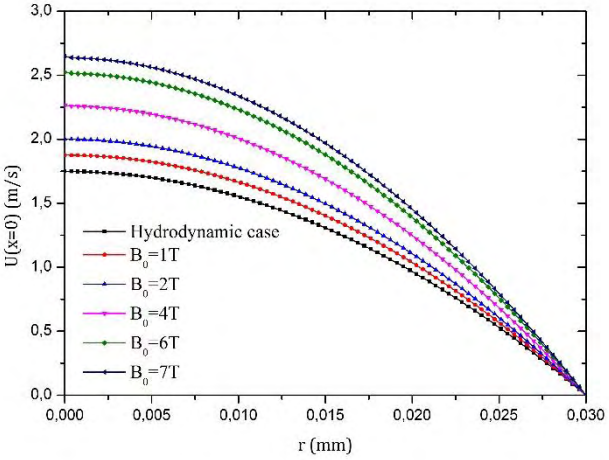

Fig. 6.5 Velocity profile for z velocity at the pore entrance (z = 0) during the liquid's exit for Jr = 5.5x10^7 A/m^2.

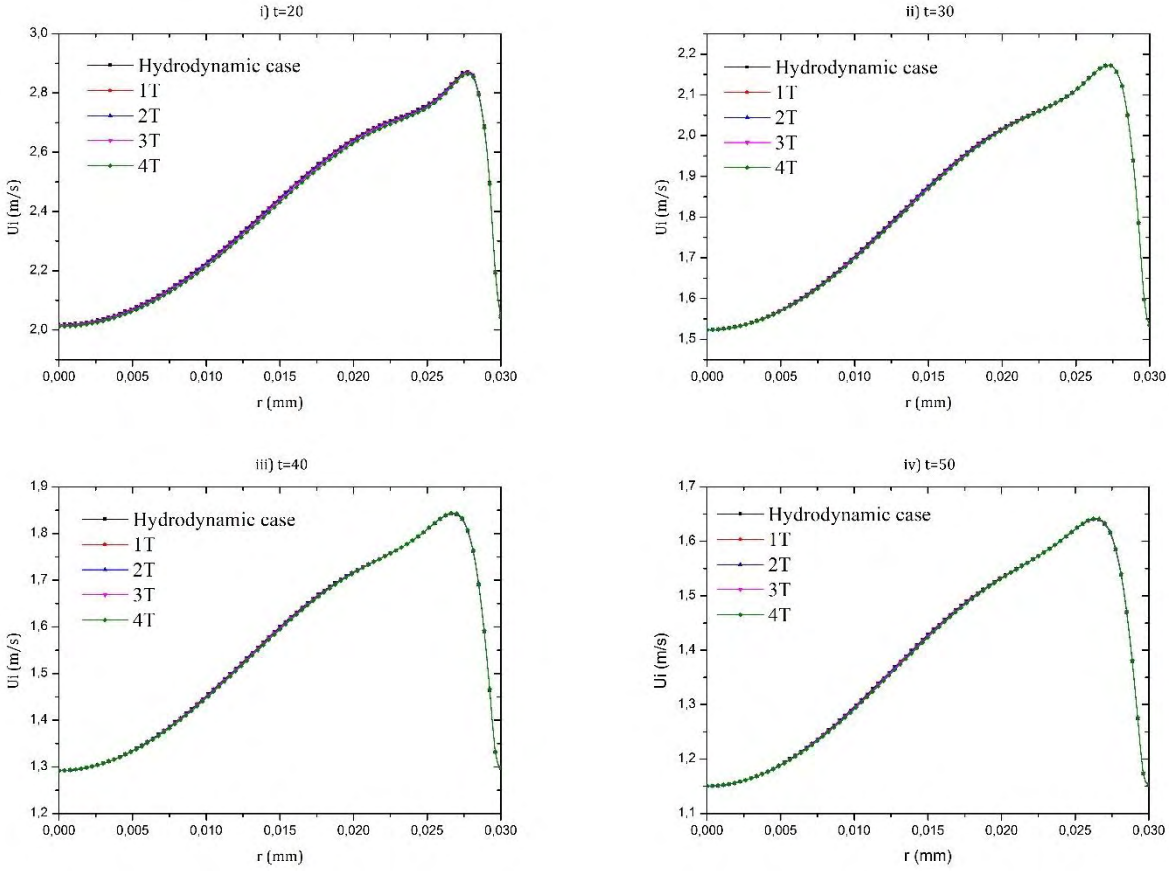

Fig. 6.6 Velocity profiles (z component) at the interface for Jr = 10^4 A/m^2.

The next set of results provide a more detailed look on the flow regime of the liquid column. Specifically, the figures above represent the axial velocity profiles at the interface and at the pore entrance obtained for various time instants. In **Fig. 6.4** the interfacial velocities u(r, z = f(r)) for t = 20, 30, 40 and 50 and Jr = 5.5x10^7 A/m^2 are illustrated. At t = 20 every profile seems to have the same shape with the hydrodynamic one. However, as time progresses its shape gradually begins to differ from

the latter. This realization is further enhanced by observing the position along the interface at which the maximum of the profile is positioned. For $B_0 \leq 2T$ the peak value of Ui appears near the solid boundary ($r = R_p$) and as B_0 is further increased and Bo_m exceeds unity, the profile appears distorted with its maximum value being moved towards r = 0. However, this behaviour is seen only for the case of $J_r = 5.5x10^7 A/m^2$, or, in other words, when $Bo_m = O(10^{-1})$. **Fig. 6.6** shows the interfacial velocity profiles for the case of $J_r = 10^4 A/m^2$ where, unlike **Fig. 6.4**, the results obtained coincide with the hydrodynamic case. At the pore entrance the velocity follows a parabolic shape for both cases, shown in **Fig. 6.5** and **6.7**, resembling the well-known Poiseuille profile.

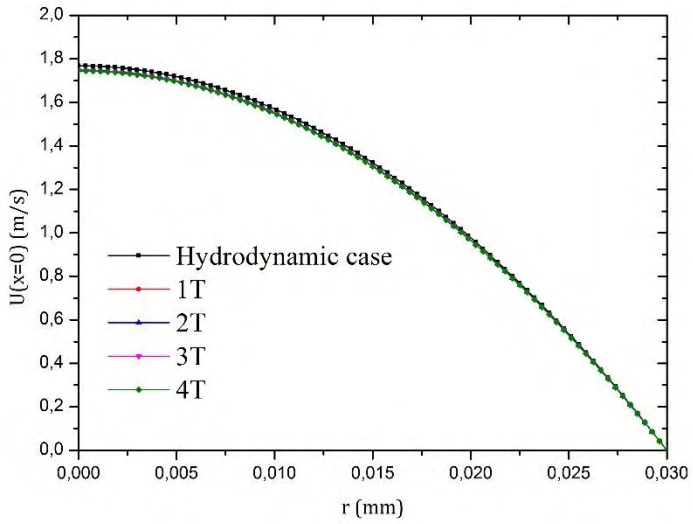

Fig. 6.7 Velocity profile for z velocity at the pore entrance (z = 0) during the liquids exit for $Jr = 10^4 A/m^2$.

Continuing with the results at the interface, the magnetic induction is plotted against r at two discrete time instants for the two cases investigated so far. Our next intention is to examine the general effect of the magnetic field on the interface for the cases $Bo_m \ll 1$ and $Bo_m \in [0.157, 1]$. In **Fig. 6.8** it is observed that for $J_r = 5.5x10^7 A/m^2$ the magnetic stream function profiles express a negative pressure exactly at the interface. According to the normal stress balance at the interface, the negative sign of H in the left scale of Eq. 4.20 creates an extra overpressure from the side of the liquid. Based on the above, the mean curvature of the free surface is expected to be increased compared to the capillary driven flow, where $Bo_m = 0$, implying that the position of the free surface is going to be above from that of the hydrodynamic case. Indeed, the corresponding shape for t = 10 and t = 20, depicted in **Fig. 6.8** iii)-iv), exhibits the aforementioned theoritical prediction.

t=10

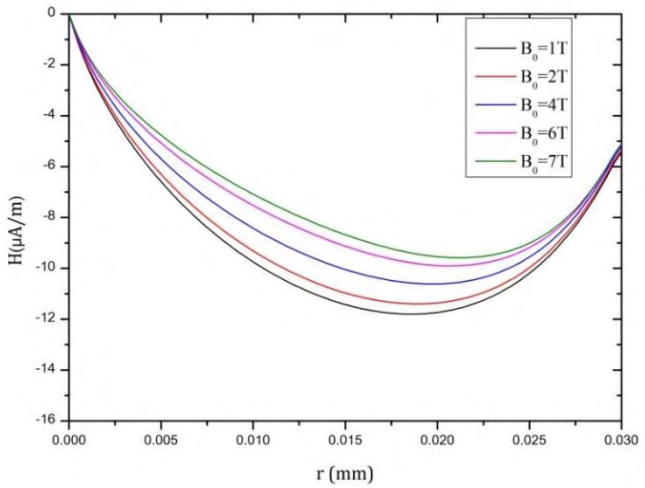

t=20

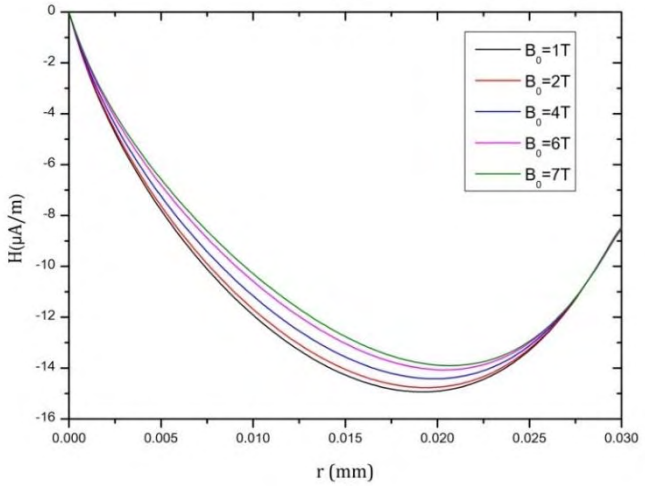

iii) t=10

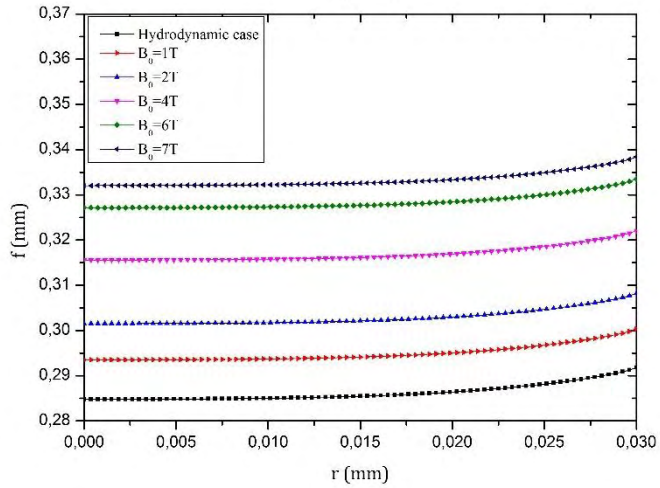

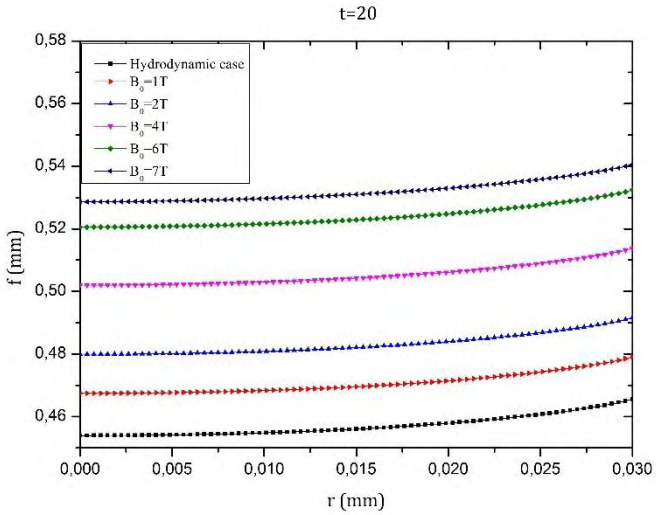

Fig. 6.8 Magnetic Induction profile i)-ii) and interface iii)-iv) obtained for Jr = 5.5x10^7 A/m^2 at t = 10 and t = 20.

In a similar fashion, for the case of $J_r = 10^4$ A/m^2 where c is much larger that one and a phenomenon of magnetic braking of little magnitude was observed above, the magnetic pressure is positive resulting in free surface positions slightly below that of zero magnetic Bond number, as it is explicitly illustrated in **Fig. 6.9**. As it has been stated in Chapter 4, the magnetic pressure is expressed by $P_m = B^2/2\mu = B_0 H$ therefore, it is either negative or possitive depending on the sign of H. At this point it is of importance to underline the fact that although increasing the value of B_0 increases not only the magnetic Bond but the c number as well, the braking effect is negligible and observed only in the first case, where $Bo_m \ll 1$. Only in the second case ($J_r = 5.5x10^7 A/m^2$) the liquid flow is obviously affected by the applied magnetic field. This is due to the fact that only in the latter case, where $Bo_m \sim 10^{-1}$, the magnetic effects and specifically the MHD related pressure begin to play an important role in the dynamics of capillary rise, apart from surface tension.

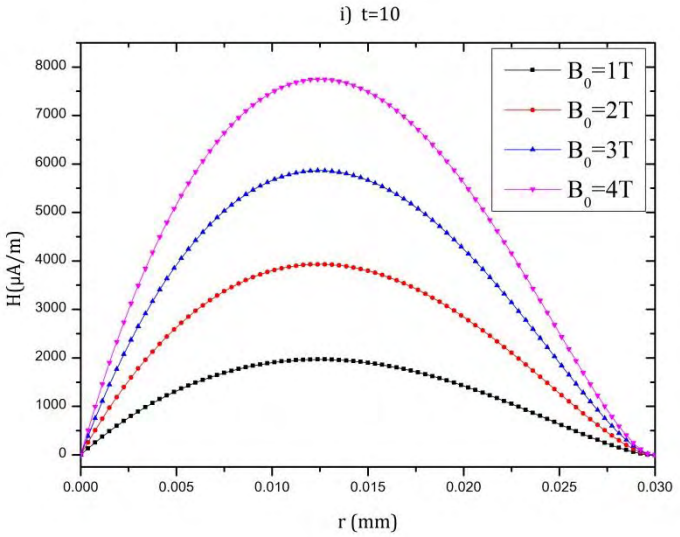

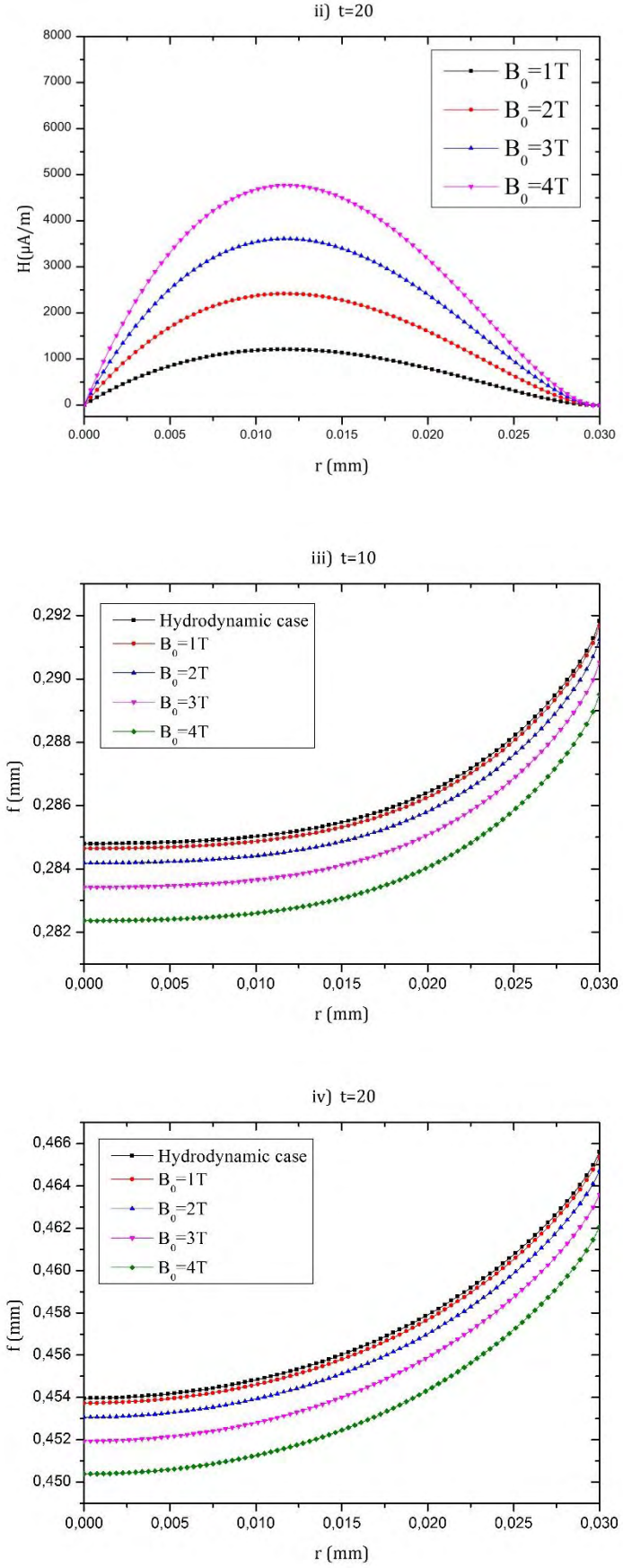

Fig. 6.9 Magnetic Induction profile i)-ii) and interface iii)-iv) obtained for Jr = 10^4 A/m^2 at t = 10 and t = 20.

Consequently, according to the above results the LM velocity and the flow field in general are affected by the magnetic field only if Bo_m exceeds a certain value. This value should be $O(10^{-1})$.

6.2.2 Nonzero axial component ($J_z \neq 0$)

Following the simulations conducted above, the effect of a nonzero axial current ($J_z \neq 0$) at the interface was studied next and compared with the $J_z = 0$ case. Two different values.The intensity of the imposed field was set to $B_0 = 2T$ and $J_r = 5.5x10^7$ A/m^2. Three different values of J_z were tested, $J_z = -10x10^7$, $2.5x10^7$ and $5x10^7$ A/m^2. According to the definition of the magnetic Bond number and the c number, since J_r and B_0 are fixed these two dimensionless parameters remain unchanged. Their values are $Bo_m = 0.315$ and $c = 0.543$ and based on the results analysed in Subsection 6.2.1 the effect of the magnetic pressure is comparable with the capillary pressure. At the same time, it accelerates the fluid. As far as velocity is concerned, when J_z is comparable with J_r in magnitude, it either accelerates or produces a braking effect depending on its sign, as seen in **Fig. 6.10**. Specifically, for $J_z < 0$ the rising velocity as well as the axial velocity profile at the pore exit is

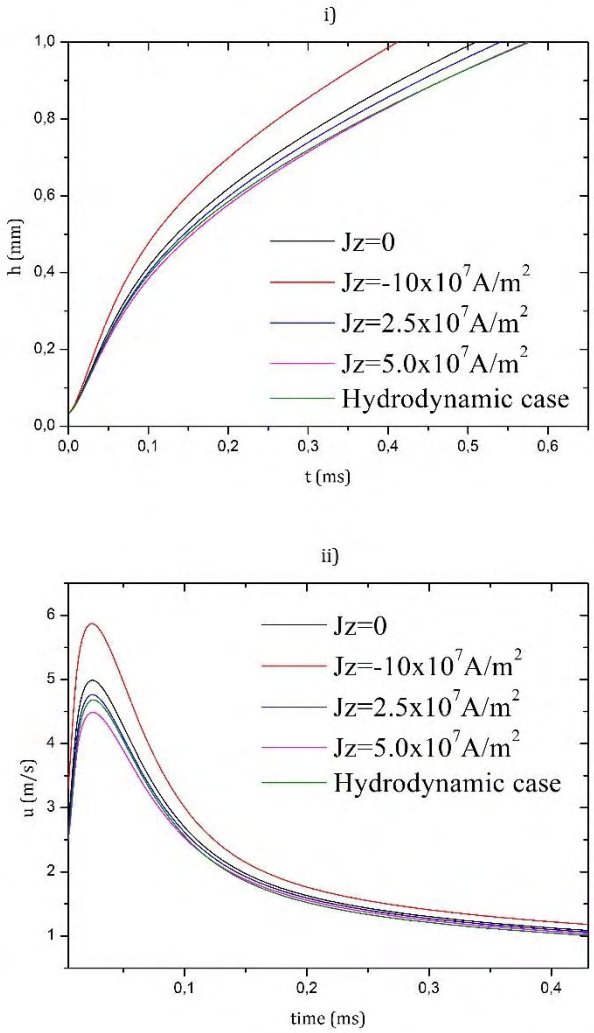

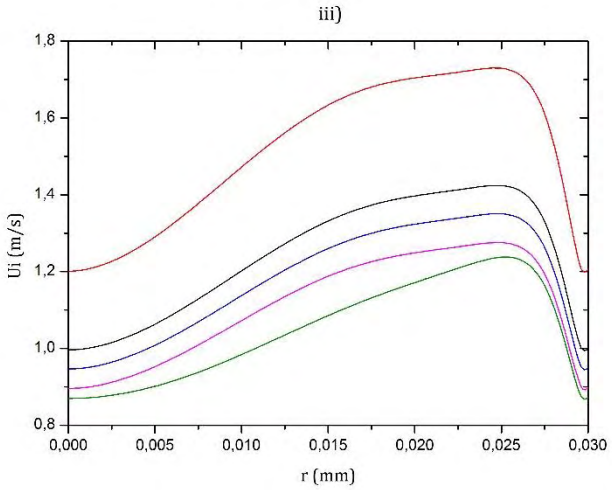

Fig. 6.10 Results for the case of nonzero current z component i) temporal evolution of the liquid column and ii) interfacial axial velocity profile at $z = h_0$ level and iii) axial velocity profiles at the exit of the pore.

greater than that corresponding to zero J_z. However, for $J_z > 0$, opposite results are observed. To be specific, a positive J_z results in a rising velocity which is smaller than that of the $J_z = 0$ case. Most importantly, the aforementioned case is seen to produce results matching those of the Hydrodynamic case. Therefore, if the z component points towards the pore exit and is equal or even greater than J_r in magnitude, magnetic braking is noticed with the Bo_m being unaffected, while in the opposite direction, the velocity is further enhanced.

In conclusion, the effect of the emerging Lorentz forces for magnetic field intensities of several T heavily depends on the magnitude of the radial component of the current density entering the CPS via the liquid gas interface within the pore. If $Bo_m \geq 10^{-1}$, the LM flow velocity can either be increased or decreased. This depends on the direction of the z component of the aforementioned current, provided that its components are of the same order of magnitude.

6.3 Results for the case of constant B_0 and varying current

Following the results presented and discussed in the previous section, the next case under investigation studies the effect of increasing the value of the current entering the capillary mesh via the liquid-gas interface while the applied field remains constant in magnitude. The value of the external field, B_0, was set to 1T and $J_z = 0$ for simplicity. Eight different values for J_r were tested as seen below.

Table 1: Values of Bo_m and c dimensionless parameters at 1 T

Jr (A/m^2)	10^4	10^5	$1.5x10^7$	$5.5x10^7$	10^8	$5.5x10^8$	$7x10^8$	10^9
c	1493.249	149.325	1	0.271	0.149	0.027	0.013	0.014
Bo_m	$2.86x10^{-5}$	$2.86x10^{-4}$	$4.27x10^{-2}$	0.157	0.286	1.576	2.006	2.866

The results concerning the meniscus tip velocity and position are depicted below in **Fig. 6.11**. It is observed that when $c = 1$ (pink curve in both panels) the fluid slightly starts to accelerate and as J_r is further increased, the accelaration is even greater. From a hydrodynamic point of view, this significant increase of the rising velocity should be attributed to an increaced pressure drop along the main flow direction (z-direction). In order to investigate this arguement, the dimensionless results corresponding to the thermodynamic pressure at the center of the radial distance ($r = R_p/2$) are plotted against the vertical direction, x, at three different time instants. The characteristic pressure is the same for every case, $p_c = \gamma/R_p$. From **Fig. 6.12** it is clear that pressure follows a linear behaviour with a negative and constant pressure gradient at every case. The total pressure drop from the entrance of the pore (x = 0) to the free surface (x = 1) increases gradually with Bo_m since every pressure curve ends up in the same value at x = 1.

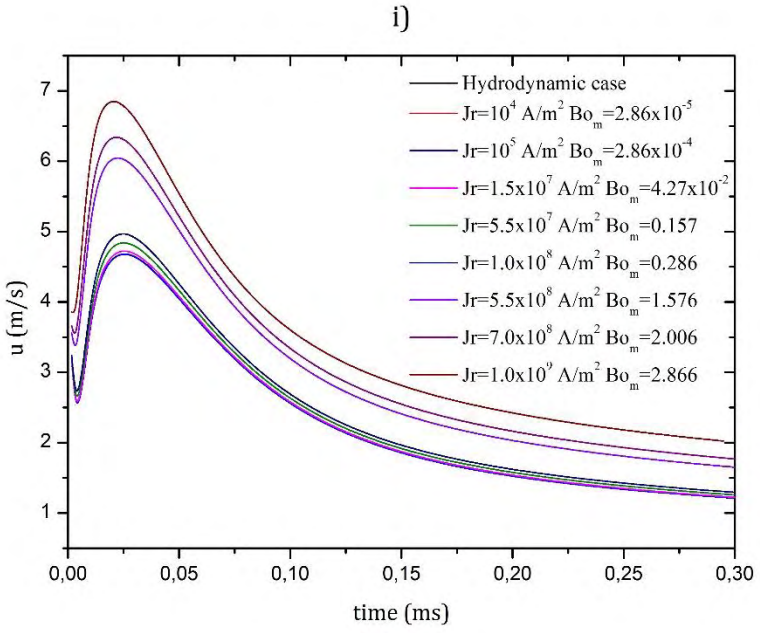

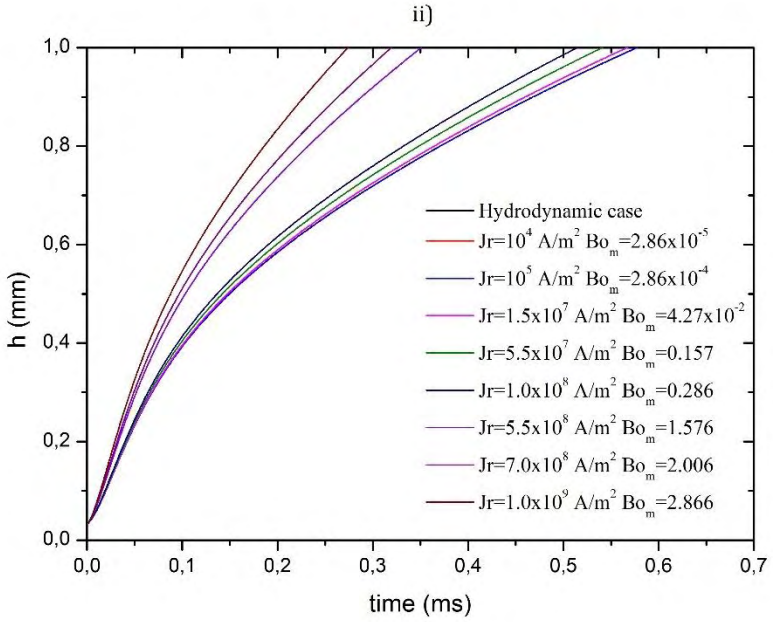

Fig 6.11 Temporal evolution of the i) rising velocity and ii) column height for B_0 = 1T.

In other words, pressure drop along the main flow direction (z direction) increases with increasing the effect of the magnetic forces, as reported in [32]. Besides, it is worth mentioning that as x approaches unity (x = 1 at the interface), an abrupt change in pressure is observed for every value of J_r. This is due to the pressure just outside the liquid, which is $p_{out} = 0$ for every simulation. Besides, the constant pressure gradient along the z direction is the reason behind the Poiseuille velocity profile observed in Subsection 6.2. This can be seen in **Fig. 6.13** which provides a sequence of velocity profiles at the pore entrance for $Bo_m \to 0$ and $Bo_m > 1$. Although the magnetic Bond number in ii) is much larger than that of i), however, the profiles corresponding to the same time instant appear to have the same shape. Only the maximum velocity, u(r=0), at each time instant varies.

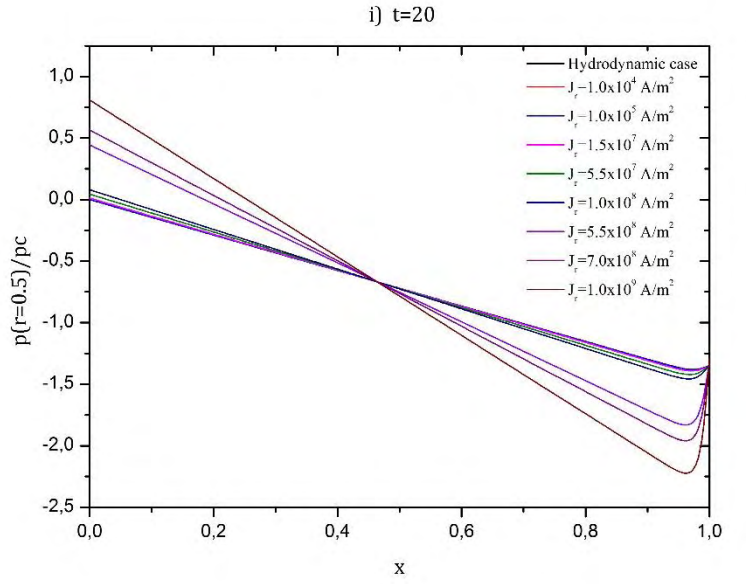

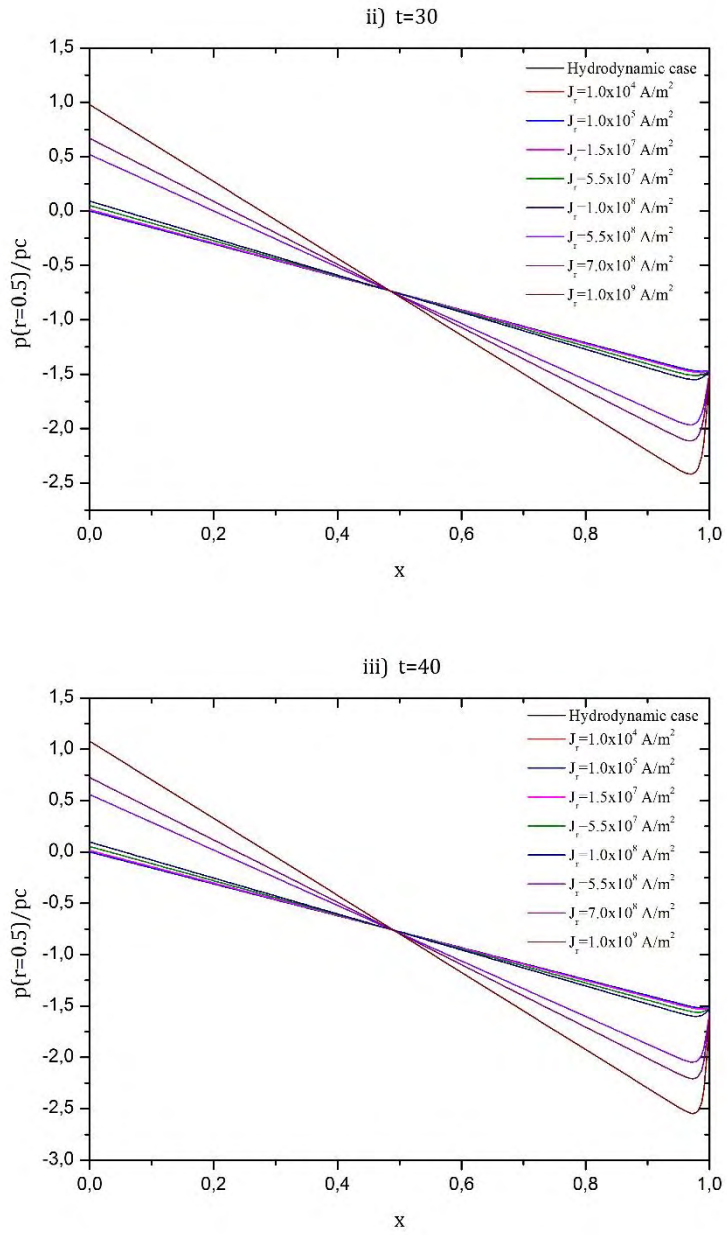

Fig. 6.12 Dimensionless pressure distribution at the center of the pore cross section, r=Rp/2 at i) t=20, ii) t=30, iii) t=40

This observation is in agreement with the result depicted in **Fig. 6.11** i). The reason behind this behaviour lies in the Ca number, which measures the importance of viscosity over surface tension. In every simulation run so far the Ca number is the same.

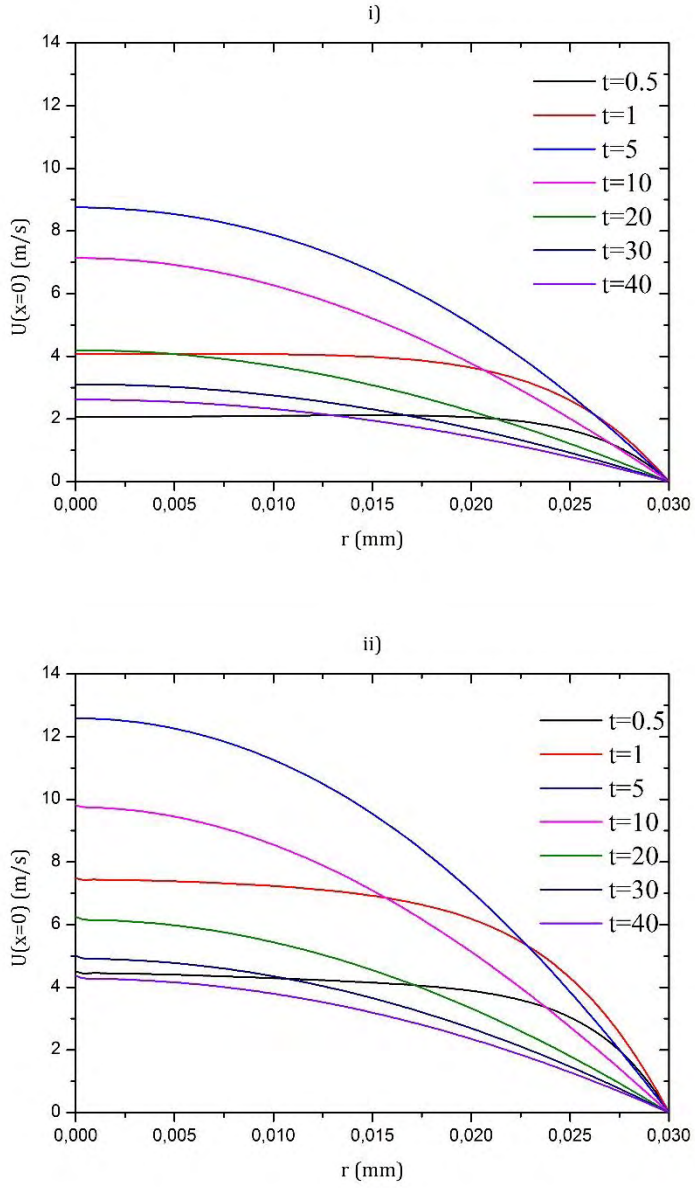

Fig. 6.13 Time evolution of the velocity profile at x = 0 for B_0 = 1T: i) Jr = 10^5 A/m^2 and ii) Jr = 10^9 A/m^2. Time instants are dimensionless.

Continuing with the case of B_0 = 1T, the shape of the interface is plotted against the radial spatial coordinate. Emphasis is being given to the cases where $Bo_m > 1$. In these cases, the occuring Lorentz forces are of greater importance than surface tension forces. The temporal evolution of the interface along with its position is seen in **Fig. 6.14**. The first four diagramms are t = 0.0197, 0.0329, 0.049 and 0.065 ms in real time, correspondingly. During the first moments of wicking (t = 3-7.5), an inter-facial distrortion is seen, resulting in a different shape than those presented in Subsection 6.2. This distortion is observed until t = 7.5 and from t = 10 and beyond, the shape seems to appear similar to those presented in Subsection 6.2, in which the curve is flat near the axis of symmetry and increases monotonically. At the pore wall, the meniscus is formed with a constant contact angle. It is of great interest to explain why this phenomenon is met only during a small time period, approximately

during the first 0.05 ms of the simulation. Thus far, the electrical current at the pore entrance has not been investigated. Interestingly, its role is nontrivial. **Fig. 6.15** shows the evolution of the aforementioned current with time. It is shown that the time period in which interfacial distortions appear coincide with the time in which the magnitude of this current reaches a minimum value and specifically at t = 0.025 ms. As time progresses beyond 0.025 ms, it increases with an increasing rate. Also, the magntitude of J increases with increasing J_r due to current conservation. Therefore, the first moments of wicking are crucial as far as stability is concerned for the case where the magnetic pressure is the dominant one.

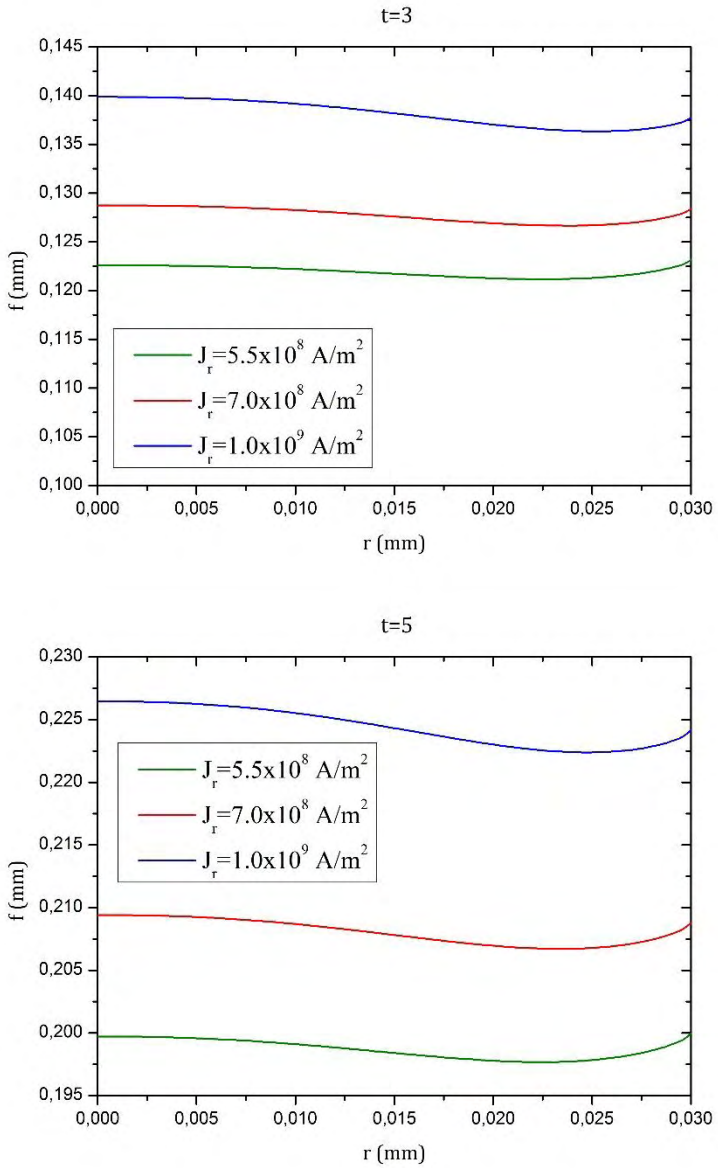

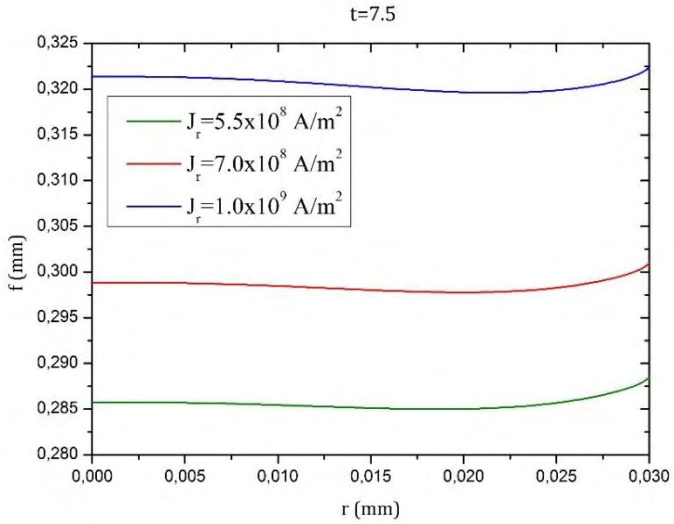
t=7.5
f (mm)
r (mm)
J_r=5.5x10^8 A/m^2
J_r=7.0x10^8 A/m^2
J_r=1.0x10^9 A/m^2
0,325
0,320
0,315
0,310
0,305
0,300
0,295
0,290
0,285
0,280
0,000
0,005
0,010
0,015
0,020
0,025
0,030

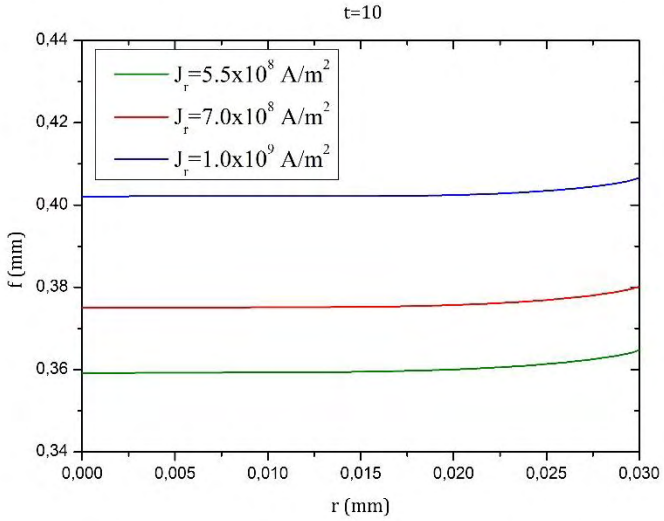
t=10
f (mm)
r (mm)
J_r=5.5x10^8 A/m^2
J_r=7.0x10^8 A/m^2
J_r=1.0x10^9 A/m^2
0,44
0,42
0,40
0,38
0,36
0,34
0,000
0,005
0,010
0,015
0,020
0,025
0,030

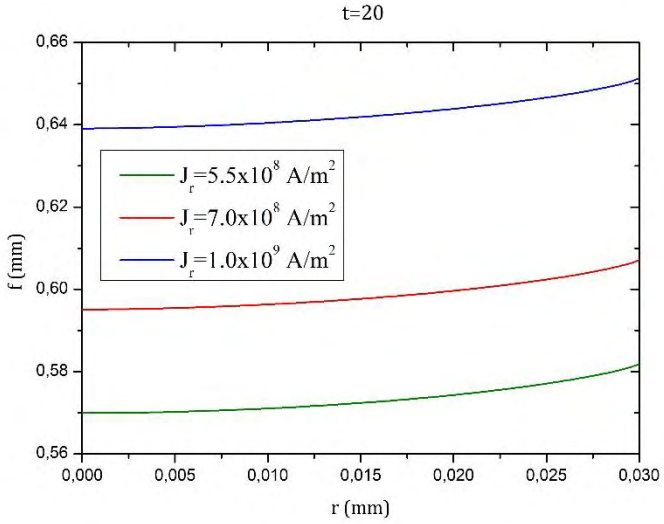
t=20
f (mm)
r (mm)
J_r=5.5x10^8 A/m^2
J_r=7.0x10^8 A/m^2
J_r=1.0x10^9 A/m^2
0,66
0,64
0,62
0,60
0,58
0,56
0,000
0,005
0,010
0,015
0,020
0,025
0,030

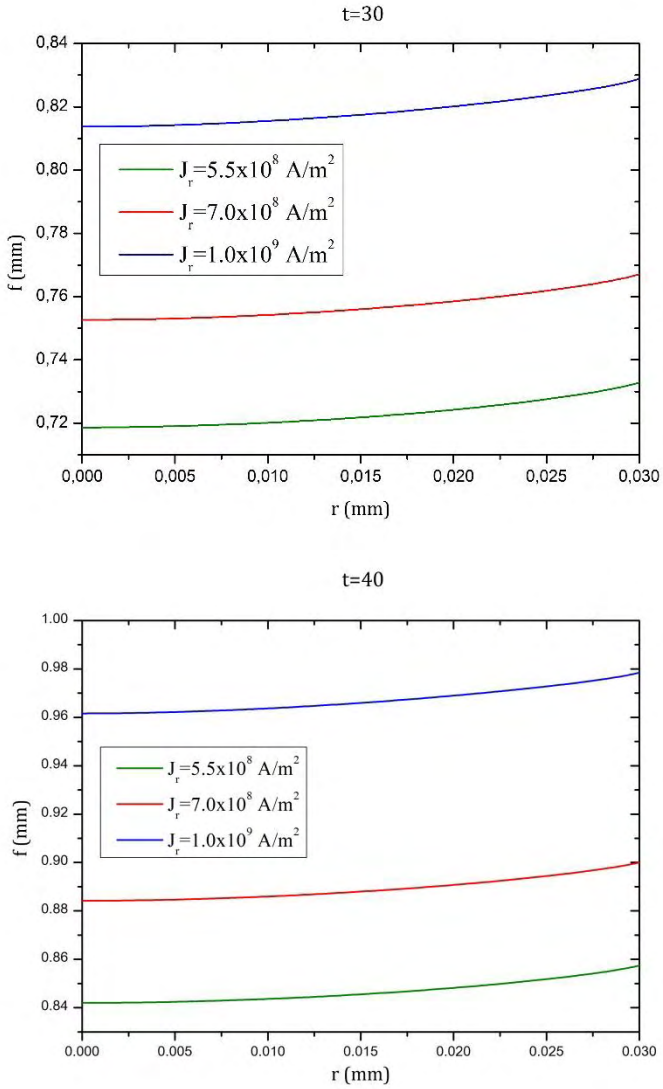

Fig. 6.14 Temporal evolution of the interface for large values of current density Jr.

Lastly, the time needed to exit the CPS pore of height h_0 and the axial velocity calculated at the meniscus tip were plotted against every value of Bo_m used so far. To be specific, the values of the magnetic Bond in Subsection 6.2.1 and 6.3 were put together in ascending order. Note that for $Bo_m \in [0.157, 1]$ the c parameter increases with Bo_m. Nonetheless, the effect of c will be negligible since Bo_m, in this interval, exceeds the critical value of 10^{-1}. Beyond this threshold, the effect of the Lorentz force on the flow is to exert a body force that points towards the pore exit. Besides, this is qualitatively assessed via the definition of the Lorentz force in vector form, where $\mathbf{J} = J_r\mathbf{e_r}$ and B_0 lies in the azimuthial direction. The characteristic time of every simulation is the same since the material and geometric parameters were fixed, thus, the characteristic time of every simulation is the same. The latter is $t_c = \frac{R_p}{\hat{u}} = \sqrt{(\rho {R_p}^3/\gamma)}$. Interestingly, the two graphs in **Fig. 6.16** indicate that the exit velocity varies linearly with Bo_m. The results corresponding to $Bo_m \leq 10^{-2}$ almost coincide with the purely hydrodynamic condition. As far as exit time is concerned, it scales like Bo_m^{-1}.

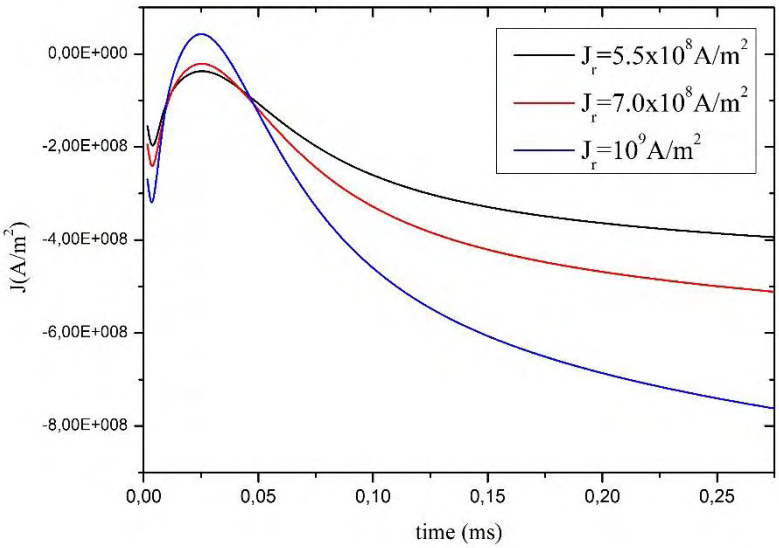

Fig. 6.15 Temporal evolution of J current for $B_0 = 1T$ and $Bo_m > 1$.

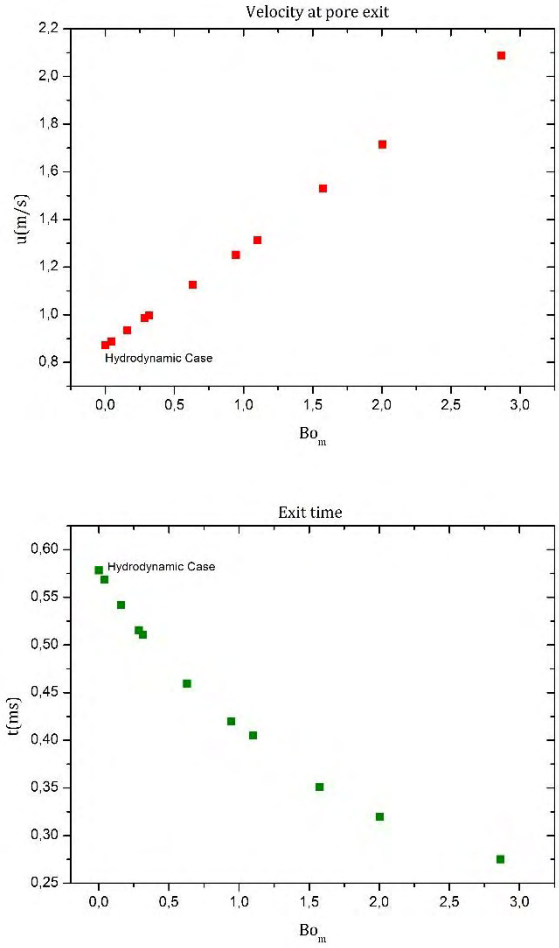

Fig. 6.16 Rising velocity and time at the exit of the pore as functions of the magnetic Bond number.

6.4 Effect of pore size

The final subsection of the Results Chapter investigates the effect of an increasing pore radius. As it has been stated in Chapter 2, the appropriate pore radius for the porous mesh of the CPS ranges between 20-100 μm. Furthermore, in [1] Benos presented a series of results for the capillary rise of Li without MHD formulation and pore radius lying in the interval mentioned above. The mathematical model he used is the same as the one used in this thesis with the only difference being the absence of the local acceleration $\partial \boldsymbol{u}/\partial t$. The Boundary Conditions were also the same, excluding those presented in Chapter 3. Based on the above, the pore radius was altered from 30-100 μm, while the MHD input variables were fixed. Specifically, B_0 was set to 1T and (J_z, J_r) to (0, 5.5x10^7 A/m^2). However, according to the definition of Bo_m, c and the characteristic velocity (Eq. 4.41), a change in R_p will change theses parameters as well. The magnetic Bond is proportional to R_p^2 while $\hat{u} \sim \sqrt{R_p}$. The c number is proportional to the characteristic velocity. Furthermore, the pore radius is included in the Ca, Bo and Re numbers as well, so, these numbers will also be different than in the cases discussed above. The table below shows the values of all the dimensionless numbers as the pore radius increases from 30 to 100 μm. The Weber number is excluded since it is always unity. Based on the data listed above, Bo_m increases from 0.157 to values exceeding unity while c decreases, always being less that unity. The Capillary number continuously decreases and the hydrodynamic Reynolds increases, implying that viscous effects become less important than surface tension and inertia. At the same time, transient effect are going to be more important due to the increasing Re. As far as gravitational Bond is concerned, it is O(10^{-5}-10^{-4}) and the effect of gravity remains negligible.

Table 2: Values of all the parameters that depend on Rp for 1T and Jr = 5.5x10^{7}A/m^2 (Rp = 30-100 μm)

R_p(μm)	30	40	50	60	70	80	90	100
Bo_m	0.157	0.280	0.438	0.630	0.858	1.121	1.418	1.751
c	0.271	0.235	0.210	0.192	0.177	0.166	0.156	0.148
Ca	0.033	0.028	0.025	0.023	0.021	0.020	0.019	0.018
Re	30.15	34.82	39	42.65	46.07	49.24	52.23	55.06
Bo	1.4x10^{-5}	2.5x10^{-5}	3.9x10^{-5}	5.6x10^{-5}	7.7x10^{-5}	10^{-4}	1.3x10^{-4}	1.5x10^{-4}

In the following figures, the axial exit velocity at the meniscus tip and the time needed to reach the pore exit is presented for every value of R_p. It is seems that as the pore radius reaches relatively large values, according to [1, 18], its effect on time and velocity at the exit of the CPS resembles the form presented by Benos in [1], although in the latter a quasi-steady pattern was assumed for the hydrodynamic momentum equations (B_0 = 0T in our problem) and transient terms were neglected. In other words, in [1] inertia terms were described by the the convective derivative $\mathbf{u}\cdot\nabla\mathbf{u}$ whereas in our

problem by the total derivative $\partial \mathbf{u}/\partial t + \mathbf{u}\cdot\nabla\mathbf{u}$. Nevertheless, the velocities presented therein are much smaller than those in **Fig. 6.17** since the results here concern a magnetohydrodynamic case. Moreover, in our problem the presense of the external magnetic field augments the fluid pressure and increases the magnitude of the body forces. The latter is attributed to the rotational term of Eq. 4.43.

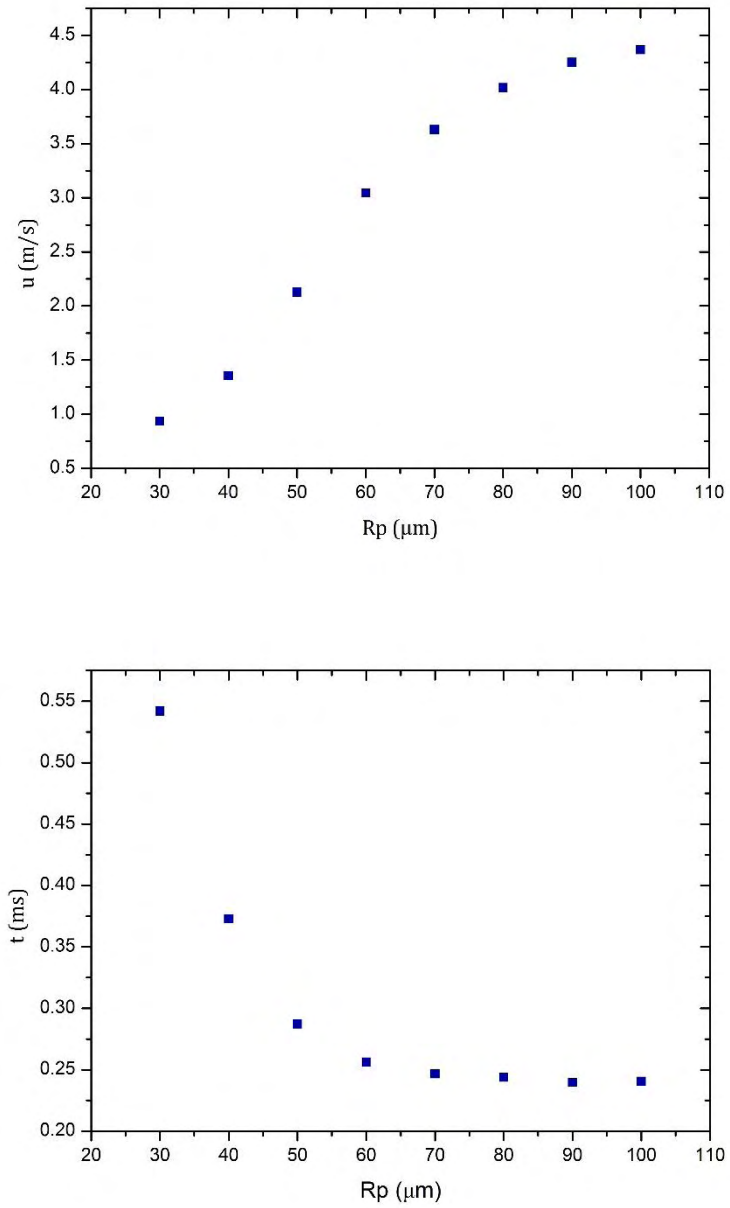

Fig. 6.17 Axial velocity (up) at the meniscus position during exit and time needed to exit the CPS pore (bottom).

Later, it was examined whether the pore radius has the same effect on the shape of the liquid metal interface, similarly to the results presented in the last part of Subsection 6.3 since for relatively large Rp the magnetic Bond exceeds unity. **Fig. 6.18** presents contour plots of the dimensionless magnetic stream function at the same dimensionless time instant t = 5. The results incicate that the form of the contour plots is similar for every case since the magnetic input variables are the same and Bo_m is al-

most O(1). The largest gradient of H is observed near the interface. The latter implies that the magnitude of the induced currents is larger in that region than in the bulk domain of the liquid column.

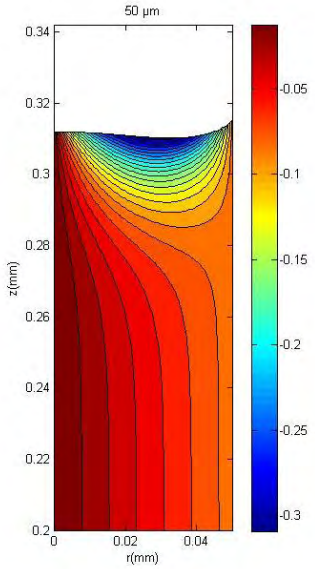

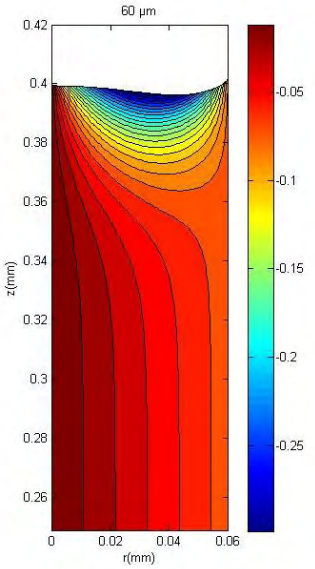

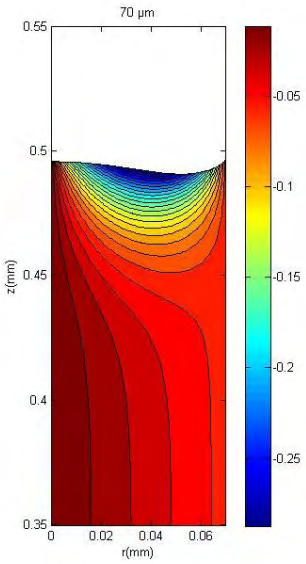

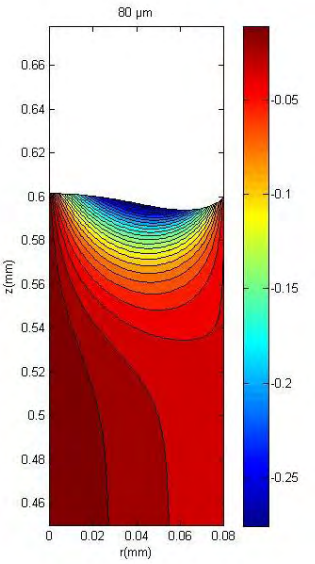

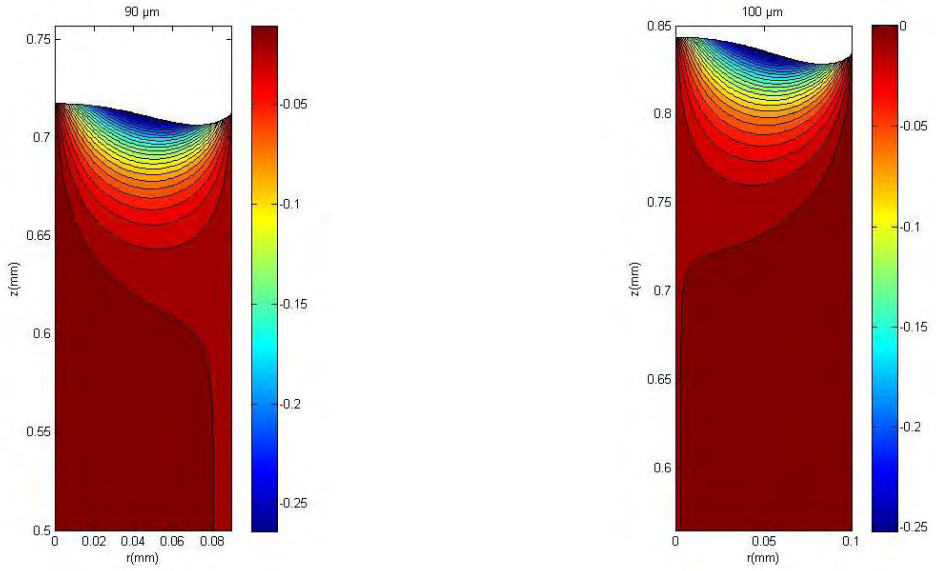

Fig. 6.18 Contour plots of H at t = 5 for R_p = 50, 60, 70, 80, 90 and 100 µm.

Recalling the Boundary Condition of Eq. 4.50, which states that $H = J/2$ at the pore wall and taking a look on the right boundary of each plot, it is deduced that the value of J decreases with Rp. These results are consistent with Eq. 3.25 which implies that if $J_z = 0$ and gradients f_r are of the same order of magnitude then the current density at the pore entrance decreases with the pore radius. Most importantly, as R_p increases, an increasing distortion is seen near the axis of symmetry similar to those in the previous Subsection. These disturbances are expected to have a duration (in physical time) which increases with the pore radius since transient effects last longer according to **Fig. 6.19**.

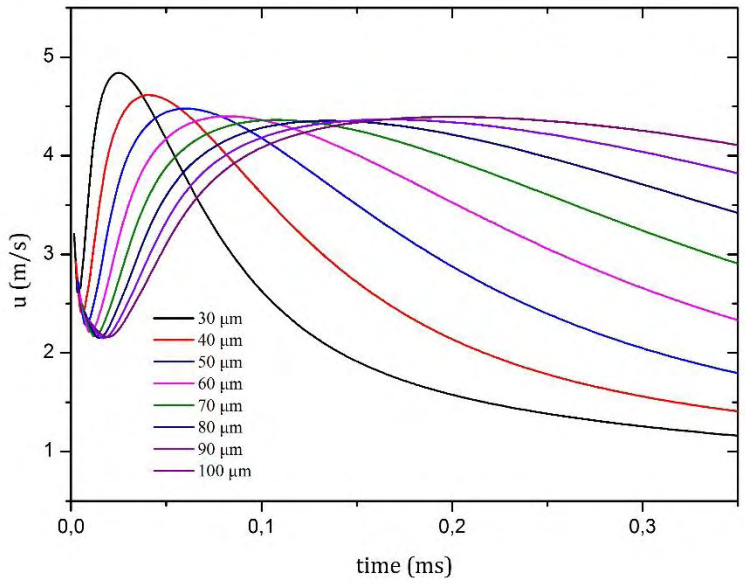

Fig. 6.19 Li rising velocities at 1T and Jr = 5.5x10^7 A/m^2, Jz = 0 for R_p = 40-100 µm.

Accordingly, for a fixed height of h_0 = 1mm and increasing pore radius, the LM exits the pore with its interface slightly being elevated near the center of the pore, implying possibility of drop ejection. A possible countermeasure against it would be a pore of greater height. This would increase the distance the LM needs to cover in order to exit the porous mesh. Then, since the time period the LM remains in the pore level is larger, viscous effects will begin to act against the LM motion as it approaches the quasi steady arrangement. In conclusion, the pore radius has a significant role on whether drop ejection appears in a real CPS of a fusion environment although it is independent of the conditions outside the CPS (e.g, Intensity of B_0 and currents hitting upon the CPS).

Chapter 7: Conclusions

In the final Chapter of this thesis, the main results of this work are summarized and directions for future work are given.

7.1 General conclusions

In the analysis conducted in this work, the finite element method was used in order to numerically solve the rise of a fusion-related liquid metal inside a capillary porous system (CPS) under the effect of a transverse magnetic field. The geometry of the problem consisted of a single vertical capillary tube of constant diameter, similar to previous studies. During the liquid's vertical motion, an electrical current enters the liquid column via the liquid gas interface, severely affecting the flow and mainly the Lorentz forces. The results obtained from an extensive series of simulations are summarized below:

- For cases in which the current density at the interface is kept fixed while the imposed field intensity is varied, two different results are obtained, depending on the magnitude of the radial current component. On the one hand, small J_r values seem to produce a negligible braking effect on the fluid velocity, but on the other hand J_r large enough to produce a magnetic Bond number of $O(10^{-1})$ increases the liquid rising velocity. Thus, the importance of MHD effects depends on the magnitude of the currents entering the liquid column.
- When the magnetic field strength is kept constant, the MHD effect is intensified as J_r increases. Also, it should be stressed that a clear departure from the hydrodynamic case is seen when $c \geq O(1)$.
- In cases in which Bo_m is greater than unity, deformations of the liquid gas interface occur for a small period of time. The aforementioned period is proven to coincide with the time interval in which transient behavior is noticed. Therefore, this work may provide a qualitative assessment on when interfacial instabilities or drop ejection may occur as far as the replenishment process is concerned.
- The time at which the liquid column reaches the CPS height is inversely proportional to the magnetic Bond number while the exit velocity of the meniscus tip varies almost linearly with the latter.These results hold for fixed pore radius.
- Pressure at the pore entrance increases with increasing the current entering the interface. Consequently, an extra pressure at the inlet of the liquid flow is observed. MHD pressure drop along the z direction, which is the main flow direction, increases with J_r for a fixed magnetic field intensity.
- As a general trend, the effect of the magnetic field is to increase the axial velocity if Bo_m exceeds a certain threshold. Based on the results of Subsection 6.3, this threshold is exceeded when $Bo_m \geq O(10^{-2})$. This is due to the dimensionless parameter dictating the effect of the emerging magnetic pressure. The latter is defined in such a way that it incorporates both the field intensity and the current at the interface.
- Inlet velocity profiles follow the Poiseuille profile. For fixed pore geometry, the MHD profiles corresponding to $Bo_m = O(10^{-1})$ increase with either B_0 for constant J_r, or with J_r for constant B_0. For the latter case and at the same time instants, a large J_r (10^9 A/m^2 for instance) produces profiles significantly larger than those of $J_r = 10^5$ A/m^2. As a result, the mean inlet

velocity increases with Bo_m and in a real CPS environment that would demand a larger volumetric flow rate of liquid Li from the reservoir. The flow rate can be calculated by the simple formula $\dot{V} = \bar{u}\pi {R_p}^2$where $\bar{u}$ is the mean inlet axial velocity. This formula applies to the geometrical configuration deployed in this study. Apparently, the volumetric flow rate will be time dependent.

- Compared to the case of $J_z = 0$, a non-zero z current component either increases or decreases the fluid velocity depending on its direction. This is observed when J_z is the same order of magnitude with J_r and $Bo_m = O(10^{-1})$. Consequently, both magnetic braking and propulsion are possible due to the presence of J_z.
- For constant operational parameters, which consist of the applied magnetic field and the current entering the CPS, larger pore radius lead to larger magnetic pressure, enhanced interfacial deformations near the z axis (pore center) which last longer due to the increased duration of transient behavior. Besides, for relatively large pore size (70-100 μm), the effect of the latter on the time for exit is seen to be the same.

7.2 Directions for future work

In the last section of this study, future perspectives conserning the mathematical model describing the flow of Li in the pore level are presented. More specifically, the proposed future work can be focused on the following directions.

- A three-dimensional MHD flow in the pore level. The applied magnetic field may have a second component at the vertical direction (**Fig. 7.1**)
- The MHD model presented in Chapter 4 can be extended by assuming non isothermal conditions. Instead, an external heat load corresponding to realistic divertor heat loads can be introduced Fig. 7.2.
- Introduction of an interaction potential in order to provide an assessment of the combined effect of intermolecular and Lorentz forces.
- Simulation of the spreading process on top of the porous substrate (**Fig. 7.1**)

The concepts presented in the first and last bullet are already in development by Dr Pelekasis and his colleagues.

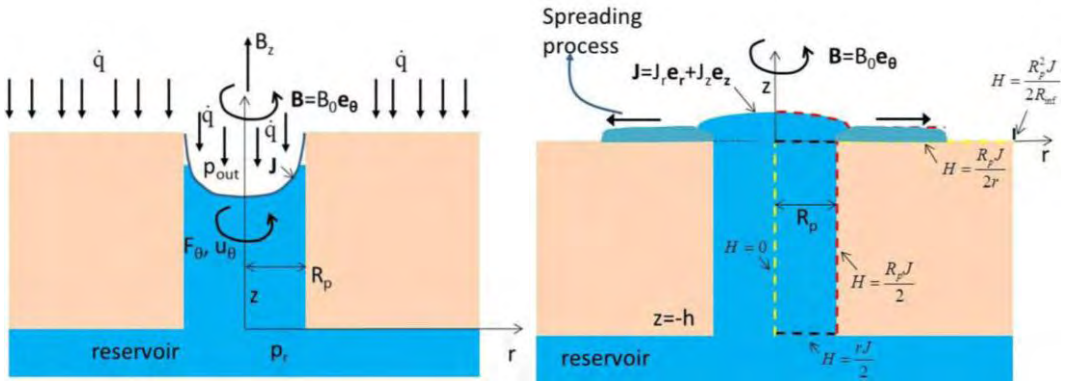

Fig. 7.1 (Left)Schematic of the flow arrangement within the pore in the presence of heat and momentum transfer and Lorentz forces. (Right) Schematic of the spreading process.

References

[1] Lefteris Th. Benos, *First Principles study of the static arrangement of a plasma facing component in the form of a capillary porous system (CPS),* (PhD Thesis) University of Thessaly, Greece, 2018.

[2] P. A. Davidson, *An Introduction to Magnetohydrodynamics, 2nd Edition*, New York, NY: Cambridge University Press (2001).

[3] N.B. Morley, S. Smolentsev and D. Gao, *Modeling infinite/axisymmetric liquid metal magnetohydrodynamic free surface flows*, Fusion Engineering and Design 6364 (2002) 343-351.

[4] S. F. Kistler and L. E. Scriven, *Coating flow theory by finite element and asymptotic analysis of the Navier-Stokes system*, International Journal for Numerical Methods in Fluids 4 (1984) 207-229.

[5] E. Widjaja, Nai-Chi Liu, M. Li, R. T. Collins, O. A. Basaran and M. T. Harris, *Dynamics of sessile droplet evaporation: A comparison of the spine and the elliptic mesh generation methods*, Computers and Chemical Engineering 31 (2007) 219 – 232.

[6] S. Smolentsev, S. Cuevas and A. Beltran, *Induced electric current-based formulation in computations of low magnetic Reynolds number magnetohydrodynamic flows*, Journal of Computational Physics 229 (2010) 1558 – 1572.

[7] S. Smolentsev, M. Abdou, *Open-surface MHD flow over a curved wall in the 3-D thin-shear-layer approximation*, Applied Mathematical Modelling 29 (2005) 215–234.

[8] G. K. Batchelor, *An Introduction to Fluid Dynamics*, Cambridge University Press (1967).

[9] G. K. Batchelor, H. K. Moffatt, M. G. Worster, *Perspectives in Fluid Dynamics*, Cambridge University Press (2000).

[10] S. Molokov, R. Moreau, H. K. Moffatt, *Magnetohydrodynamics*, Springer, 2007.

[11] C. Kawczynski, S. Smolentsev, M. Abdou, *An induction-based magnetohydrodynamic 3D code for finite magnetic Reynolds number liquid-metal flows in fusion blankets*, Fusion Engineering and Design 109-111 (2016) 422-425.

[12] I. E. Sarris, G. K. Zikos, A. P. Grecos & N. S. Vlachos, *On the Limits of Validity of the Low Magnetic Reynolds Number Approximation in MHD Natural-Convection Heat Transfer*, Numerical Heat Transfer, Part B: Fundamentals 50:2 (2006) 157-180.

[13] R. Moreau, *The fundamentals of MHD related to Crystal Growth*, Progress in Crystal Growth and Characterization of Materials (1999) 161-194.

[14] S. Khan, J. N. Davidson, *Magnetohydrodynamic Coolant Flows in Fusion Reactor Blankets*, Annals of Nuclear Energy Vol. 6 (1979) 499-509.

[15] P. X. Yu, Z. F. Tian, *Comparison of the simplified and full MHD models for laminar incompressible flow past a circular cylinder*, Applied Mathematical Modelling 41 (2017) 143–163.

[16] S. Middleman (1995), *Modeling Axisymmetric Flows: Dynamics of Films, Jets, and Drops*, San Diego, California: CRC Press.

[17] R. E. Nygren and F. L. Tabarés, *Liquid surfaces for fusion plasma facing components –A critical review. Part I: Physics and PSI*, Nuclear Materials and Energy 9 (2016) 6-21.

[18] I. Lyublinski, A. Vertkov, S. Mirnov and V. Lazarev, *Protection of tokamak plasma facing components by a capillary porous system with lithium*, Nuclear Materials 463 (2015) 1156–1159.

[19] V. A. Evtikhin et al., Plasma Physics and Controlled Fusion, 44 (2002) 955.

[20] J. H. Spurk, N. Aksel (2008), *Fluid Mechanics*, 2nd Edition, Springer.

[21] L. G. Golubchikov et al. *Development of a liquid metal fusion reactor divertor with a capillary pore system*, Journal of Nuclear Materials, 233-237 (1996) 667-672.

[22] F.L. Tabarés, *Present status of liquid metal research for a fusion reactor*, Plasma Physics and Controlled Fusion, 58 (2016).

[23] C. Pozrikidis, *Fluid Dynamics: Theory, Computation and Numerical Simulation*, Third Edition, Springer 2017.

[24] S. Kenjeres, *On modeling and eddy-resolving simulations of flow, turbulence, mixing and heat transfer of electrically conducting and magnetizing fluids: A review*, International Journal of Heat and Fluid Flow, 73 (2018) 270-297.

[25] D. Gao, N. B. Morley, V. Dhir, *Numerical study of liquid metal film flows in a varying spanwise magnetic field*, Fusion Engineering and Design 63-64 (2002) 369-374.

[26] N. B. Salah, A. Soulaimani, W. G. Habashi, *A finite element method for magnetohydrodynamics*, Computer Methods in Applied Mechanics and Engineering 190 (2001) 5867-5892.

[27] Nikos Pelekasis, Lefteris Benos, *Static arrangement of a capillary porous system (CPS): Modelling*, Fusion Engineering and Design 117 (2017) 180-187.

[28] J. N. Reddy (1993), *An Introduction to the Finite Element Method*, 2nd Edition, New York, NY: Cambridge University Press. McGraw-Hill, Inc.

[29] G. Karniadakis, A. Beskok, A. Narayan (2005), *Microflows and Nanoflows*, Springer.

[30] G. Mazzitelli, M. L. Apicella, A. Alexeyev and FTU Team**,** *Heat loads on FTU liquid lithium limiter,* Fusion Engineering and Design 86 (2011) 580-583.

[31] H. W. Kugel, J. P. Allain, M. G. Bell, R. E. Bell, A. Diallo, R. Ellis et al*., NSTX plasma operation with a Liquid Lithium Divertor*, Fusion Engineering and Design 87 (2012) 1724-1731.

[32] L. Buhler, C. Mistrangelo, T. Najuch, *Magnetohydrodynamic flows in model porous structures*, Fusion Engineering and Design, 98-99 (2015) 1239-1243.

[33] S. J. Zinkle, *Summary of Physical properties for Lithium, Pb-17Li and (LiF)nBeF2 Coolants*, Technical report (1998) APEX study meeting, Sandia National Lab.

[34] U. Shumlak, B.A. Nelson, E.L. Claveau, E.G. Forbes, R P. Golingo, M.C. Hughes et al., *Increasing plasma parameters using sheared flow stabilization of a Z-pinch*, Physics of Plasmas 24 (2017) 055702

[35] P. A. Bagryansky, A. G. Shalashov, E. D. Gospodchikov, A. A. Lizunov, V. V. Maximov, V. V. Prikhodko et al*., Threefold Increase of the Bulk Electron Temperature of Plasma Discharges in a Magnetic Mirror Device,* Physical Review Letters 114 (2015) 205001.

[36] Y. Xu, *A general comparison between tokamak and stellarator plasmas*, Matter and Radiation at Extremes, Matter and Radiation at Extremes 1 (2016) 192-200.

[37] ITER's homepage https://www.iter.org

[38] N. Pelekasis, L. Benos and R. Gomes, *Deflection of a liquid metal jet/drop in a tokamak environment*, Fusion Engineering and Design 12 (2014) 2930-2936.

[39] P. Rindt et al., *Conceptual Design of a pre-loaded liquid lithium divertor target for NSTX-U*, Fusion Engineering and Design 112 (2016) 204-212.

[40] V. A. Evtikhin et al., *Research of lithium capillary-pore system for fusion reactor plasma facing component*, Journal of Nuclear Materials 307-311 (2002) 1664-1669.

[41] G. van Eden et al., Self-Regulated plasma heat flux mitigation due to liquid Sn vapor shielding, Physical Review Letters 116 135002.

[42] Vladimir S. Ajaev, *Interfacial Fluid Mechanics, A Mathematical Modeling Approach*, Springer 2012.

[43] Michael Strange, Michael E. Dreyer and Hans J. Rath, *Capillary driven flow in circular cylindrical tubes*, Physics of Fluids Volume 15, Number 9.

[44] Abraham Marmur and Ruben D. Cohen, *Characterization of Porous Media by the Kinetics of Liquid Penetration*: The Vertical Capillaries Model, Journal of Colloid and Interface Science 189, 299-304 (1997).

[45] M. Narula, M. A. Abdou, A. Ying, N. B. Morley, M. Ni, R. Miraghaie, J. Burris, *Exploring liquid metal plasma facing component (PFC) concepts – Liquid metal film flow behavior under fusion relevant magnetic fields*, Fusion Engineering and Design 81 (2006) 1543-1548.

[46] T. W. Morgan, D. C. M. van Bekerom, G. De Temmerman, *Interaction of a tin-based capillary porous structure with ITER/DEMO relevant plasma conditions*, Journal of Nuclear Materials 463 (2015) 1256-1259.

[47] F. L. Tabarés, E. Oyarzabal, A. B. Martin-Rojo, D. Tafalla, A. de Castro and A. Soleto, *Reactor plasma facing component designs based on liquid metal concepts supported in porous systems*, Nuclear Fusion 57 (2017) 016029.

[48] You J. H. et al, *Conceptual design studies for the European DEMO divertor: rationale and first* results, Fusion Engineering and Design 109-111 (2016) 1598-1603.

[49] I. E. Lyublinski, A. V. Vertkov and V. A. Evtikhin, *Application of lithium in systems of fusion reactors. 1. Physical and chemical properties of lithium*, Plasma Devices and Operations, Vol. 17, No. 1, 2009, 42–72.

[50] V. A. Evtikhin, A. V. Vertkov, I. E. Lyublinski,B. I. Khripunov, V. B. Petrov, S. V. Mirnov, *Research of lithium capillary-pore systems for fusion reactor plasma facing components*, Journal of Nuclear Materials, 307-311 (2002) 1664-1669.

APPENDIX SECTION

Appendix A: Derivation of unit vectors and mean curvature in cylindrical coordinates

Cylindrical coordinates (r, θ, z) are related to the cartesian (x, y, z) by the following formulas:

$$x = r\cos\theta$$
$$y = r\sin\theta$$
$$z = z$$

and

$$\mathbf{e_r} = \cos\theta\mathbf{e_x} + \sin\theta\mathbf{e_y}$$
$$\mathbf{e_r} = \cos\theta\mathbf{e_x} - \sin\theta\mathbf{e_y}$$
$$\mathbf{e_z} = \mathbf{e_z}$$

Unit vectors and Mean Curvature

Let f(r), $\mathbf{n}, \mathbf{t}$ represent the two-dimensional shape of a liquid surface in contact with a gas along with its normal and tangent unit vectors, respectively. The unit vectors in cylindrical coordinates are defined by the following relations:

$$\mathbf{n} = \frac{\mathbf{e_z} - f_r\mathbf{e_r}}{\sqrt{1+f_r^{\,2}}} \qquad \text{A.1}$$

$$\mathbf{t} = \frac{\mathbf{e_z} + f_r\mathbf{e_r}}{\sqrt{1+f_r^{\,2}}} \qquad \text{A.2}$$

Here $\mathbf{e_r}$, $\mathbf{e_z}$ are the unit vectors and the mean curvature of the surface, H_c, is related to the unit vectors through the following relation :

$$2H_c\mathbf{n} = \frac{\partial\mathbf{t}}{\partial s} - \frac{\mathbf{n}}{R_2} = \left(\frac{1}{R_1} + \frac{1}{R_2}\right)\mathbf{n} = \left(\nabla_s \cdot \mathbf{n}\right)\mathbf{n} \qquad \text{A.3}$$

In the above relation, R_1, R_2 are the radii of curvature and are taken as positive when the respective centres of curvature are on the gas side of the interface [8]. They are calculated using the following expressions:

$$\frac{1}{R_1} = \frac{f_{rr}}{\left(1+f_r^{\,2}\right)^{3/2}}, \qquad \frac{1}{R_2} = \frac{-f_r}{r\left(1+f_r^{\,2}\right)^{1/2}} \qquad \text{A.4}$$

Appendix B: Analytical expressions of $\underline{\underline{\tau_v}} : \nabla(B_i \mathbf{e_k})$, $\nabla(B_i \mathbf{e_k})$

In this appendix the derivation of the components of the tensors, $\underline{\underline{\tau_v}}, \nabla(B_i \mathbf{e_k})$ is carried out under the assumption of axisymmetry, pertaining to geometric configuration of the problem studied, for a two-dimensional velocity field $\mathbf{u} = u(r,z)\mathbf{e_z} + v(r,z)\mathbf{e_r}$ in cylindrical coordinates.

B.1 Derivation of $\nabla(B_i \mathbf{e}_z)$

$$\nabla(B_i \mathbf{e}_z) = \mathbf{e_r}\mathbf{e_z}\frac{\partial B_i}{\partial r} + \mathbf{e_r}\overset{0}{\frac{\partial \mathbf{e_z}}{\partial r}}B_i + \frac{\mathbf{e_\theta}}{r}\overset{0}{\frac{\partial B_i}{\partial \theta}}\mathbf{e_z} + \frac{\mathbf{e_\theta}}{r}\overset{0}{\frac{\partial \mathbf{e_z}}{\partial \theta}}B_i + \mathbf{e_z}\mathbf{e_z}\frac{\partial B_i}{\partial z} + \mathbf{e_z}\overset{0}{\frac{\partial \mathbf{e_z}}{\partial z}}B_i = \begin{bmatrix} 0 & 0 & \frac{\partial B_i}{\partial r} \\ 0 & 0 & 0 \\ 0 & 0 & \frac{\partial B_i}{\partial z} \end{bmatrix} \qquad \text{B.1}$$

B.2 Derivation of $\nabla(B_i \mathbf{e_r})$

$$\nabla(B_i \mathbf{e}_r) = \mathbf{e_r}\frac{\partial B_i}{\partial r}\mathbf{e_r} + \mathbf{e_r}\overset{0}{\frac{\partial \mathbf{e_r}}{\partial r}}B_i + \frac{\mathbf{e_\theta}}{r}\overset{0}{\frac{\partial B_i}{\partial \theta}}\mathbf{e_r} + \frac{\mathbf{e_\theta}}{r}\overset{=\mathbf{e_\theta}}{\frac{\partial \mathbf{e_r}}{\partial \theta}}B_i + \mathbf{e_z}\overset{0}{\frac{\partial \mathbf{e_r}}{\partial z}}B_i + \mathbf{e_z}\mathbf{e_r}\frac{\partial B_i}{\partial z} = \begin{bmatrix} 0 & \frac{\partial B_i}{\partial r} & 0 \\ 0 & \frac{B_i}{r} & 0 \\ \frac{\partial B_i}{\partial z} & 0 & 0 \end{bmatrix} \qquad \text{B.2}$$

B.3 Derivation of $\underline{\underline{\tau_v}} : \nabla(B_i \mathbf{e_k})$

z component:

$$\underline{\underline{\tau_v}} : \nabla(B_i \mathbf{e}_z) = \begin{bmatrix} 2\frac{\partial v}{\partial r} & 0 & \frac{\partial u}{\partial r} + \frac{\partial v}{\partial z} \\ 0 & 2\frac{v}{r} & 0 \\ \frac{\partial u}{\partial r} + \frac{\partial v}{\partial z} & 0 & 2\frac{\partial u}{\partial z} \end{bmatrix} : \begin{bmatrix} 0 & 0 & \frac{\partial B_i}{\partial r} \\ 0 & 0 & 0 \\ 0 & 0 & \frac{\partial B_i}{\partial z} \end{bmatrix} = \frac{\partial B_i}{\partial r}\left(\frac{\partial u}{\partial r} + \frac{\partial v}{\partial z}\right) + 2\frac{\partial u}{\partial z}\frac{\partial B_i}{\partial z} \qquad \text{B.3}$$

r component:

$$\underline{\underline{\tau}}_v : \nabla(B_i \mathbf{e}_r) = \begin{bmatrix} 2\frac{\partial v}{\partial r} & 0 & \frac{\partial u}{\partial r}+\frac{\partial v}{\partial z} \\ 0 & 2\frac{v}{r} & 0 \\ \frac{\partial u}{\partial r}+\frac{\partial v}{\partial z} & 0 & 2\frac{\partial u}{\partial z} \end{bmatrix} : \begin{bmatrix} \frac{\partial B_i}{\partial r} & 0 & 0 \\ 0 & \frac{B_i}{r} & 0 \\ \frac{\partial B_i}{\partial z} & 0 & 0 \end{bmatrix} = 2\frac{\partial v}{\partial r}\frac{\partial B_i}{\partial r} + \frac{\partial B_i}{\partial z}\left(\frac{\partial u}{\partial r}+\frac{\partial v}{\partial z}\right) + 2\frac{vB_i}{r^2} \qquad \text{B.4}$$

where $\underline{\underline{\tau}}_v$ is the dimensionless form of the viscous stress tensor of a Newtonian fluid and reads:

$$\underline{\underline{\tau}}_v = \nabla\mathbf{u} + (\nabla\mathbf{u})^{\mathrm{T}} = \begin{bmatrix} 2\frac{\partial v}{\partial r} & 0 & \frac{\partial u}{\partial r}+\frac{\partial v}{\partial z} \\ 0 & 2\frac{v}{r} & 0 \\ \frac{\partial u}{\partial r}+\frac{\partial v}{\partial z} & 0 & 2\frac{\partial u}{\partial z} \end{bmatrix} \qquad \text{B.5}$$